UNIVERSITÉ PARIS XI
École Doctorale
Rayonnements & Environnement

N° SUDOC : 2009PA112253

Atomic Beam Merging and Suppression of Alkali Contaminants in Multi Body High Power Targets: Design and Test of Target and Ion Source Prototypes at ISOLDE

Thèse
présentée pour l'obtention du grade de
Docteur en Sciences de l'Université Paris XI Orsay
par

Elian J. A. BOUQUEREL

Soutenue le 10 Décembre 2009

Membres du Jury

Bernard BERTHIER - *Directeur de thèse*
Pierre BRICAULT - *Rapporteur*
Pierre DESESQUELLES - *Président de Jury*
Jacques LETTRY - *Superviseur*
Marc LOISELET - *Rapporteur*
Thierry STORA - *Superviseur*

Atomic Beam Merging and Suppression of Alkali Contaminants in Multi Body High Power Targets: Design and Test of Target and Ion Source Prototypes at ISOLDE

Author:	Elian J. A. BOUQUEREL - CERN Marie Curie Fellow (FP6) /PhD Student, Ecole Doctorale Rayonnements et Environnement, Paris-Sud XI.
Thesis Director:	Bernard BERTHIER, Research Director, IPN-Orsay, Paris-Sud XI.
Rapporteur:	Pierre BRICAULT - TRIUMF, Vancouver, Canada.
President of Jury:	Pierre DESESQUELLES - IPN-Orsay, Paris
Supervisor:	Jacques LETTRY - CERN, EN Department, Geneva, Switzerland.
Rapporteur:	Marc LOISELET - Centre de Recherches du Cyclotron, Louvain-la-Neuve, Belgium.
Supervisor:	Thierry STORA - CERN, ISOLDE, Geneva, Switzerland.

N° SUDOC: 2009PA112253 December 2009

Abstract

The next generation of high power ISOL-facilities will deliver intense and pure radioactive ion beams. Two key issues of developments mandatory for the forthcoming generation of ISOL target-ion source units are assessed and demonstrated in this thesis. The design and production of target and ion-source prototypes is described and dedicated measurements at ISOLDE-CERN of their radioisotope yields are analyzed.

The purity of short lived or rare radioisotopes suffer from isobaric contaminants, notably alkalis which are highly volatile and easily ionized elements. Therefore, relying on their chemical nature, temperature controlled transfer lines were equipped with a tube of quartz that aimed at trapping these unwanted elements before they reached the ion source. The successful application yields high alkali-suppression factors for several elements (ie: $^{80,\ 82m}$Rb, $^{126,\ 142}$Cs, ^{8}Li, ^{46}K, ^{25}Na, ^{114}In, ^{77}Ga, $^{95,\ 96}$Sr) for quartz temperatures between *300ºC* and *1100ºC*. The enthalpies of adsorption on quartz were measured for Rubidium and Caesium. The enthalpies ΔH_{ad} (Rb) = *-242 ± 20* kJ/mol and ΔH_{ad} (Cs) = *-145 ± 20* kJ/mol are in good agreement with those obtained by isothermal chromatography.

For proton beam power of the order of *100 kW* such as foreseen in the EURISOL-DS project for direct ISOL targets, multi-body target units connected to a single ion-source are proposed. The so-called “Bi-Valve” target prototype aims to benchmark the engineering tools required to simulate effusion related decay losses and to validate the multi body target concept. Four isotopes were investigated online: ^{34,35}Ar and ^{18,19}Ne. The efficiency of the double line merging was found to be in the range of *75* to *95%*. The diffusion (analytical) and effusion (Monte Carlo) code RIBO provided the profile of the effusion distribution of the isotopes within the Bi-Valve unit for the different operation modes. A mathematical expression for the probability, *p(t)* that an isotope diffuses and effuses through the system is proposed. The simulated release efficiencies were in agreement with the experimental ones for $^{34,\ 35}$Ar at *95%* thus opening the way to the engineering of multi body target units for future facilities.

Résumé

La prochaine génération d'installation ISOL 'haute puissance' délivrera des faisceaux d'ions radioactifs intenses et purs. Deux points clés de développements nécessaires pour la prochaine génération d'unités de cibles et sources d'ions ISOL sont testés et démontrés dans cette thèse. La conception et la production de prototypes sont décrites et les mesures de leurs radioisotopes effectuées à ISOLDE-CERN sont analysées.

La pureté des radioisotopes rares ou ayant une courte durée de vie souffre de contaminations isobariques, parmi lesquelles, les alcalins qui appartiennent aux éléments hautement volatiles et facilement ionisables. En tenant compte de leur nature chimique, des lignes de transferts ont été équipées avec un tube de quartz pour retenir ces éléments avant que ceux-ci n'atteignent la source d'ions. L'application a montré avec succès la suppression des alcalins avec un facteur important pour différents éléments (ex: $^{80,\ 82m}$Rb, $^{126,\ 142}$Cs, ^{8}Li, ^{46}K, ^{25}Na, ^{114}In, ^{77}Ga, $^{95,\ 96}$Sr) à des températures de quartz allant de *300ºC* à *1100ºC*. Les enthalpies d'adsorption du quartz ont été mesurées pour le Rubidium et le Césium. Les enthalpies ΔH_{ad} (Rb) = *-242 ± 20* kJ/mol et ΔH_{ad} (Cs) = *-145 ± 20* kJ/mol sont en accords avec celles obtenues par chromatographie isotherme.

Pour un faisceau de protons avec une puissance de 100 kW, comme celui envisagé dans le projet EURISOL-DS, des unités de cibles constituées de plusieurs parties connectées à une seule source d'ions sont proposées. Le prototype de cible appelé Bi-Valve a pour objectif de valider les outils d'ingénierie requis pour simuler l'effusion des pertes par désintégrations et le concept d'une cible à plusieurs compartiments. Le Bi-Valve est une double cible et ligne de transfert se jetant dans une seule source d'ions FEBIAD. Quatre isotopes ont été étudiés en ligne : ^{34,35}Ar et ^{18,19}Ne. L'efficacité de la double ligne a été mesurée allant de *75* à *95%*. La diffusion (analytique) et l'effusion (Monte Carlo) étudiées avec le Code RIBO a permis l'élaboration du profil de la distribution de l'effusion des isotopes à travers le Bi-Valve pour différents modes opératoires. Une expression mathématique de la probabilité, *p(t)*, qu'un isotope diffuse et effuse à travers le système est proposée. Les efficacités de relâchement simulées ont été en accord avec l'expérience pour le $^{34,\ 35}$Ar à *95%* et ouvre donc le chemin à l'élaboration d'unités à cibles multiples pour de futures installations.

Contents

Remerciements

Cette thèse marque l'aboutissement d'un intéressant et long parcours universitaire qui m'a donné la chance de découvrir et de côtoyer des personnes de différents horizons: Montpellier, Glasgow, Belfast, Genève...

Je tiens tout d'abord à remercier mon superviseur, Jacques Lettry (CERN) pour m'avoir accueilli au sein de l'équipe ISOLDE et donné l'opportunité de travailler à l'élaboration de ces prototypes dans le cadre du programme de Bourse Européenne, Marie Curie (projet HIGHINT). Je remercie Thierry Stora pour m'avoir guidé et conseillé tout au long de ces recherches et Richard Catherall, chef de Section RBS.

Merci à Bernard Berthier, Directeur de Recherche à l'IPN d'Orsay, pour avoir accepté d'être mon directeur de thèse ; merci pour ses conseils, sa patience et sa disponibilité. Mes remerciements vont aussi aux membres du Jury, plus particulièrement aux rapporteurs Pierre Bricault et Marc Loiselet pour avoir accepté cette mission qui nécessite beaucoup de temps. Merci à Pierre Desesquelles pour être le Président du jury et à Michel Davier, conseiller aux thèses à l'Université Paris XI, pour ses conseils.

Merci à mon collègue de bureau, Etam Noah pour son amitié, son aide, sa patience et pour avoir supporté mes 'excès de folie' et mes plantes pendant toutes ces années.

Je remercie l'équipe de développement de cibles/sources RBS-ISOLDE pour sa formidable atmosphère, son accueil et sa compétence ; merci notamment à Daniel Carminati, Bernard Crépieux, Ermano Barbero, Liviu Penescu, Stefano Marzari, Herta Richter, Luca Bruno, Mats Lindroos, Mike Owen, Sandrina Fernandes, Tim Giles, Martin Eller...Merci à l'équipe PH-ISOLDE dont Alex Helert, Manuela Turrions Nieves & Luis Fraile, Karl Johnston (et Anne-Gaelle), Ulli Koester, Mélanie Marie-Jeanne, Dina Lopes, Gry Tveten, Frederic Wenander, Guilherme Correia, Ligia Amorim, Ana Marques, Sarah Naimi, Martin Breteinfeld & Tania Mendonça. Merci aux ingénieurs en charge d'ISOLDE: Erwin Siesling, Magnus Eriksson, Pascal Fournier, Emiliano Piselli...Je remercie l'équipe CERN-FLUKA pour m'avoir gentiment aidé dans l'apprentissage du code : Vasilis Vlachoudis, Adonai Herrera, Mario Santana Leitner, Sylvestre Catin et Anna Mackney. Merci à Luisella, Alessio, Ketil, Elias, Roberto, Markus, Francesco, Daniel...et ainsi qu'à Virginie pour les pauses-café agréables.

Je remercie Marie Sklodowska Curie (1867-1934) sans qui cette bourse et ce programme n'aurait jamais existé.

Merci à mes amis pour leur présence, leur support et leur compréhension : Larissa, Marina, Marc, Erika, Candys, William, Kerri-Ann, João, Diana, Agathe, Alex, Marie. Merci à eux, et pardon à ceux que j'ai pu malencontreusement oublier...

Je remercie mes parents pour leurs encouragements et leur soutien sans faille aucune dans tout ce que j'entreprends depuis mon premier cri.

Je remercie cette inépuisable et formidable source artistique qu'est la musique et les nombreux groupes qui m'ont été un apport non négligeable en énergie et en créativité tout au long de ces travaux. Je remercie entre autres Amorphis, Indochine, Dark Tranquillity, Therion, Muse et Radiohead d'exister.
''La musique donne une âme à nos cœurs et des ailes à la pensée'' (Platon).

Je dédie enfin cette thèse à ma tante, Yolande Bourrel; je suis sûr que ce manuscrit va lui donner une occasion de parler de moi là où elle se trouve.

Introduction

The scientific community has a growing interest in the study of radioactive nuclei far from the stability region. Nuclei far from stability play decisive roles in astrophysical nucleosynthesis that build up heavier elements than Lithium (stars and supernovae). The study of exotic nuclei contributes to the understanding of the isotopes present on Earth. Radioactive Ion Beams (RIBs) concern numerous domains such as nuclear physics, nuclear astrophysics, weak interaction physics, solid state physics and life sciences. After being produced, the nuclides of interest are electromagnetically mass-separated from the other reaction products and distributed to the experimental physics community and/or post-accelerated.
The physics of radioisotopes is the natural continuity of the studies started by Henri Becquerel, when observing the radioactivity of Uranium in 1896 [Bec-96] and afterwards by Pierre and Marie Curie when isolating Polonium and Radium in 1898 [Cur-98]. In 1934, Irene Curie and Frederic Joliot were the first physicists to create unstable nuclei in their laboratory [Jol-34]. The idea of coupling a target to an ion source from an electromagnetic mass separator was first developed in the Niels Bohr institute in 1951 [Kof-51]. In the late 60's, Isotope Separators On Line facilities were built and linked to accelerators mainly in Europe. At ISOLDE-CERN (Geneva) this concept was demonstrated to be working efficiently [Rav-75] leading to controlled, high intensity beams of RIBs available to scientists for precision measurements.

RIBs can be produced with a wide variety of techniques. Typically the isotopes of interest are produced in a nuclear reaction (between an accelerated primary projectile beam and a stationary target). The two main production mechanisms are the Isotope Separation On Line (ISOL) method and the In Flight method. In the ISOL method, radioactive ions are produced essentially at rest in a thick target which is bombarded with energetic primary particles from an accelerator. After diffusing out of the target, effusing through the transfer line and being ionised, the radioactive ions are accelerated in a post-accelerator.
For the In-Flight method an energetic heavy-ion beam is fragmented while passing through a thin target. After mass, charge and momentum selection in a fragment separator the selected ions are analysed.

Radioactive Ion Beams are present and developed all around the world.

Low energy RIB facilities:

IGISOL (Ion Guide Isotope Separator On-Line) at JYFL (University of Jyväskylä) [Moo-05] is a facility that delivers RIBs of short-lived exotic nuclei, in particular the neutron-rich isotopes from the fission reaction. The beam is cooled, bunched and isobarically purified. The isobaric purification is achieved in by a Penning trap placed after the RF-cooler element.

SLOWRI (Slow RI-beam facility) is being built at the RIKEN RI-Beam Factory (RIBF). It will provide slow, high-purity and small emittance ion beams of all elements [Rik-00]

IRIS (Investigation of Radioactive Isotopes at Synchrocyclotron) on-line isotope separator facility at the PNPI (Petersburg Nuclear Physics Institute)-Gatchina produces nuclei far from stability by interaction of 1 GeV protons with uranium targets with a typical proton current of 100 μA [Pan-02].

Facilities with post-accelerated RIBs:

SPIRAL (Système de Production d'Ions Radioactifs Accélérés en Ligne) at GANIL (Grand Accélérateur National d'Ions Lourds) is an ISOL and post-accelerator facility. It combines a target-ion source assembly and a particle accelerator, CIME (Cyclotron pour Ions de Moyenne Energie). The facility delivers radioactive beams with energies in the range between 1.7 and 25 A MeV [Vil-01].

ISOLDE facility at CERN uses proton beams up to 4 μA from the PS Booster [Iso-00]. The RIBs are produced from 25 available target materials and 4 types of ion sources (See Chapter 1), and are distributed to the experimental physics area or/and post accelerated by a linear accelerator, REX-ISOLDE, up to 3.1 MeV/u [Rex-00].

ISAC at TRIUMF (Canada's National Laboratory for Particle and Nuclear Physics) [Sch-1996] uses ISOL and post-acceleration schemes. It produces short-lived exotic nuclei through a reaction between the primary proton beam and a thick target. Additional experiments measure precise lifetimes of exotic nuclei. The first beam was achieved in 1997 with 0.5 μA of proton current on the production target, nowadays the current on target reaches up to 100 μA [Sho-02].

The cyclotron facility at Louvain-la-Neuve [Loi-96] was based on a cyclotron accelerating 30 MeV protons to produce the desired exotic element in suitable targets with an intensity up to 300 μA and a post-accelerator. The activities in this facility ended in 2009.

HRIBF (Holifield Radioactive Ion Beam Facility) at ORNL (Oak Ridge National Laboratory) [Car-08] produces neutron-rich radioactive nuclei via proton-induced fission of uranium in a low-density matrix of UC. Recently developed RIBs include ^{25}Al from a silicon carbide target and isobarically pure beams of neutron-rich Ge, Sn, Br and I isotopes from a uranium carbide target. Post-acceleration is made by 26 MeV tandem.

These facilities produce hundreds RIBs, and almost all the stable elements of the periodical table have been studied. Since then, experimental nuclear physics has developed from the technological progress of the accelerators of light particles and nuclei of heavy ions.
Other new facilities are planned worldwide. They will be designed to handle higher activities for the radioactive nuclei produced in the primary target than is available at the actual, so called first-generation, facilities [Nup-00]. In Europe this is structured by the Nuclear Physics European Collaboration Committee (NuPECC) and in the United States by the Department of Energy. Both have independently recommended the construction of a 'second-generation' facility, the EURISOL Design Study is based on the ISOL principle. It is a collaboration of 21 institutes and laboratories within Europe (full participants), with additional 21 institutions either in Europe, North America and Asia (as contributors) [Eur-01]. The aim of such a study is to increase the intensity with respect to existing facilities (from 100 μA to few mA of 1 GeV primary proton beam) [Gue-02]. A CW Linac up to 150 A MeV is planed to perform post-acceleration process. The Rare-Isotope Accelerator (RIA) study is proposed in the USA

to produce intense RIBs accelerating beams of protons to 900 MeV to bombard thick targets. (post-acceleration by a Linac up to 8-15 A MeV) [Nol-02].

Ongoing projects are:

SPIRAL2 which will accelerate 5 mA deuterons up to 40 MeV and 1 mA heavy ions up to 14.5 MeV/u. Thick and thin targets will produce RIB (neutron induced fission of UC, direct interaction of deuterons in a UC target and interaction of heavy ion beam with a target) [Lec-08].

The FRIB (Facility for Rare Isotope Beams) at MSU (Michigan State University) will use 400 kW of incoming power beam [Yor-09].

ISAC2 at TRIUMF will be an extension of the existing ISAC facility and will accelerate RIBs up to 6.5 MeV/u for masses up to 150 [Lax-03].

HIE ISOLDE is an upgrade of the current ISOLDE facility at CERN; incoming beam power will reach 10 kW (from Linac 4) to 40 kW (from LP-SPL) and post-acceleration up to 10 MeV/u for the 850 different available isotopes [Hie-00].

FAIR (Facility for Antiproton and Ion Research) at GSI will use existing SIS ring as the injector to 2 further rings. RIB production will be achieved using the in-flight technique. Uranium ions will be accelerated to 2 GeV/u for $^{238}U^{28+}$ and 34 GeV/u for $^{238}U^{92+}$ [Fai-00].

SPES (Selective Production of Exotic Species) at LNL (Legnaro National Laboratories) is a project planning to accelerate proton beams to 40 MeV towards the ISOL target. RIBs will be post-accelerated to 15 MeV/u in the linac ALPI [Spe-00].

The experiments described in this thesis were performed at the ISOLDE facility, where more than 800 isotopes (73 elements) are produced making the facility one of the world leaders in the low-energy radioactive ion beam research. It hosts a programme that ranges from basic nuclear structure to weak interaction studies [Iso-00].

The target station is the heart of ISOLDE in which a *1* or *1.4 GeV* proton beam from CERN's PS booster accelerator strikes a target to produce a range of isotopes. The radioactive isotopes produced by nuclear reactions in the stationary target diffuse out of it due to thermal energy. Once on the surface of the target material, the isotopes effuse out of the target volume through the transfer line and reach the ion source. Typically, targets are heated up to very high temperatures (*<2300ºC*) to enhance the diffusion-effusion process. Atoms of interest are then extracted, ionised and separated before they are steered to experiments. ISOLDE produces radioactive beams of a variety of species by combining a range of target materials with efficient and selective ion sources such as RILIS [Fed-06] to obtain the best possible purity. However in certain cases, isobaric impurities prevent a proper utilisation for physics. Thus new techniques of purification are mandatory.

The production of radioactive beams is a specialised field. It is important to design targets which can withstand the high primary beam power and produce the desired ion species by suitable material selection. Ion-extraction is particularly difficult if the ions have a short lifetime. With the aim of producing good RIBs, the quest for ion sources with high chemical selectivity, efficiency and long lifetime with emphasis on the beam optical properties are the highest priorities. The beam intensity of short-lived isotopes is strongly affected by decay losses due to time delay between in-target production and ion beam extraction. The development of models for calculating the release efficiencies expressing the decay losses due to diffusion from the target and effusion to the ion source is of key importance for the design and performance prediction of future targets. The demand from physics for higher particle or isotope production is driving facilities to higher accelerator powers and more intense primary beams on targets. Indeed, the future generation of targets will need to handle an incoming proton beam having a higher power than what is operated in the current facilities. This will imply important changes in the development and design of the target-ion sources used to deliver such ion beams.

This thesis deals with two target-ion source units which have been developed with the aim of anticipating and investigating RIB production at the future generations of ISOL facilities in the framework of The European Marie Curie Program, HIGHINT (High Intensity) project. **Chapter 1** discusses the principles of the ISOL technique and the nuclear reactions involved when sending a proton beam onto target materials. The facility of ISOLDE-CERN and its physics are highlighted. **Chapter 2** presents the fundamental processes which affect the purity and the release properties of a RIB. The two main parameters, diffusion and effusion, are presented as being the dominating phenomena influencing RIB quality. EURISOL will operate at high power (*100 kW* on direct targets and *4 MW* on converter). The direct targets will be used to produce primarily the proton-rich radioactive ion beams. Delivering purer RIBs is therefore mandatory. To achieve this purification task a target-transfer line unit having a quartz insert to trap alkali contamination has been built and tested at ISOLDE, **Chapter 3** presents the development and results of this experiment. Hundreds of kW of incoming power will imply the use of multiple containers merging in a single ion source to dissipate the heat generated by the impact of the proton beam. It is then mandatory to know how the effusion process and the isotope decay losses are affected by such a design. **Chapter 4** presents a dual target-transfer line prototype which was developed and tested at CERN-ISOLDE as a precursor of this concept.

Chapter 1

ISOL Method and Radioactive Ion Beam (RIB) Production at ISOLDE-CERN

1.1 The PS Booster

At the ISOLDE-CERN facility (www.cern.ch/ISOLDE) protons impinging on targets come from the Proton Synchrotron Booster (PSB) as shown in figure 1.1-1**.** It consists of a stack of four synchrotrons and receives protons (or heavier particles) injected from a LINAC (LINear particle ACcelerator) which accelerates to *1 or 1.4 GeV*. The PSB delivers short high intensity pulses at low repetition rate. Each pulse is *1.25 μs* long and consists of a microstructure of 4 bunches of *230 ns* spaced by *110 ns* (figure 1.1-2). About six pulses in a typical PS supercycle of *14.4 s* are available for isotope production at ISOLDE [All-90]. This is equivalent to a dc proton current of about *2.1 μA*.

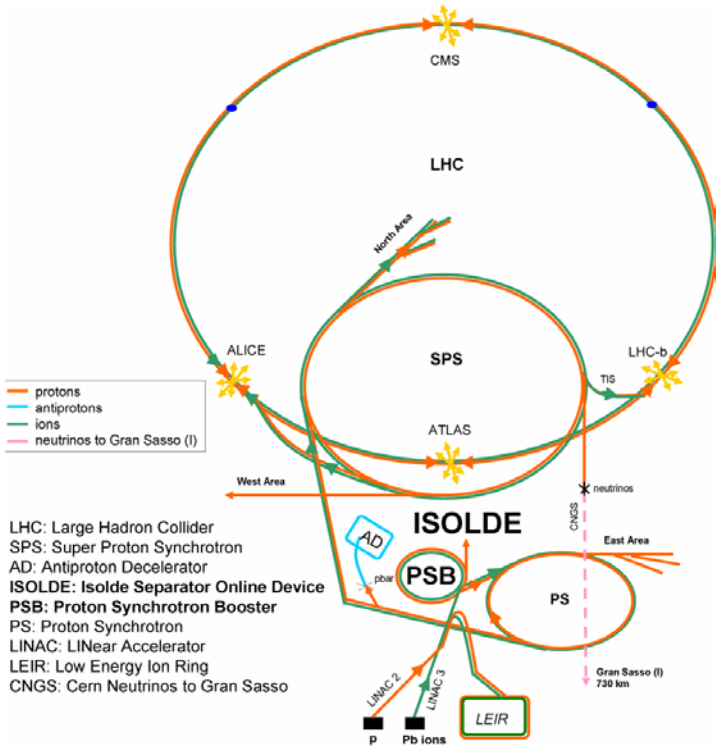

Figure 1.1-1: ***Layout of the PSB at CERN***

The time structure of the pulses enhances the release of the produced radioisotopes from the target and increases the production of short-lived species. On the other hand, the extremely high instantaneous power deposition in the target increases the stress on the target container and the target itself.

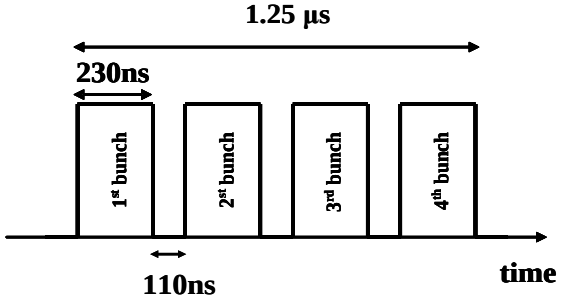

Figure 1.1-2: ***PS Booster time structure for a solid target (different for molten metal targets)***

1.2 Mechanisms of nuclear reactions

1.2.1 Impact parameter, cross section and isotope production

The production of isotopes is mainly done by bombarding a target (**see Section 1.2.2**) with an incident beam of stable ions. Nuclear reactions between a projectile and a target depend on the nature and energy of both the projectile and target and on the impact parameter between these [Hey-99]. This impact parameter, called *b*, is schematically shown on figure 1.2-1. It is the perpendicular distance from the centre of the target to the extrapolation of the trajectory of the particle before it experiences any deflection.

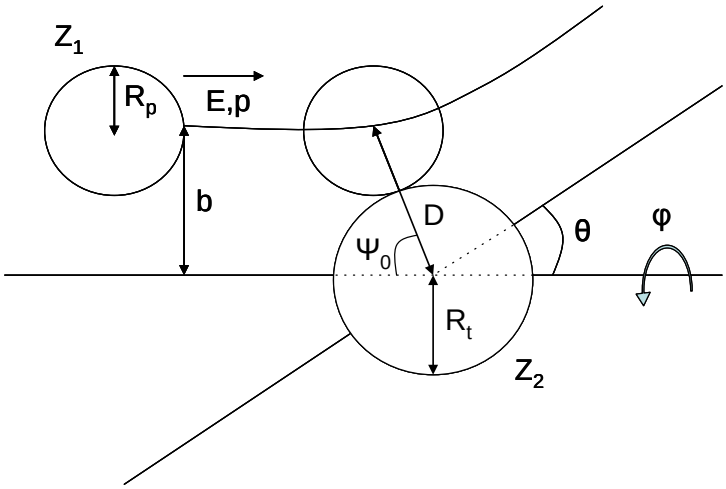

Figure 1.2-1*: Classical trajectory of a charged particle, effective radius R_p and charge Z_1e, incident with impact parameter b at energy and momentum p and deflected through an angle θ by a target nucleus, effective radius R_t and charge Z_2e. D is the distance of closest approach for this trajectory ($D= R_p + R_t$). ψ_0 is the angle at the closest approach.*

Nuclear reactions can be initiated by any type of projectile. Protons, deuterons, alpha particles and other nuclei are positively charged and so require enough energy to overcome the Coulomb barrier. The Coulomb barrier (equation 1.2.1) increases with the atomic number (i.e: number of protons) of the colliding nuclei:

$$V(D) = \frac{Z_1 \cdot Z_2 \cdot e^2}{4\pi\varepsilon_0 D} \cdot \qquad (1.2.1)$$

where ε_0 is the permittivity of free space and D is the distance of closest approach for this trajectory.
There is a value D of the impact parameter, b, which considers a minimal distance between the target nucleus and the projectile nucleus defined as $R_p + R_t$. If $b \leq D$, there is a nuclear collision between both nuclei ($D \leq R_p + R_t$).

When a proton collides with another material, the interaction event between these two is defined by the cross section, σ. It represents the area around the centre of the target nucleus into which the path of the centre of the proton must fall if it is to collide with the target. The

cross section can be divided into three parts σ_e, σ_i, σ_a which are the partial cross section and represent the probability the collision occurs:

$$\sigma = \sigma_e + \sigma_i + \sigma_a \qquad (1.2.2)$$

where σ_e is the elastic Rutherford scattering by the target; σ_i, is the inelastic scattering and σ_a is the absorption by the target.

By using a beam of high energy protons, a larger penetration depth is obtained. However, when the proton energy is increased towards the Coulomb barrier, deviations from Rutherford scattering arise. Depending on the mass of the target element, either an enhancement or a decline of the scattering cross section relative to the Rutherford cross section significantly affects the backscattering analysis at high energies.

The basic assumptions of such a model as described in figure 1.2-1 are:

- The atom contains a nucleus with positive charge Ze.
- The electrically neutral atom contains Z electrons moving around the nucleus.
- The target nucleus is more massive than the incident particle and therefore does not recoil significantly in the collisions.
- The target nucleus and the incident particle have point-like charge distributions so that the Coulomb potential (equation 1.2.1) acts between them.
- No other force is acting other than that due to Coulomb potential.
- No excitation of incident or target particle.

The scattering of a particle in a potential is determined by this impact parameter, b, and the energy of the incident particle, E [Hal-57].

$$b = \frac{Z_1 \cdot Z_2 \cdot e^2}{2E} \cdot \cot(\frac{\theta}{2}) \qquad (1.2.3)$$

Any incident particles entering with impact parameter b and b+db will scatter to the angle θ and θ+dθ. This corresponds to scattering into a solid angle dΩ given by [Lil-01]:

$$d\Omega = 2\pi \cdot \sin(\theta) \cdot d\theta \qquad (1.2.4)$$

Assuming spherical symmetry in ø, the scattering centre presents an effective transverse cross-sectional area of:

$$\Delta\sigma(\theta) = -\frac{d\sigma}{d\Omega}(\theta) \cdot 2\pi \cdot \sin(\theta) \cdot d\theta = 2\pi \cdot b \cdot db \qquad (1.2.5)$$

Equation (1.2.5) can be used to represent graphically the cross section according to the impact parameter (figure 1.2-2).

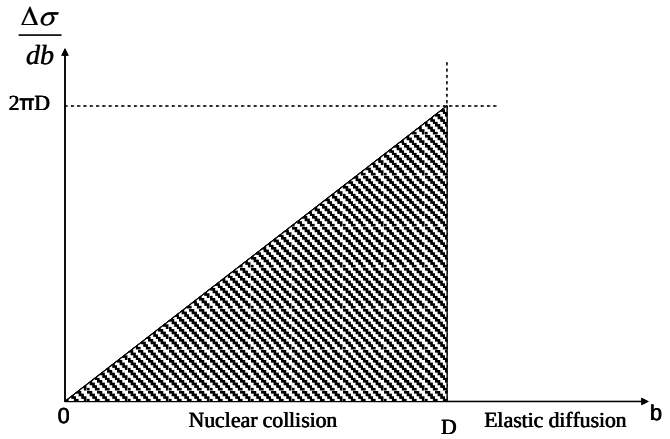

Figure 1.2-2: ***Geometrical representation of the differential total cross section versus the impact parameter b.***

Combining equations (1.2.4) and (1.2.5):

$$\frac{d\sigma}{d\Omega}(\theta) = -\frac{b}{\sin(\theta)} \cdot \frac{db}{d\theta} = \left(\frac{Z_1 \cdot Z_2 \cdot e^2}{16\pi\varepsilon_0 E} \right)^2 \cos ec^4(\frac{\theta}{2}) \quad (1.2.6)$$

which is known as the Rutherford formula for the differential cross section in Coulomb scattering. The cross sections are measured in the unit of barns where 1 barn corresponds to 10^{-24} cm^2. The integration of the differential cross section over the entire solid angle, dΩ represents the total cross section:

$$\sigma_{Total} = \int_0^{4\pi} \frac{d\sigma}{d\Omega}(\theta,\varphi) \cdot d\Omega = 2\pi \cdot \int_0^{\pi} d\theta \cdot \sin(\theta) \cdot \frac{d\sigma}{d\Omega}(\theta) \quad (1.2.7)$$

The total cross section, σ_{Total} is the effective size of the scattering centre for all possible impact parameters.

The inelastic cross section is composed of scattering and reactions terms. Generalised equation for the reaction cross-sections of proton-nucleus interactions was investigated in 1973 by Silberberg and Tsao [Sil-73].
The semi-empirical equation is given by:

$$\sigma = \sigma_0 f(A) f(E) e^{-P\Delta A} \exp(-R\left|Z - SA + TA^2\right|^{\nu}) \Omega \eta \xi \quad (1.2.7b)$$

where f(A) and f(E)are correction factors applicable to products from heavy targets (Z>30), when ΔA is very large. The factor (-PΔA) describes the reduction of cross-section as the difference of target and product mass, ΔA, increases (related to the distribution of excitation energies). The factor $\exp(-R\left|Z - SA + TA^2\right|^{\nu})$ is the distribution of cross sections for the production of various isotopes of an element of atomic number Z. R is the width of the distribution of cross sections and S the location of the peaks of these distribution. T is the shift of the distribution curves towards greater neutron excess as the atomic number of the product increases.
To deduce the production rate in the thin target, the following equation applies:

$$R = N \cdot \sigma \cdot \Phi \quad (1.2.8)$$

where N is the number of atoms per cm^2, σ the cross section (cm^2) and Φ the flux of the projectile (atom/s). The resulting nuclear reactions lead to the production of radioactive residual nuclei. If the cross section of these reactions is known, the number of these residual nuclei can be determined as a function of time during the bombardment.
For N radioactive nuclei, the rate of decay is [Hal-57]:

$$\frac{dN}{dt} = -\lambda \cdot N \quad (1.2.9)$$

according to the decay constant, λ. The solution to equation (1.2.9) is:

$$N(t) = N(0) \cdot e^{-\lambda t} \quad (1.2.10)$$

where N(0) is the number of nuclei at t=0 and λ is equal to $\frac{\ln 2}{t_{1/2}}$ ($t_{1/2}$ being the half-life of the decaying nucleus).

The net rate of increase of the radioactive nuclei is the difference between the rate of production, P, and the rate of decay.

$$\frac{dN}{dt} = P - \lambda \cdot N \qquad (1.2.11)$$

The solution to equation (1.2.11) is:

$$N(t) = \frac{P}{\lambda} \cdot (1 - e^{-\lambda t}) \qquad (1.2.12)$$

Equation (1.2.12) can be used to represent graphically the number of radioactive nuclei, figure 1.2-3:

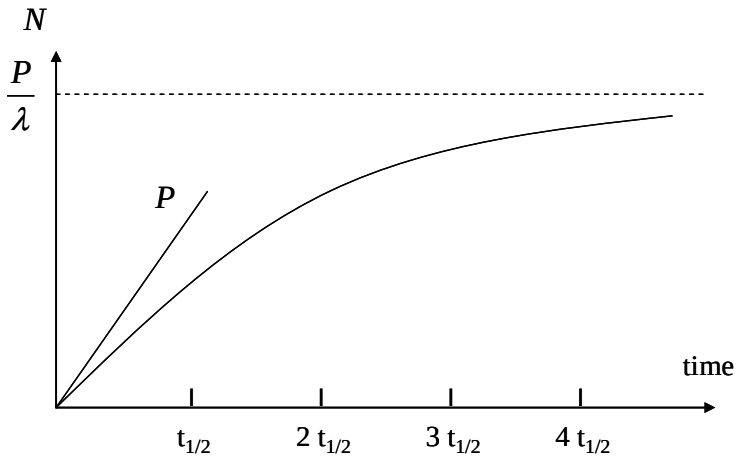

Figure 1.2-3: ***Geometrical representation of the number of the radioactive nuclei produced at a constant rate P.***

1.2.2 Spallation, fission, fragmentation and fusion-evaporation

For a given projectile, different mechanisms of reaction will produce different elements located in the isotopic chart. These reactions depend on the projectile itself, on its energy and the nature of the target. The cross section of the production and the angular distribution of the products of the reaction are the parameters characteristics of this reaction.

Spallation

When a proton is accelerated and strikes a target at energies between hundreds of MeV and a few GeV, it produces multiple collisions with nucleons in a nucleus causing an intranuclear cascade called spallation. High energy particles such as neutrons and protons are emitted in the course of this process and then collide with other nuclei, causing similar reactions (extranuclear cascade). The residual nuclei of the cascade are in an excited state, and light particles are emitted by evaporation of neutrons mainly.

The intensity of the process depends on the number of collisions and then on the impact parameter, b, between the light nucleus and the matter of the heavy nucleus. In these processes about ten fast neutrons are emitted for each proton. From the view point of energy output, the quantity of neutrons thus produced is about one hundred times that of photonuclear reaction and about ten times that produced by fission in a nuclear reactor.

The semi-empirical model of Silberberg and Tsao [Sil73] allows calculating the production cross sections of isotopes produced by spallation. However, this model is reliable mainly for isotopes close to the stability. Models have been created such as the abrasion-ablation model, ABRABLA [Ben-98] (see Section 1.2.3), which describes the formation dynamics of exotic nuclei far from stability and predicts nuclide production cross-sections with a model validated from inverse-kinematics measurements at GSI [Luk-06].

Fission

Fission can be induced by an incident particle that is absorbed by the nucleus of the projectile. The excitation energy generated by this collision leads to longitudinal oscillations. If this energy is sufficiently high, two drops are formed and repulse each other breaking the nucleus in two parts (figure 1.2-4). The nucleus is like a charged droplet and when the deformation reaches a certain critical point, the repulsive Coulomb force driving the deformation overcomes the attractive nuclear force, and the nucleus breaks apart into two large fragments and several neutrons.

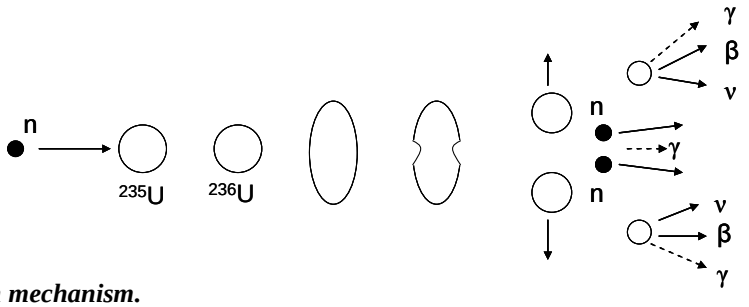

Figure 1.2-4: ***Fission mechanism.***

After separation the two fragments acquire approximatively *170 MeV* of kinetic energy from the Coulomb potential energy as the electric force continues to drive them apart. This forms the bulk of the prompt release of energy in fission. Energy is also carried by neutrons and gamma rays. Many fission fragments are radioactive, because they are formed from a nucleus which has a neutron-to-proton ratio of over *1.5*. The incident particles can be a proton, neutron (generated by the impact of a proton on a converter in Ta or W) or a flux of photons (induced by the impact of an electron of *50 MeV* onto a converter. Nuclear fission is possible for nuclei with large A. It may happen spontaneously, but generally it occurs because some activation energy was sent into the nucleus. To get a nuclear reaction to start, even one that produces useful energy, it is often necessary to give some energy to the system. The energy provided to start a reaction is called the nuclear activation energy.

Fragmentation

Fragmentation is a fast process in which a heavy nucleus fragments. It involves high-energy beams of nuclei being broken up, on a target, into lighter products. Such reactions produce a wide range of nuclei. Due to the high speed of the fragments (typically *60%* of the speed of light) it is difficult to collect useful prompt gamma-ray events. The principal advantage of these reactions is their ability to produce both neutron and proton-rich nuclei and this technique is suited to studies of isomeric decays.
If the impact parameter is large enough, there is a dissipative collision and a fast fragmentation leading to two fragments close from each other of the projectile and of the target (figure 1.2-5).

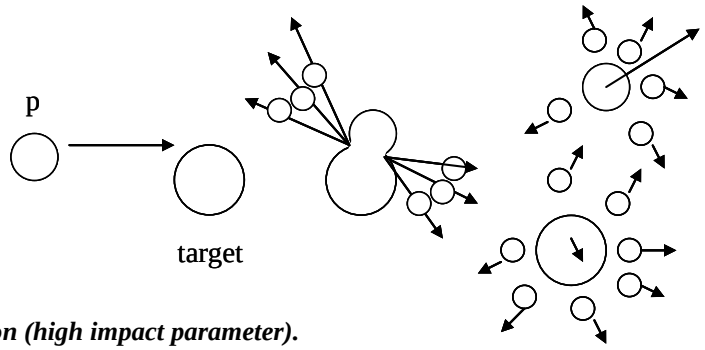

Figure 1.2-5: ***Fragmentation (high impact parameter).***

If the impact parameter is small, the main process induced is the multifragmentation. The projectile and the target dislocate into several lighter fragments.

Fusion- evaporation

The fusion-evaporation reaction is a method of producing highly excited nuclei. In this technique, two stable nuclei are brought together at energy above the Coulomb barrier; the resulting compound system evaporates nucleons before decaying by gamma-ray emission. Such a process produces nuclei on the neutron-deficient side of the stability region. This is because stable light nuclei such as the target and projectile have a lower N/Z ratio compared to the heavy stable nuclei. Moreover the compound system preferentially emits neutrons, leaving a more neutron-deficient nucleus. The alpha and proton emission channels are less probable for heavy compound nuclei near stability. In order to produce nuclei that are more neutron-rich with this technique, radioactive beams (or targets) can be used (such as ^{14}C beam.).

Other reactions

At low energies, the reactions appear as soon as the energies reach the Coulomb barrier or are slightly above (inelastic scattering). For a high impact parameter, collisions will occur between transfer reactions of one or several nuclei. The projectile releases protons to the nucleus of the target (stripping reactions), absorbs neutrons from this target (pick-up reactions) or exchange several nuclei with it (charge exchange reactions). In this process, the nuclei produced at the end will be different from the initial state [Lil-01].

1.2.3 Reactions used at ISOLDE

Spallation, fragmentation and fission (also fission induced by neutron converter) are the three processes used at ISOLDE with protons of *1* to *1.4 GeV* onto thick targets (figure 1.2-6). Due to such energies, the energy distribution is great enough to produce many reactions and hence a large variety of radioactive isotopes.

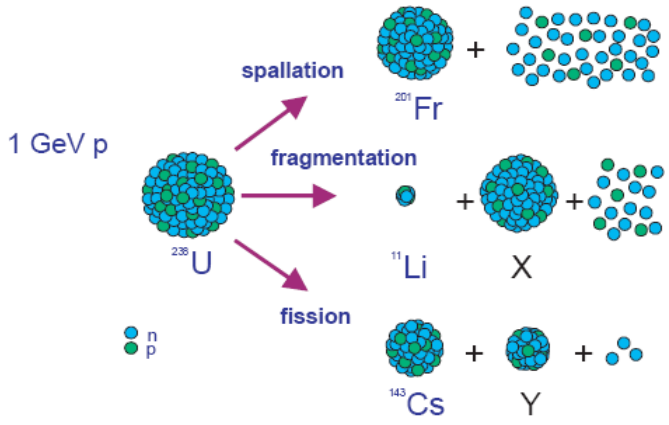

Figure 1.2-6: ***The three processes involved at ISOLDE when sending a 1 GeV proton onto ^{238}U.***

The Monte Carlo Code FLUKA [Fas-03; Fas-05] allows simulating the isotope productions according to the target materials used. FLUKA is one of the existing codes to simulate transport and interaction of particles in matter which is capable of being a complete multipurpose tool. The code is able to treat hadron–hadron, hadron–nucleus, nucleus–

nucleus, neutrino, electromagnetic and also manages interaction and transport of neutrons down to thermal energies.

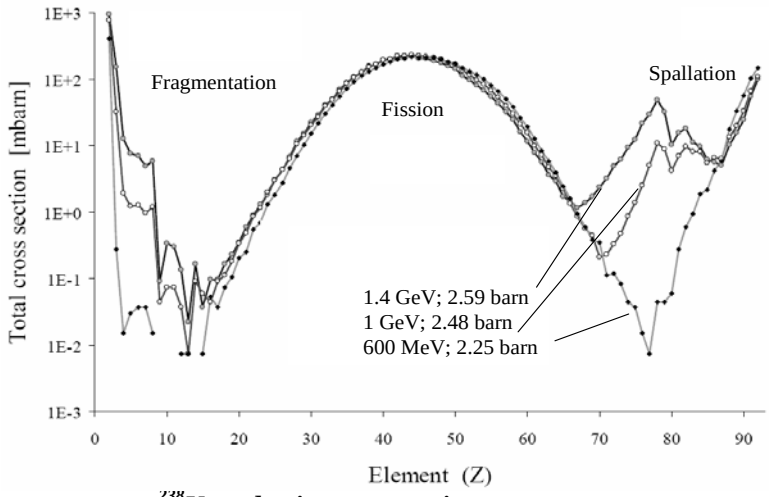

Figure 1.2-7: ***High energy protons on ^{238}U production cross sections.***

Figure 1.2-7 represents the total cross section for different elements obtained from uranium and shows the different nuclear reactions involved.
ABRABLA [Ben-98] (Abrasion-Ablation) has been developed at GSI in the last 10 years and is a Monte-Carlo code that simulates both the nucleus-nucleus and the nucleon-nucleon collisions at relativistic energies assuming that the reaction can be divided in two stages: an interaction stage where the target nucleus loses part of its nucleons and is left in an excited state and a deexcitation stage where evaporation and fission are in competition (thus estimates the cross section with no transport of secondary particles).

1.3 ISOLDE facility

1.3.1 Targets and materials

As seen previously, spallation, fragmentation and fission are the main nuclear reactions involved the production of radioactive isotopes at ISOLDE. Figure 1.3-1 shows a typical ISOLDE target container, which consists of a *20 mm* diameter, *200 mm* long tube of tantalum that can be filled with the target materials.

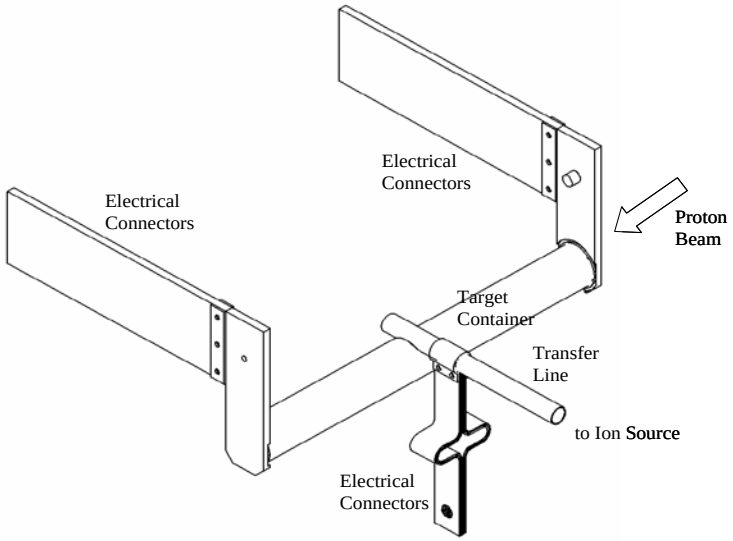

Figure 1.3-1: ***Schematic layout of a standard ISOLDE target and transfer line.***

By ohmic heating up to *1000 A* the target container can be brought up to *2200°C* in order to increase the diffusion process for radiogenic isotopes from the target bulk to its surface from which they desorb. Figure 1.3-2 represents an entire target unit consisting mainly of confinement box, target container and ion source.

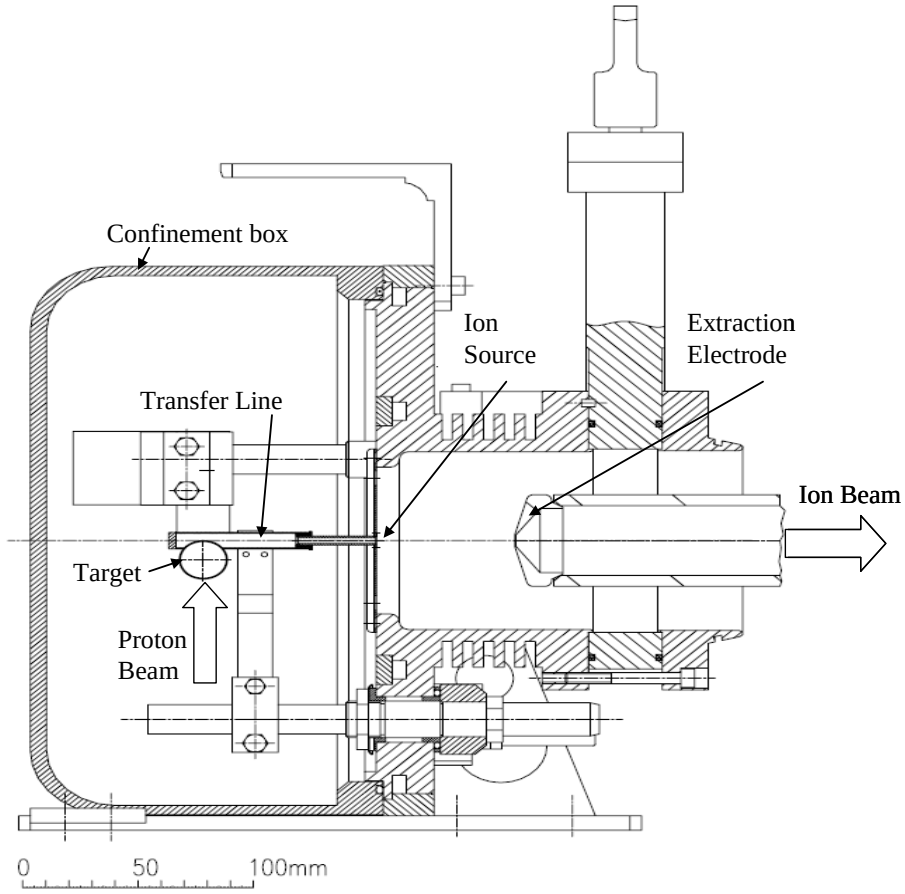

Figure 1.3-2: ***Schematic layout of a standard ISOLDE target-ion source unit.***

The target material must fulfil a number of conditions to be useful for ISOLDE applications. It must be able to provide a rapid and continuous release of the desired product element. The material must lead to the formation of a high cross section for the nuclides of interest; a high release rate (short delay time) in continuous on-line operation; high temperature stability with low vapour pressure at the operating temperature and to a resistance to radiation damage [Car-78; Hof-84]. A limited number of elements is well suited as material for an ISOL target due to the required thermal stability.

- Carbides

Typical carbide targets are: Al_4C_3, SiC, LaC_2, ThC_2, UC_2. This latter is the most used at ISOLDE in combination with positive surface ioniser.

- Oxides

Oxides are mainly used to produce noble gas nuclides. At ISOLDE, ThO_2 (Thoria) is used and shows fast release properties but its limitations (sintering) are strongly dependant on the time that the target is working at operational temperature. Other typical oxide targets used at ISOLDE are: MgO, Al_2O_3, CaO, TiO_2, SrO, ZrO_2, BaO, La_2O_3 and CeO_2.

- Metal foils

Powders and foils of refractory metals are also used as target materials. Typical materials used are: Ti, Nb, Ta and W. Table 1.3-1 shows the different isotopes produced by several kinds of solid target materials at ISOLDE.

Element	T_{max}(°C)	ρ (g/cm^{-3})	ζ (g/cm^{-2})	Isotopes
Nb	*1600*	*4.5*	*25*	*$^{36-46}$Ca, $^{42-48}$Sc*
Ta	*2200*	*16.7*	*110*	*many*
W	*2200*	*19.3*	*7*	*^{8,9,11}Li*
C	*1800*	*2.5*	*73*	*^{7,10,11}Be*
SiC	*1650*	*3.2*	*21*	*$^{17-23}$F, $^{18-24}$Ne, $^{20-24}$Na, $^{22-28}$Mg*
ThC_2	*2200*	*9.0*	*50*	*Many (+ excess of C)*
UC_2	*2200*	*11.3*	*50*	*Many (+ excess of C)*
MgO	*1500*	*3.6*	*2.9*	*$^{17-24}$Ne*
Al2O3	*1550*	*4.0*	*9*	*$^{20-25}$Na*
ZrO2	*1400*	*5.9*	*6*	*$^{48-62}$Mn, $^{56-71}$Cu, $^{62-7}$4Ga*
CeO2	*1300*	*7.1*	*16*	*$^{112-125}$Xe*
ThO2	*2100*	*9.9*	*< 30*	*many*
CaO	*1400*	*3.3*	*5*	*He, C, N, Ne, Ar*

Table 1.3-1*: Overview of solid targets used at ISOLDE [Kos-01]: T_{max} is the maximal temperature of operation, ρ is the density of the material and ζ is the target length.*

- Liquid metal targets

Liquid metal targets are the most efficient production systems for a number of elements. Tin, lanthanum and lead are the typical liquid metals used. In order to produce an optimal release of the isotopes from the container, the temperature is kept high enough to avoid any solidification of the target material. Due to the high target density liquid metal targets can provide the highest intensities for isotopes of certain elements: Cd from a Sn target, Hg from a Pb target and Xe and Cs from a La target. Limitations of these targets come from the large diffusion time constant although shock waves induced by the pulsed proton beam from the PSB lead to shaking of the liquid metal and therefore accelerate diffusion. Special mechanisms are adopted to prevent large quantities of vapour reaching the ion source and to prevent blocking of the transfer line by splashing of the liquid metal target. Table 1.3-2 represents some liquid materials used as targets at ISOLDE and the typical isotopes they produce.

Element	T_{max}(°C)	ρ (g/cm^{-3})	ζ (g/cm^{-2})	Isotopes
Ge	*1100*	*5.5*	*110*	*$^{60-74}$Zn, $^{64-75}$Ga*
Sn	*1200*	*6.4*	*128*	*$^{97-122}$Cd*
La	*1400*	*6.2*	*124*	*$^{114-137}$Cs, $^{115-133}$Xe*
Pb	*800*	*10.1*	*200*	*$^{177-207}$Hg*
Bi	*600*	*9.6*	*190*	*Hg*
U	*1700*	*17.6*	*350*	*Kr, Cd, I*

Table 1.3-2*: Overview of liquid metal targets used at ISOLDE [Kos-01]: T_{max} is the maximum temperature of operation, ρ is the density of the material and ζ is the target length.*

Normally only volatile elements with a low desorption enthalpy are released from liquid targets. The average release times from liquid targets are typically of the order of minutes [Let-97].

1.3.2 Transfer lines

The only orifice of the target container is connected to the ion source via a transfer line (figure 1.3-3). By control of the temperature of this transfer line chemical selectivity may be achieved by means of condensation for a specific element or selective adsorption (isothermal chromatography) for a specific material. Therefore the temperature of the transfer line is chosen according to the target material and the species studied. Three different transfer lines are classically used at ISOLDE and are usually made of Ta: when linked to an MK5 (or MK1) 'Hot Plasma' ion source (**see Section 1.3.3**) the transfer line operates at high temperature (*1900°C*) to allow the ionisation of less volatile elements; when linked to a MK7, 'Cold Plasma' ion source, the transfer line is kept at room temperature by a water-cooling system to condense all elements and release volatile species such as noble gases and N_2.

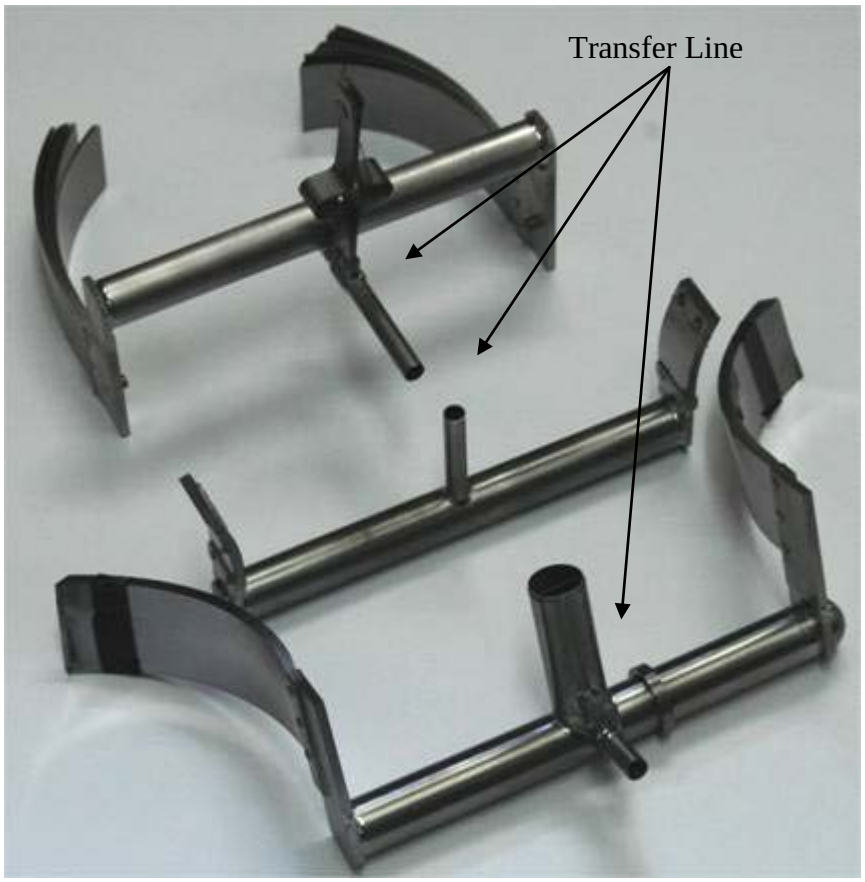

Figure 1.3-3: ***Pictures of three different transfer lines used at ISOLDE.***

Transfer lines are also used at intermediate temperatures (between *200°C* and *400°C*) to allow the suppression of less volatile species that may affect the purity of the ion beam released from the unit. In this case, when linked to a MK3 or MK1-2 surface ion sources, the retention of specific elements such as isobaric contaminants can be improved by the addition of a material in the line. This latter aspect is the subject of **Chapter 3** of the present work.

1.3.3 Ion sources

Once the radioactive elements are produced by the nuclear reactions, they are ionised. At ISOLDE, three types of ion sources can be used to ionise the isotopes.

- Surface ionisation sources

The concept of surface ionisation has proven to be particularly successful for production of singly charged positive and negative radioactive ion-beams due to its simplicity, high efficiency and selectivity.

An atom interacting with a metal surface will be positively ionised if the work function of this surface is greater than the ionisation potential of the atom. On the contrary, if the work function is less than the electronic affinity of the atom, then there is a change in the polarity of the ionisation (Negative ion source). Surface ionisation is described by the degree of ionisation, α, which is defined by the ratio of ions, n_i, leaving the surface to the neutral atoms, n_0, leaving the surface of the material [Zha-99].

$$\alpha = \frac{n_i}{n_0} \qquad (1.3.1)$$

At a thermodynamic equilibrium, the degree of surface ionization as a function of surface temperature is given by the Saha-Langmuir equation [Lan-25].

$$\alpha = \frac{g_0}{g_1} \cdot e^{(W-\varphi_i)/kT} \qquad (1.3.2)$$

where g_i and g_0 are the statistical weights of the ion and atom states (for the alkali metals, $g_i/g_0 = ½$), φ_i is the ionisation potential of the atom, W is the work function of the metal, and T is the surface temperature.

Table 1.3-3 represents calculated values of degree of ionisation, α, on a tungsten surface.

			Temperature (K)			
Adsorbate	$\varphi_{i\,(eV)}$	W- $\varphi_{i\,(eV)}$	1000	1500	2000	2500
Cs	3.88	0.64	790	72	19.9	9.8
K	4.32	0.20	6.3	2.16	1.60	1.27
Na	5.12	-0.60	$5x10^{-4}$	$5x10^{-3}$	$1.58x10^{-2}$	$3.16x10^{-2}$
Li	5.40	-0.88	$1.8x10^{-5}$	$5.5x10^{-4}$	$3.0x10^{-3}$	$8.4x10^{-3}$

Table 1.3-3*: Calculated values of degree of ionisation on a tungsten surface (MK1) [Zha-99].*

The ionisation efficiency is the ratio of n_i to the number of the arrival flux of atoms, n. [Lan-25]

$$P_i = \frac{n_i}{n} \qquad (1.3.3)$$

For a steady equilibrium state the total evaporation rate is:

$$n = n_0 + n_i \qquad (1.3.4)$$

Thus

$$P_i = \frac{n_i}{n_0 + n_i} = \frac{\alpha}{1+\alpha} = (1 + \frac{g_0}{g_i} \cdot e^{e(\varphi_i - W)/kT})^{-1} \qquad (1.3.5)$$

Table 1.3-4 presents some ionisation efficiencies according to the temperature of the hot metal plate [Wol-95].

Adsorbate	Hot Metal Plate	Temperature (K)	P_i
K	*Pt*	*1500*	*1.0*
Cs	*W*	*1500*	*0.99*
Ba	*Re*	*2200*	*0.12*

Table 1.3-4*: Calculated values of ionisation efficiencies of alkalis over metal surface.*

Efficiencies of *50-100%* may be obtained for elements with ionisation potential below *5eV* (positive ions) and above *2eV* (negative ions) depending on the surface material. With a constriction made of tantalum kept at a temperature of *1000°C* the alkali K, Rb, Cs, and Fr are selectively ionised with an efficiency of about *90%*. If the constriction is lined with a Re foil and heated to *1700°C*, it also ionises alkaline earths Ba and Ra with *10* to *50%* efficiency [Bio-86]. Figure 1.3-4 shows the schematic layout of a surface ion source.

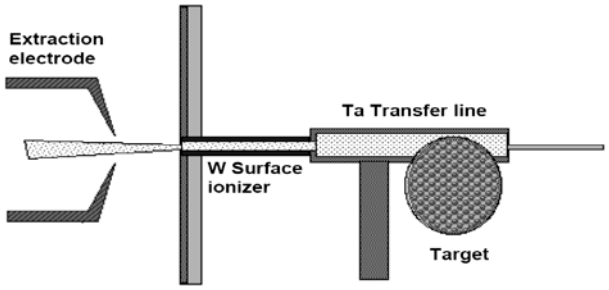

Figure 1.3-4: ***Schematic layout of a surface ion source (MK1).***

At ISOLDE, typical surface ion sources use a LaB_6 surface for a selective production of halogens. Due to its low work function (W= *2.6 eV*), elements having a high electron affinity such as halogens are ionized with high selectivity [Iso-00].
Another interest of this kind of ion sources is the possibility of adaptation to complex target geometry and getting an efficiency of *1.0* if the work function, W is greater than φ_i by at least *1 eV*.

- Plasma ion sources

The plasma ion sources such as Electron Cyclotron Resonance (ECR) are used to ionise elements not surface-ionisable. Ions are produced in a magnetically confined plasma, which is heated by microwaves. The plasma can be practically defined as: "*a quasi-neutral gas that exhibits collective behaviour when exposed to external electromagnetic fields*" [Wol-95]. It also exhibits collective behaviour via long range Coulomb interaction. There is no well-defined phase transition point from the gaseous state to plasma that consists of electrons, ions and neutral atoms or molecules. The most significant difference between a plasma and a neutral gas is the number of freely moving charges that make the plasma a good conductor. A plasma also has properties that are characteristic of liquids. An ionised gas can be considered as a plasma if the following so-called plasma conditions are fulfilled:

- The typical length scale (dimension) *L* of the plasma has to exceed its shielding length λ_D (Debye length). The Debye length determines how far the charge imbalance due to thermal motion in the equilibrium state or the impact of an external electric potential can extend in the plasma or in the ionised medium. The condition can be written for electrons as [Wol-95]:

$$L >> \lambda_{De} = \sqrt{\frac{\varepsilon_0 \cdot kT_e}{e^2 \cdot n_e}} \qquad (1.3.6)$$

where ε_0 is the permittivity constant ($\approx 8.854 \cdot 10^{-12}$ F/m), k the Boltzmann constant ($\approx 1.38 \cdot 10^{-23}$ J/K), T_e the electron temperature (in Kelvin), e the elementary charge

($\approx 1.602 \cdot 10^{-19}$ C) and n_e, the electron density. If this condition is not met, the plasma is not necessarily macroscopically neutral.

- In order to have collective behaviour, the number of particles inside the Debye sphere must be sufficient such as:

$$n_e \cdot \lambda_D^2 >> 1 \qquad (1.3.7)$$

- The frequency f_{pe} of collective plasma (electron) oscillations must be higher than the collision frequency ν_{en} of electrons and neutrals

$$f_{pe} = \frac{\omega_{pe}}{2\pi} = \frac{1}{2\pi} \cdot \sqrt{\frac{e^2 \cdot n_e}{\varepsilon_0 \cdot m_e}} > \nu_{en} \qquad (1.3.8)$$

where m_e is the electron mass ($\approx 9.11 \cdot 10^{-31}$ kg). Equation (1.3.8) defines the plasma oscillation frequency ω_{pe}. If this plasma condition is not valid, there are no collective phenomena and the dynamics of the system is dominated by the motion of neutrals. This condition is fulfilled as the degree of ionisation of the plasma increases. Usually the ionised gas can be considered to be a plasma when its degree of ionisation exceeds a few percent [Sti-92].

FEBIAD Ion Sources:

Forced Electron Beam Induced Arc Discharge (FEBIAD) sources are slightly different from plasma ion sources but are the most used at the ISOLDE-CERN. FEBIAD sources exhibit a large range of weak charge density which is at the lower limit of a plasma parameters' as defined previously. They were developed in order to ionise several kinds of nuclei produced from an ISOL technique and they allow efficient ionisation at low pressure [Kir-76, Kir81a]. Electrons are produced by heating the cathode. This is known as the thermionic emission principle. The density of emission depends on the work function of the material and of its temperature (for condensable elements). Typically, cathodes are made either of tungsten or tantalum as they have relevant thermoelectronic properties.
The electron flux produced by the cathode is directed to the ionisation chamber which is under low pressure [Kir-76]. The discharge region has a volume of a few cm^3. The ionisation is produced by the collisions of electrons with elements coming from the target via the transfer line. In general, pressure is under 10^{-5} *mbar*.
Several kinds of plasma ion sources are used at ISOLDE defined as 'hot' and 'cold' plasma ion sources. This actually refers to the temperature of the transfer line inside which the isotopes are effusing. Figure 1.3-5 represents a 'hot plasma ion source' operating with a transfer line at *1900°C*. This ion source is efficient for refractory elements [Iso-00].

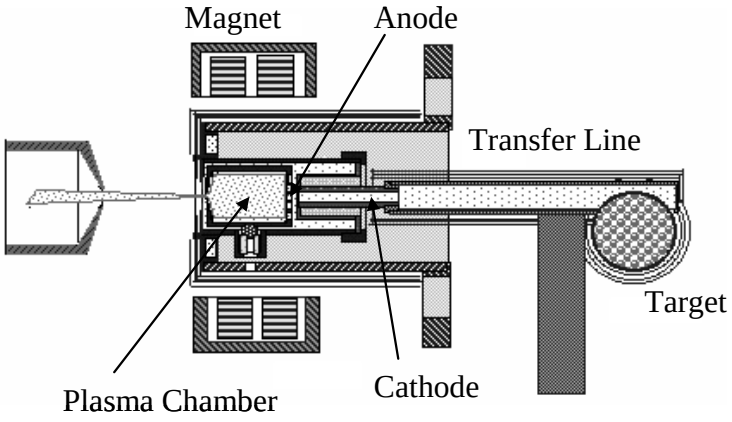

Figure 1.3-5: ***Schematic layout of a Plasma ion source with hot transfer line (MK5).***

The 'cold plasma ion source' is used for the production of noble gas isotopes. The transfer line bringing the operating temperature to *50°C* is cooled continuously by a water flux (figure 1.3-6). Cooling the line suppresses the less volatile elements and reduces the unwanted isobaric contamination in the ISOLDE radioactive ion beams and therefore allows selectivity [Iso-00]. The temperature of the line depends on the element to be studied.

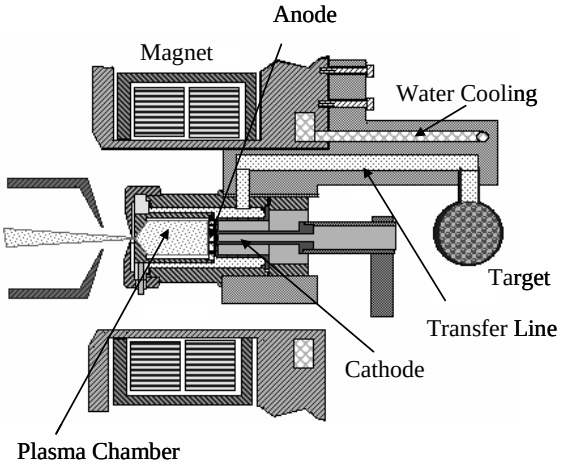

Figure 1.3-6*: Schematic layout of a Plasma ion source with cold transfer line (MK7).*

Another kind of plasma ion source (MK6) operates a transfer line at a temperature going up to *400°C* to produce elements with intermediate to low vapour pressure. Table 1.3-5 shows different efficiencies for the FEBIAD ion sources [Sun-92].

Element	Ion Source Type	Efficiency (%)
He	MK7	0.5
C	MK6	0.1
N	MK7	0.1
O	MK7	0.1
F	MK7	1
Ne	MK7	1
Ar	MK7	10
Kr	MK7	20
Xe	MK7	40
Hg	MK5	42
Pb	MK6	60

Table 1.3-5*: Value of ionisation efficiencies for the different plasma ion sources.*

The advantages of the plasma ion source are the following:

- High efficiencies (20 - 60 %) for Z > 20.
- Stable operation with little support gas ($2x10^{-5}$ mbar).
- Low ion current density (0.1 $mA.cm^{-2}$).
- Good emittance (< 20 π mm mrad at 15 kV).
- Low energy spread (< 2 eV).

Recently an efficient ion source that can accommodate the 50-fold increase in proton beam intensity that will become available at CERN through the upcoming Linac 4 and Superconducting Proton Linac upgrades has been developed: the Versatile Arc Discharge Ion Source (VADIS). The VADIS sources are improved FEBIAD ion sources, based on the optimization of the electronic and ionic loss currents inside the ion source. They are the result of the development of an improved model for the ionization efficiency, based on extensive experimental data and confirmed by analytical analysis and simulations [Liv-09].
VADIS was employed at ISOLDE in 2008 with spectacular results. The experiment in question involved another pioneering facility, ISOLTRAP.

ISOLTRAP first weighed isotopes of Xenon ionized by VADIS, determining masses for four more of them. The team then focused its efforts on the neutron-rich isotopes of radon, with impressive results. The experiment determined seven new masses, one for an isotope, ^{229}Rn, that had never been observed in the laboratory before.

- Laser ion sources

The Resonance Ionisation Laser Ion Source (RILIS) at ISOLDE is based on the selective excitation of atomic transitions by tunable laser radiation. Ion beams of isotopes of 20 elements have been produced using the RILIS setup. It consists of copper vapour lasers and dye lasers that ionise the atoms which are confined in the hot cavity of the source. After being released from the target, the produced isotopes diffuse through a tube heated between *1800°C* and *2200°C*: then two or three laser beams are sent collinear to the cavity axis for the ionisation of the elements (figure 1.3-7). Two and three-step excitation schemes are used, providing an ionisation of about 10%. Operation of the laser ion source at ISOLDE is described in [Fed-00, Fed-06, Mis-92].

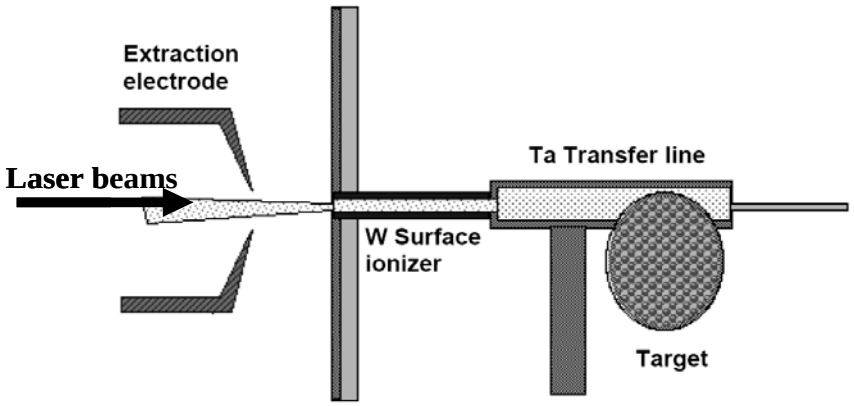

Figure 1.3-7: ***Schematic layout of ionisation by RILIS.***

Table 1.3-6 represents the excitation wavelengths (λ_1, λ_2 and/or λ_3) used for each element ionised, their efficiency and the atomic ionisation energies (E_1). Table 1.3-7 summarises which elements can be ionised according to the type of the ion source used.

Element	E_1 (eV)	λ_1 (mm)	λ_2 (mm)	λ_3 (mm)	Efficiency (%)	Produced ion beams (mass number)
Be	*9.32*	*234.9*	*297.3*	-	*>7*	*7, 9-12, 14*
Mg	*7.65*	*285.2*	*552.8*	*578.2*	*9.8*	*off-line*
Mn	*7.44*	*279.8*	*628.3*	*510.6*	*19.2*	*49-69*
Ni	*7.64*	*305.1*	*611.1*	*748.2*	*>6*	*56-70*
Cu	*7.73*	*327.4*	*287.9*	-	*>7*	*56-78*
Zn	*9.39*	*213.9*	*636.2*	*510.6*	*4.9*	*58-73*
Ag	*7.58*	*328.1*	*546.6*	*510.6*	*14*	*101-129*
Cd	*8.99*	*228.8*	*643.8*	*510.6*	*10.4*	*98-132*
Sn	*7.34*	*300.9*	*811.4*	*823.5*	*~9*	*109-137*
Tm	*6.18*	*589.6*	*571.2*	*575.5*	*>2*	*off-line*
Yb	*6.25*	*555.6*	*581.1*	*581.1*	*15*	*157-167*

Table 1.3-6*: Values of ionisation efficiencies when using the RILIS [Fed-00].*

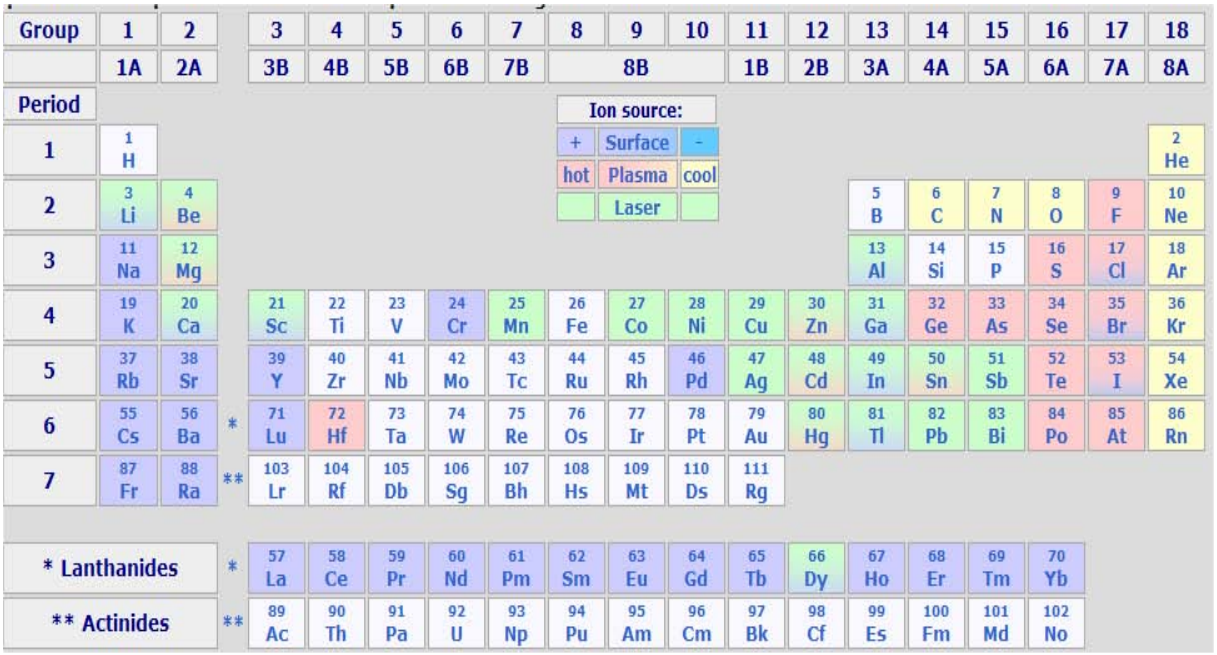

Table 1.3-7*: Ionised elements according to the type of the ion source at ISOLDE [Iso-00].*

1.4 Mass separation

At ISOLDE, the target-ion source unit is connected to a target station referred to as the 'Front End'. The radioactive ion beam is extracted from the ion source by the extraction electrode, the beam is accelerated at a potential of few kV and sent to the experimental hall (figure 1.4-1). The diagnostics of the beam is made using Faraday cups and scanners in order to maximise the transmission.

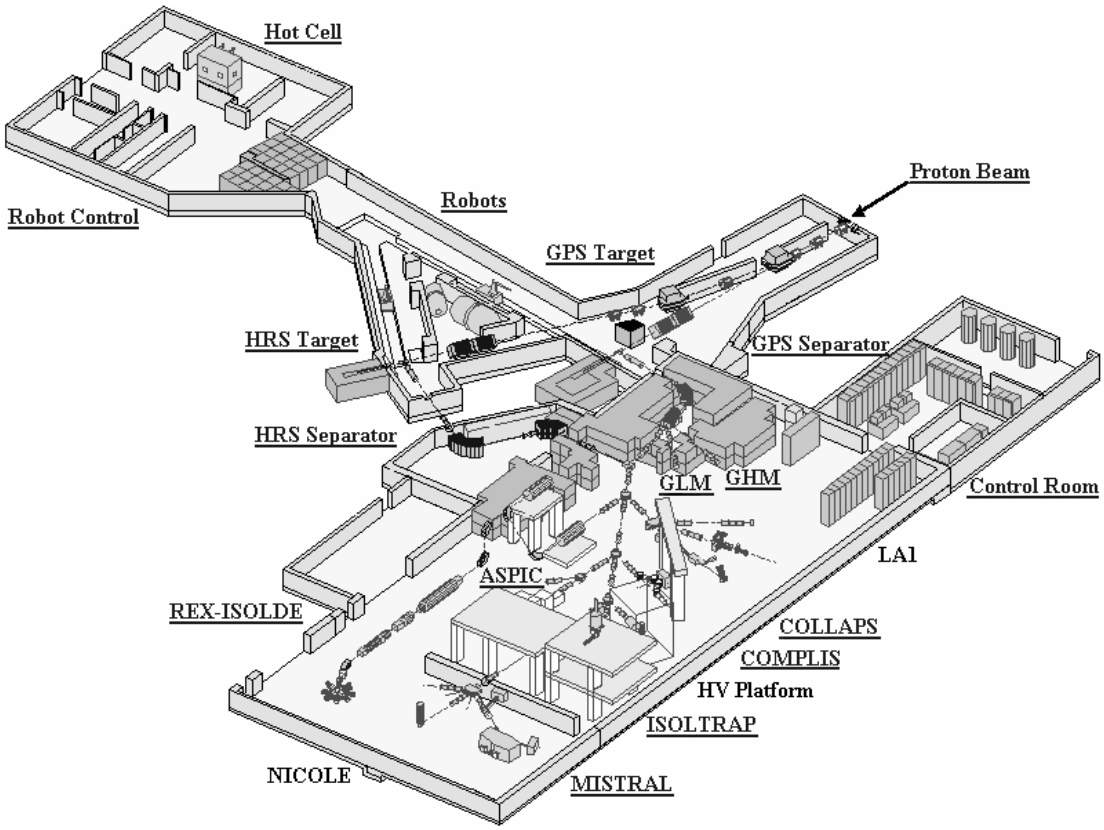

Figure 1.4-1: ***Layout of the ISOLDE facility [Iso-00].***

ISOLDE operates two mass separator systems, HRS (High Resolution Separator) and GPS (General Purpose Separator) [Iso-00]. Beam distribution is done by other elements such as kickers, deflectors, electrostatic deflectors, and switchyard.

- HRS

  The HRS (figure 1.4-2) consists of two magnets (magnets with bending angles of *90°* and *60°* respectively), electrostatic quadrupole lenses and a number of magnetic and electrostatic elements for correction of higher order image aberrations [Iso-00]. The separator delivers one mass at a time to the experimental hall. At the exit of the dispersive and focussing system, the separation Δx between two beams of different mass m and $m + \Delta m$ is expressed by:

$$\Delta x = D \cdot \frac{\Delta m}{m} \qquad (1.4.1)$$

  where D is the dispersive coefficient. For the HRS, $D = 2.7\ m$.
  The resolving power is expressed by [Iso-00]:

$$P_R = \frac{\Delta x}{\delta x} \cdot \frac{\Delta m}{m} = \frac{D}{\delta x} \qquad (1.4.2)$$

where δx is the length of the image in the focal plan. Therefore, a *1 mm* large image will be obtained with a resolution of *2700*.

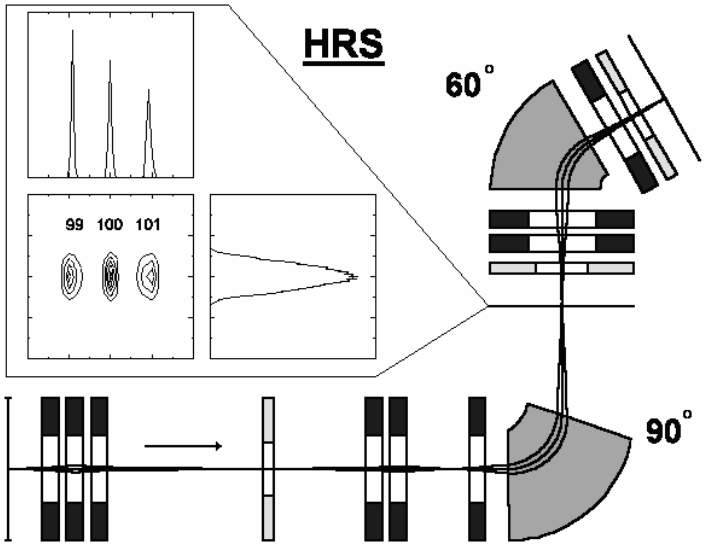

Figure 1.4-2: ***HRS Layout [Iso-00].***

- GPS

The GPS (figure 1.4-3) allows the selection of three different beams within a certain range of mass that it can deliver simultaneously into the experimental hall through three different beam lines (central mass, low mass and high mass beam line). The magnet is a double focusing H-magnet with a bending angle of *70°* and a mean bending radius of *1.5 m*. The mass resolving power is *m/Δm=2400* (for 20 mm mrad beam). The selection of mass is achieved by moving the deflector plates parallel to the focal plane. To make best use of the space in the experimental hall both side beams are taken out to the left of the central mass. These two side beam lines serve mainly for ion collections and small size experimental set-ups.

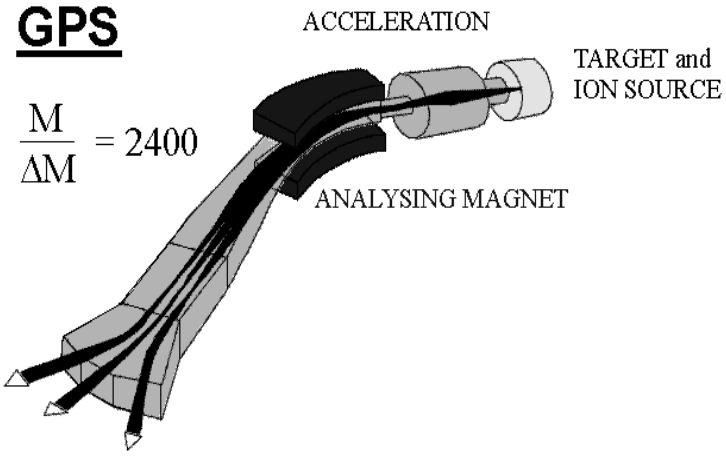

Figure 1.4-3: ***GPS Layout [Iso-00].***

The magnetic field is set to select the ions of a chosen mass and steer them in the beam line through the beam gate. Release measurements are made using a tape station [Tur-08]. It consists of a metallic mylar tape and two detectors (plastic scintillator and c-detector). The radioactive beam is deposited on the metallic band and when the atoms hit the band they penetrate into the material. Then they are transported in front of the detectors. The beam gate is opened after a defined time after proton impact (t_{delay}) and it is held open for a given time ($t_{collection}$). The beam gate is then closed and the tape moved to the detectors. The detectors measure for a defined time ($t_{measurement}$). The values of $t_{collection}$ and $t_{measurement}$ are set (depending on the half-life and production rate of the isotope) to obtain enough statistics and not to saturate the detectors. The delay time t_{delay} is changed to obtain the release curve point by point. This procedure is repeated typically 20 times.

1.5 Physics at ISOLDE

A large variety of ions species allows the systematic study of atomic and nuclear properties and exotic decays over long isotope chains. The experiments carried out at ISOLDE employ the state-of-the-art instrumentation (figure 1.4-1). Instruments such as for laser spectroscopy are used by COLLAPS and COMPLIS. The NICOLE experiment carries out nuclear orientation studies of exotic nuclei. ISOLTRAP is a triple-trap spectrometer able to give accuracy approaching 10^{-8} in mass measurements of unstable nuclei. GLM and GHM beam lines are used for collecting radioactive samples for research in solid-state physics and biophysics. Electro-weak interaction is studied by a retardation spectrometer called WITCH: it also searches for physics beyond the Standard Model through nuclear beta-decay [Iso-00].
A most important feature of ISOLDE is the post-accelerated beams with the REX-ISOLDE charge breeder and linear accelerator. REX makes use of the large variety of radionuclides that have been extracted from the on-line mass separator ISOLDE. The radioactive singly-charged ions from the separators are first accumulated, bunched and cooled in a Penning trap, REXTRAP. REX-ISOLDE currently provides beams of energy *3.1 MeV/u* (up to masses *230*) into the super-efficient, highly segmented gamma-ray MINIBALL array at the secondary target position.

Chapter 2

Fundamental Processes Affecting the Release of Isotopes to Produce a RIB

The main objective of the ISOL technique is the production of beams of exotic nuclei that are abundant, pure and variable in energy. From the moment the proton beam hits the target to the measurement of the radioactive ion beam after the separators each part of the production chain plays an important role in delivering a satisfactory isotopic yield [Rav-98].
The target system has to be able to dissipate the power deposition of the primary beam and allow the production of the secondary particles in the material. An optimised beam-target combination is mandatory to obtain a high production rate (high production cross section and "thick" target). Before being extracted the isotopes effuse out of the target through the transfer line and are ionised by the ion source. Nevertheless, several processes along this chain affect the release properties of isotopes to produce a RIB: these are due to release losses in the target, condensation phenomenon in the transfer line and in the ion source, molecular sidebands and decay losses.

2.1 Beam purity

Most of the RIBs extracted from an ISOL-type target are contaminated with isobars and isotope selection by mass separation alone is often limited by the ion source emittance combined with the mass resolution of the separator magnet, an additional chemical selectivity is mandatory. When the nuclear reactions occur, some nuclei are produced among those of interest and certain have the same mass-over-charge ratio. The ratio of the desired yield from these RIBs to all others, including molecular side bands and multiple charge states is defined as ''beam purity''. This concept was first introduced in 1988 [Rav-88].
Nowadays development of efficient beam purification techniques has become a focus for different RIB facilities:

- The Holifield Radioactive Ion Beam Facility (HRIBF) produces isobarically pure beams of neutron-rich Sn and Ge from a UC target: the isotope of interest is extracted as a sulphide molecular ion and the molecule is dissociated. Then the negatively-charged ion is formed in a Cs-vapor charge-exchange cell before being injected into post accelerator [Str-03].

- LIST (Laser and Ion Source and Trap) at Johannes-Gutenberg-Universität of Mainz consists of a laser ion source and a linear Paul trap to produce RIBs: the atoms exiting the source are selectively ionised by the lasers [Sch-08].

- ISOLDE and TRIUMF use the ionisation schemes such as provided by Resonant Ionization Laser Ion Source (RILIS) (known to be one of the most selective type of ion sources) [Fed-06]. Hovewer, isobaric contamination occurs by surface ionisation of low ionisation potential elements in the RILIS high temperature cavity. As an example, Uranium Carbide targets release isobaric contaminants such as alkalis (Cs, In) when studying an isotope of interest (i.e. Cd) (**see Chapter 3**). Pure beams at ISOLDE can also be obtained by chemically selective steps such as isothermal chromatography lines [Bjo-86] investigating the chemical nature of the elements (adsorption/desorption enthalpies; surface purities); or separation of molecular sidebands [Kir-75]. To enhance the ratio of the desired isotope over the 'unwanted' elements, neutron converter, Positive [Kir-90] and negative [Vos-81] surface ionisation sources also provide pure beams of elements with low ionisation potential or high electron affinity, respectively. The cross sections, the nature of the projectile and its flux have a strong influence onto the beam purity as well as the efficiencies of the ion sources and the mass separation processes (as discussed earlier).

The ISOLTRAP [Bol-96] experiment is a tandem Penning trap system for accurate on-line mass determination of isotopes and suffers from isobaric contaminations. Conventional techniques of purification does not prevent ISOLTRAP to obtain Fr-to-Tl yield ratios from

100 (mass 207) to 10^4 (mass 212) [Kow-07]. An additional purification method, subject of chapter 3 of the present manuscript, is required.
The release fractions of the elements constitute an important parameter to define the purity of a beam as it includes the diffusion-effusion process (**see Sections 2.3 and 2.4**).

2.2 Release properties and decay losses through a target-ion source unit

The RIB intensity I_{RIB} produced by the ISOL method can be expressed, in the thin target approximation, as [Rav-79]:

$$I_{RIB} = (\sigma_{prod} \cdot N_{target} \cdot I_{prim-beam}) \cdot \varepsilon \qquad (2.2.1)$$

- σ_{prod} is the isotope cross section production (cm^2) by interaction with the primary beam, $I_{prim-beam}$ its intensity (particle/s) and N_{target} the target thickness (atom/cm^2). Since the cross section is energy dependent and the primary beam looses energy while passing through the target, the intensity has to be calculated by integrating over the target thickness taking into account the energy loss of the beam.

- ε is the efficiency regrouping a series of specific efficiencies through the ISOL chain. It is defined as the ratio of the final secondary beam intensity (I_{final}) that arrived at the experimental set-up versus the intensity of the reaction products (I_{prod}):

$$\varepsilon = \frac{I_{final}}{I_{prod}} = \varepsilon_{release} \cdot \varepsilon_{ion} \cdot \varepsilon_{transp} \cdot \varepsilon_{post-acc} \qquad (2.2.2)$$

  $\varepsilon_{release}$, ε_{ion} and $\varepsilon_{post-acc}$ represent the released fraction from the target unit, the ion source efficiency, and the post-accelerator efficiency, respectively. ε_{transp} is the efficiency of the mass analysis and transport to the experimental set-up.

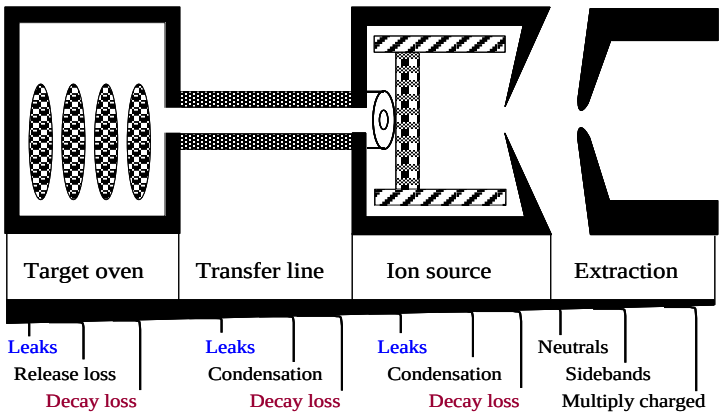

Figure 2.2-1: ***Layout of the ISOLDE concept of an ion source connected via a short transfer line to a thick target [Rav-79].***

The parameter $\varepsilon_{release}$ expresses the relative amount of ions that survive from the moment of their production in the target to the moment of their extraction from the ion source (figure 2.2-1). This so-called release time is the result of the diffusion from the target material, the desorption from the material surface and the effusion through the transfer line to the ion source.

To quantify the loss factors a delay-time distribution, *P(t)*, is defined as:

$$\varepsilon_{release}(t,\lambda_i) = \int_0^\infty P_i(t,\lambda_i)\cdot dt = \int_0^\infty P(t)\cdot \exp(-\lambda_i t)\cdot dt \qquad (2.2.3)$$

with λ is equal to $\frac{\ln 2}{t_{1/2}}$. Here $P(t)\cdot dt$ represents the probability for an atom of a given element created at *t=0* to be released from the ion source between time t and *t + dt*. Eq. (2.2.3) exclusively depends on the chemical and physical properties of the element, the temperature, geometry and the material of the unit.
The fraction of the atoms produced at *t=0* which have escaped from the target-ion source unit after a time *t* is expressed as the fractional release function *F(t)*:

$$F(t) = \int_0^t P(t')\cdot \exp(-\lambda t')\cdot dt' \qquad (2.2.4)$$

For an infinite value of $t_{1/2}$, $\varepsilon_{release}(t_{1/2}) = 1$. This means that all produced atoms have escaped from the target unit at the end. Therefore the average of the delay time is given by:

$$\tau_{delay} = \int_0^\infty t\cdot P(t)\cdot dt \qquad (2.2.5)$$

Typically, the release measurements which are expressed in β-counts per unit of time are converted into yield (1/μC): ratio of the average ion beam intensity (1/s) by the average proton beam current (1/μA) [Let-97]:

$$Y = \frac{N_{0i}}{N_p}\cdot 6.2\times 10^{12}\cdot \int_0^\infty P_i(t,\lambda_i)\cdot dt \qquad (2.2.6)$$

where N_{0i} is the number of ionised isotopes created by one proton pulse of N_p protons. The parameters from the experimental data are computed and fitted (cross section) to provide an estimation of the yield for a given isotope.

2.3 Diffusion process

The main parameters which influence the diffusion process to take place are the temperature of the target, the concentration of the radioactive element involved, the microstructure, impurities and the crystalline structure.
According to the first Fick's law [Gli-00]:

$$\vec{J}(p,t) = -D(p,t)\cdot \overrightarrow{Grad}(C(p,t)) \qquad (2.3.1)$$

where J represents the flux density vector, in $m^{-2}s^{-1}$, of the radioactive element per surface and time unit. In a specific point, p, and at a time t. D(p,t) is the diffusion coefficient, in m^2s^{-1}, at a point p of the target and at a time t. D depends on the nature of the diffusing atoms, of the target and on the temperature [Gli-00]:

$$D(p,t) = D_0(p,t)\cdot e^{\frac{-E_a(p,t)}{k_b\cdot T(p,t)}} \qquad (2.3.2)$$

D_0 (m^2s^{-1}) and E_a (en eV) are the Arrhenius coefficients.

Supposing that the temperature is homogeneous and constant in the target, therefore T(p,t) is independent from p and from t. $E_a(p,t)$ represents the energy for a radioactive atom to diffuse.

The ratio E_a by k_bT shows the importance of the thermal energy in the system. The higher the temperature is, the smaller the ratio between both terms is and the higher the diffusion coefficient is. $D_0(p,t)$ is the frequency factor and depends of the crystalline structure and of lattice vibrating period of the diffusing atom. The frequency factor also depends of the radioactive element which is under study, and more particularly of the concentration of the impurity present with this element. Indeed, impurity affects the diffusion process: an element with high impurity will tend to saturate sites and therefore make difficult the atom to diffuse. Supposing that this impurity level is very low from the element of interest, there $D_o(p,t)$ is independent from *p* and *t*. Thus the first Fick's law becomes:

$$\vec{J}(p,t) = -D_0 \cdot e^{\frac{-E_a}{k_b \cdot T}} \cdot \overrightarrow{Grad}(C(p,t)) = -D_0 \cdot e^{\frac{-E_a}{k_b \cdot T}} \cdot \frac{\partial C(p,t)}{\partial p} \qquad (2.3.3)$$

The negative symbol indicates that atoms move in the opposite direction of the gradient. Whenever there is a concentration gradient of impurity atoms or vacancies in a solid material, the atoms or vacancies will move through the solid until equilibrium is reached. Therefore this negative sign involves an evolution to equilibrium in the concentrations.

Fick's First Law does not consider the fact that the gradient and local concentration of the impurities in a material decreases with an increase in time, an aspect that's important to diffusion processes. The flux of impurities entering a section of a cylinder with a concentration gradient is different from the flux of impurities leaving the same section. From the law of conservation of matter, the difference between these two fluxes must result in a change in the concentration of impurities within the section (assuming that no impurities are formed or consumed in the section). This conservation of matter is treated by the second Fick's law, stating that the change in impurity concentration over time is equal to the change in local diffusion flux.

$$\frac{\partial C(p,t)}{\partial t} = -\frac{\partial J}{\partial p} \qquad (2.3.4)$$

If the diffusion coefficient is constant, such as when the impurity concentration is low, then combined with the first Fick's law, it becomes [Gli-00]:

$$\frac{\partial C(p,t)}{\partial t} = D \cdot \frac{\partial^2 C(p,t)}{\partial p^2} \qquad (2.3.5)$$

To characterise the radioactive elements leaving the target, the diffusion parameters are not sufficient. Other phenomena have to be taken into account such as the radioactive decay of the nuclide, $\lambda C(p,t)$, created in the target material during this diffusion process and the production rate, $q(p,t)$. Combining equation (2.3.5) with these terms, the Fick's law can be expressed as [Kir-87]:

$$\frac{\partial C(p,t)}{\partial t} - D \cdot \frac{\partial^2 C(p,t)}{\partial p^2} + \lambda \cdot C(p,t) = q(p,t) \qquad (2.3.6)$$

This equation represents the diffusion equation in a particular case: D_0, E_a *and* T are constant. Solving this equation gives the concentration, $C(p,t)$, of the radioactive element studied. The flux leaving the target is deduced from the efficiency of diffusion of the element produced. The equation is fundamentally similar to the previous one but with dependant of the position, *p*, and of the time, *t*.

For an initially homogeneous distribution of nuclei with the diffusion coefficient *D* in an infinite foil of thickness *d* and under the condition that desorption from the surface is fast compared to the mean diffusion time, the delay function is [Kir-92]:

$$p_\mu(t) = \frac{8\mu_0}{\pi^2}\sum_{n=0}^{\infty}\exp\{-\mu_n t\} \qquad (2.3.7)$$

where μ_0 is the delay parameter:

$$\mu_0 = \frac{\pi^2 D}{d^2} \qquad (2.3.8)$$

$$\text{and } \mu_n = \mu_0 \cdot (2n+1)^2 \qquad (2.3.9)$$

Therefore, for a homogeneous distribution of a radio tracer inside of a target matrix a special solution of Fick's law describes the relationship between the fractional release (*F*), the diffusion coefficient (*D*) [Cra-75] and the grain size (of a foil):

$$F_\mu(t) = 1 - \sum_{n=0}^{\infty}\frac{8}{(2n+1)^2\pi^2}\cdot\exp\left\{-\frac{D\cdot(2n+1)^2\cdot\pi^2\cdot t}{d^2}\right\} \qquad (2.3.10)$$

Thus the release efficiency is described as:

$$\xi_{diff}(\lambda) = \frac{8}{\pi^2}\sum_{n=0}^{\infty}\frac{1}{(2n+1)^2 + \lambda/\mu_0} \qquad (2.3.11)$$

where $\lambda = \frac{\ln 2}{t_{1/2}}$.

2.4 Effusion process

As soon as they are released from the target material where they are produced, the radioactive atoms move until they meet a wall where they stand for some time before leaving again up to the next obstacle and then finally are extracted from the ion source (provided that the isotopes have not decayed before). This phenomenon is called effusion.

2.4.1 Conductance of a transfer line

For a simple geometrical approach, the effusion of an atom though a transfer line can be described applying the following assumptions [Rot-82]:

a) the radioactive decay is ignored.
b) the re-diffusion is ignored.
c) the particles do not stick to the wall.
d) all particles diffuse out of the target material instantly following the proton pulse.

Target containers operate under high vacuum ranges (<10^{-4} mbar); for such conditions the mean free path for a particle is much higher than the diameter of the tube they are moving in: $\lambda >> d$. The system is then considered to be under molecular flow: the molecules move freely, without any mutual interference. Therefore the flow of particles leaving the target to reach the ion source can be characterised by the conductance formulas [Gut-49].
The time constant for the release of the particles from a volume, *V*, through the conductance *U* is then defined as:

$$\tau_c = \frac{V}{U} \qquad (2.4.1)$$

The volume of a pipe is given by:

$$V = \pi \cdot \frac{d^2}{4} \cdot l \qquad (2.\ 4.2)$$

where *d* and *l* are the diameter and the length of the tube respectively (figure 2.4-1).

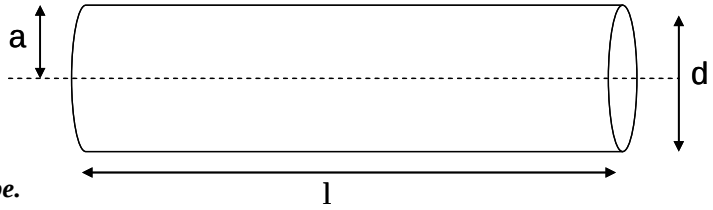

Figure 2.4-1: ***Cylindrical tube.***

The conductance of a cylindrical tube is expressed as [Sak-88]:

$$U = \frac{1}{6} \cdot \sqrt{\frac{2\pi \cdot R_0 T}{M}} \cdot \frac{d^3}{l} \text{ in L.s}^{-1} \qquad (2.\ 4.3)$$

where R_0 is the universal gas constant and is equal to 0.0821 L.atom.mol^{-1}.K^{-1}, *T* the temperature of the gas molecule and *M* the mass of the effusing gas in g.mol^{-1}. Therefore one can deduce that the time constant is:

$$\tau_c = \frac{3\pi . l^2}{2d} \cdot \sqrt{\frac{M}{2\pi \cdot R_0 T}} \qquad (2.\ 4.4)$$

$$\text{Thus } \tau_c \propto \frac{l^2}{d} \cdot \qquad (2.4.4b)$$

Bigger is the diameter, smaller is the effusion time constant along the pipe and longer is the tube, higher is the time constant.

2.4.2 Adsorption phenomena

When a gas or an atom is brought into contact with a solid surface, some of it will be retained by the surface by sorption. Sorption includes two mechanisms: absorption and adsorption [Rot-82]. Sorption reactions generally occur over a short period of time, however if the adsorbed contaminant begins to be incorporated into the structure of the sorbent, a slow occurring reaction, known as absorption, begins to take place. The difference between adsorption and absorption is that adsorption is the attraction between the outer surface of a solid atom and a contaminant, whereas absorption is the uptake of the contaminant into the physical structure of the solid.

The solid is generally referred to as the adsorbent, adsorbed gas as the adsorbate and non-adsorbed gas as the adsorptive. All solid, as well as liquid surfaces present attraction forces normal to the surface, so molecules landing on the surface can be adsorbed. Adsorbed gases under certain conditions of temperature and pressure can be desorbed, and are the main source of gas in vacuum systems. The adsorption-desorption process is controlled by the interaction energy between the adsorbed atoms with the surface atoms. According to this binding energy, the adsorption can be either weak or strong [Rot-82].

Adsorption may occur with gaseous or liquid phase atoms interacting with the solid surface, however the gas phase is typically the most commonly studied phenomenon in surface science as oxides etc. are investigated. When adsorption takes place, the gas atoms are restricted to two-dimensional motion.

Adsorption processes are accompanied by a decrease in entropy and a decrease in free energy: $\Delta G = \Delta H - T\Delta S$ (2. 4.5)

Heats of adsorption can be measured by direct calorimetric methods and isosteric heats of adsorption can be calculated from reversible adsorption isotherms using the Clausius-Clapeyron equation:

$$\left(\frac{\partial \ln p}{\partial T}\right)_v = \frac{-\Delta H_{ads}}{RT^2} \quad (2.\ 4.6)$$

When an atom interacts with a solid surface, it sticks on the surface for a time τ_s given by the Frenkel equation [Loe-34]:

$$\tau_s = \tau_0 \exp(\frac{-\Delta H_{ads}}{k_B T}) \quad (2.\ 4.7)$$

where ΔH_{ads} is the heat of adsorption. When an atom is adsorbed to a surface heat is given off. By thermodynamic convention, exothermic processes are usually designated by a negative sign. When an atom initially contacts a surface, a significant amount of movement occurs along the surface before adsorption takes place. Because the activation energy for surface diffusion is much lower than that for diffusion into the bulk or desorption, atoms may easily diffuse along the surface before bonding to a surface atom. The coverage of a surface is a function of the flux of gas molecules F striking the surface as well as the resident time, where the surface coverage (atoms/cm^2) is given by:

$$S = \tau_s F = \frac{N_A P}{\sqrt{2\pi MRT}} \tau_0 \exp(\frac{-\Delta H_{ads}}{RT}) \qquad (2.\ 4.8)$$

which shows the coverage proportional to pressure *P* and inversely proportional to the square root of molecular mass *M*. As adsorption occurs however, less sites are available for adsorption, or the adsorption of additional layers involves different activation energies. A simple model for adsorption of one monolayer could represent S_0 as a completely covered surface. The available sites are then $S_0 - S$, where a fraction of the total flux $\frac{S}{S_0}F$ would be reflected from occupied sites. The fraction of the surface then left available for adsorption would be $(1-\frac{S}{S_0})F$. Modifying Eq. 2. 4.8, leads to:

$$S = \tau_s F = (1-\frac{S}{S_0})\frac{N_A P}{\sqrt{2\pi MRT}} \tau_0 \exp(\frac{-\Delta H_{ads}}{RT}) \qquad (2.\ 4.9)$$

Making the substitution $\theta = \frac{S}{S_0}$ and $b = \frac{F\tau_s}{S_0 P}$, the degree θ of coverage is given by [Lan-18]:

$$\theta = \frac{bP}{1+bP} \qquad (2.\ 4.10)$$

where the degree of coverage θ is for one monolayer.

When an atom adsorbs onto a surface, it may bond in one of two ways: physical adsorption (physisorption) or chemical adsorption (chemisorption). The former is the weakest for of adsorption and is not a true chemical bond to the surface [Rot-82].

- Physisorption

Physisorption is the adhesion of a thin layer of atoms to a surface without the formation of a chemical bond, either atom-atom or atom-substrate. The binding is mainly due to the interplay of weak attractive forces (predominantly Van der Waals and electrostatic which exist over long ranges) and hard core repulsions. Physisorption is an exothermic process, and its enthalpy can be measured by monitoring the rise in temperature of a sample with known heat capacity during the process of adsorption or desorption of the adsorbate. The enthalpy of physisorption is low (approximately 20 kJ/mol), and this small enthalpy change is insufficient to cause bond breaking. So a physisorbed atom retains its identity, albeit perhaps distorted by the surface. Physisorption is a reversible process, and the adsorption involved can also take place in multilayers.

- Chemisorption

Chemisorption is the adsorption of atoms to a surface through the formation of a chemical bond, as opposed to Van der Waals forces [Rot-82]. The type of interaction is strong; covalent bonds form between adsorbate and surface. The enthalpy of chemisorption (from 50 kJ/mol to 800 kJ/mol) is higher than that of physisorption. The process of chemisorption does not always occur directly from the gaseous state; atoms may be initially adsorbed physically and then, with the provision of a certain minimum energy (activation energy E_A) they may become chemisorbed (activated chemisorption): $E_D = H_C + E_A$ (2. 4.11)
where E_D is the energy of desorption, H_C the heat of chemisorption and E_A the energy of activation.

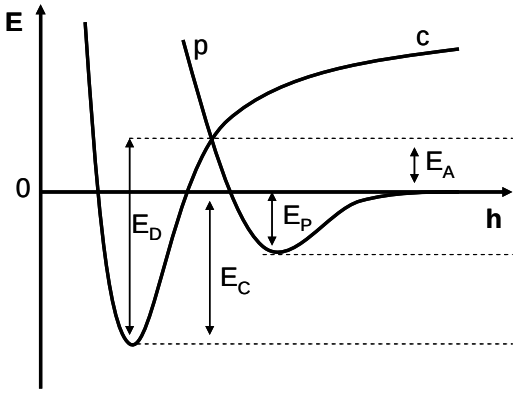

Figure 2.4-2: ***Potential energy, E, for activated chemisorption, with adsorption versus the distance from the surface, h [Rot-82].***

The adsorbate gas atom is first physically adsorbed, which involves approaching the solid surface along a low-energy path. Transition from physical adsorption to chemisorption takes place at the point where curves p and c intersect (figure 2.4-2). The energy at his intersection is equal to the activation energy for chemisorption. The magnitude of the activation energy for chemisorption depends on the shapes of the Physisorption and chemisorption curves.
The extent of gas adsorption onto a solid surface varies according to the temperature at a given pressure (figure 2.4.3).

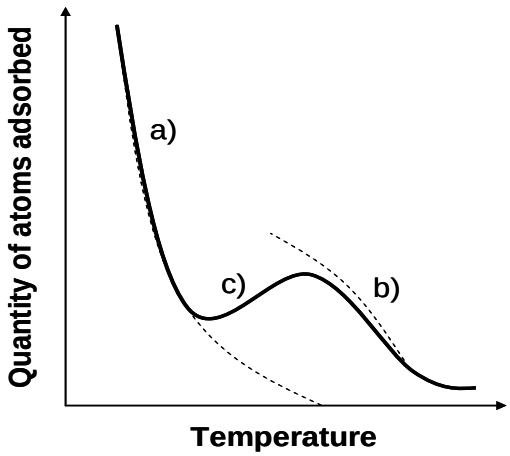

Figure 2.4-3: ***Schematic adsorption isobar showing the transition between physisorption and chemisorption. a) and b) curves represent physisorption and chemisorption equilibrium respectively. c) represents the non-equilibrium curve of the extent of adsorption at temperatures at which the rate of chemisorption is slow.***

2.4.3 Effusion of a radioactive element

As discussed in **Section 2.3.1**, the system is considered to be under molecular flow: the molecules move freely, without any mutual interference.
For an ideal gas in a tube, at low pressure, *P*, and temperature, *T*, the flow rate of the atoms is given by [Pre-58]:

$$\frac{dN}{dt} = -(\frac{2\pi a^3}{3l}) \cdot v \cdot \frac{dn}{dz} = (\frac{2\pi a^3}{3k_B T}) \cdot v \cdot \frac{dP}{dz} \qquad (2.\ 4.12)$$

where *a* and *l* are the radius and the length of the tube respectively; v is the average velocity of the atoms within the tube and $\frac{dn}{dz}$ is the density gradient. *n* is the particle density and k_B is the Boltzmann's constant. Once the effusion process started, the radioactive elements, *N*, produced by the target effuse through the transfer line according to the time, *t*:

$$N(t) = N_0 \exp(-\lambda t) \cdot \exp(\frac{-t}{\tau_{eff}}) \qquad (2.\ 4.13)$$

where N_0 is the number of atoms in the transfer line at time $t=0$. The half life of the nuclei $t_{1/2}$ is equal to $ln(2)/\lambda$.
The average travel distance travelled per particles, L_c, in a tube of length l and radius a can be determined as [Bil-03]:

$$L_c = \frac{6l^2(1+\frac{8a}{3l})}{\pi^2 r} \qquad (2.4.13a)$$

For long tubes, the wall at one end influences on this travel distance and then it can be corrected by:

$$L = L_c(1+\frac{A_E}{A_T}) \qquad (2.4.13b)$$

where $A_E = \pi.r^2$ is the area of the end wall of radius *r*, and $A_T = 2\pi.r.l$ is the surface area of the tube. The time constant of an effusing radioactive atom can be written [Bil-03]:

$$\tau_{eff} \cong g \cdot (n_c \tau_0 \exp(\frac{-\Delta H_{ads}}{k_B T}) + \frac{L}{v}) \qquad (2.\ 4.14)$$

where n_c is the number of collisions of the atoms on the walls of the transfer line. τ_0 (s) is the Debye frequency of the material ($2.4\text{x}10^{-15}$ s for Ta [Kir-92]; $2.3\text{x}10^{-13}$ s for quartz [Sim-07]).

$\nu = \sqrt{\frac{8k_BT}{\pi m}}$ is the average Maxwell velocity for a particle of mass *m* at a temperature *T* (K). and ΔH_{ads} (eV) is the enthalpy of adsorption of the element. *g* is a factor according to the particle emission in a cosine distribution about the normal to the surface during desorption [Bil-03; Kir-92].

The enthalpy of adsorption is much smaller than k_BT for noble gases ($\tau_{eff} \cong g \cdot \frac{L}{\nu}$) and is high for condensable elements. Optimisation of the time constant of the transport of the radioactive elements can be done minimising *L*.

The effusion process is defined by 3 main parameters:

- The mean number of collisions, n_c, from the release of the target to the entrance of the ion source. This parameter depends on the geometry of the target-ion source unit.
- The sticking time, τ_s (s), corresponding to the time an atom stays on the solid surface before leaving. τ_s is related to the enthalpy of adsorption by the equation 2. 4.7.
- And also the average flight time, τ_{fl}, of the particle between two sticking points on the wall. It's defined by the mean distance, d_{fl}, and by the thermal velocity in m.s^{-1} of the effusing element.

$$\tau_{fl} = d_{fl} \cdot \sqrt{\frac{m}{3k_BT}} \qquad (2.\ 4.15)$$

where *m* (kg) represents the mass of the effusing element, *T* (K) is the temperature of the system and k_B is the Boltzmann constant (J/K).
Therefore, rearranging equation 2.3.14, the average time of effusion due to collisions can be expressed [Kir-92]:

$$\tau_{co} = n_c \cdot (\tau_{fl} + \tau_s) = \frac{1}{\nu} \qquad (2.\ 4.16)$$

where *v* represents the average time constant of the effusion in s^{-1}. Combining (2. 4.15) and (2. 4.16) equations, leads to:

$$\tau_{co} = n_c \cdot (\tau_{fl} + \tau_s) \cong n_c \cdot \tau_{fl} = n_c \cdot d_{fl} \cdot \sqrt{\frac{m}{3k_BT}} \cong \tau_c \qquad (2.\ 4.17)$$

$$\text{Thus } \overline{d_{fly}} \propto \frac{L^2}{d} \qquad (2.\ 4.18)$$

According to Kirchner [Kir-92] the probability an atom has effused within a thin target system between *t* and *t+dt* can be expressed as:

$$p_\nu(t) \cdot dt = \nu \cdot e^{-\nu t} \cdot dt \qquad (2.\ 4.19)$$

The fractional release is given by [Kir-92]:

$$F_\nu(t) = \int_{t'=0}^{\infty} p(t')dt' = 1 - e^{-\nu t} \qquad (2.\ 4.20)$$

The effusion efficiency is therefore calculated for a nuclide of half life $t_{1/2}$:

$$\xi_{eff}(t_{1/2}) = \int_{t=0}^{\infty} \nu \cdot e^{-\nu t} \cdot e^{-\lambda t} dt = \frac{\nu}{\nu + \lambda} \qquad (2.\ 4.21)$$

The efficiency of effusion depends on the half life of the isotopes and on the geometry of the system.

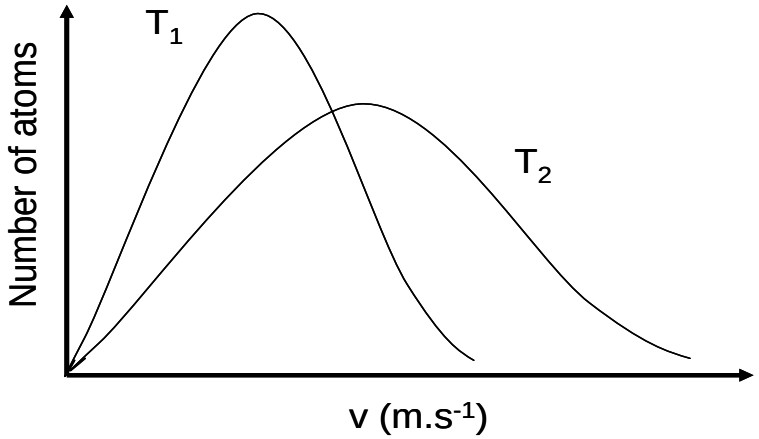

Figure 2.4-4: ***Maxwell-Boltzmann distribution of the velocity of the atoms according to different temperatures T_1 and T_2 where $T_2>T_1$.***

2.5 Models of the release function

Physical model based on effusion-diffusion process

As seen in **Section 2.3**, the delay time is affected by physical characteristics of the target such as effusion and diffusion. Combining these two different functions (equation (2.3.7) and (2.4.19)) as a convolution in time by assuming that particles effuse after being released from the target material and never diffuse back after, one can express the following equation [Kir-92]:

$$p(t) = p_\mu \otimes p_\nu(t) = \int_0^t p_\mu(\tau) \cdot p_\nu(t-\tau) \cdot d\tau \qquad (2.5.1)$$

The diffusion takes place in the time interval [0, τ] and effusion in [τ, t]; this leads to:

$$p(t) = \frac{8\mu_0 \nu}{\pi^2} \sum_{n=0}^{\infty} \frac{e^{-\nu t} \cdot e^{-\mu_n t}}{\mu_n - \nu} = \frac{8\mu_0 \nu}{\pi^2} \left\{ \sum_{n=0}^{\infty} t \cdot e^{-\nu t} + \frac{e^{-\nu t} \cdot e^{-\mu_n t}}{\mu_n - \nu} \right\} \qquad (2.5.2)$$

in the case of that $\mu_0 = \nu$.

Simplified analytical model

Most of release processes start with a sharp rise, followed by a steep fall and end with a tail (figure 2.5-1). This function can be mathematically defined using 3 time-constant parameters (λ_R, λ_F, λ_S) and one weighing parameter α [Let-97].

$$P(t, \lambda_R, \lambda_F, \lambda_S, \alpha) = \frac{1}{Norm} \cdot (1 - e^{-\lambda_R t}) \cdot \left[\alpha \cdot e^{-\lambda_F t} + (1-\alpha) \cdot e^{-\lambda_S t} \right] \qquad (2.5.3)$$

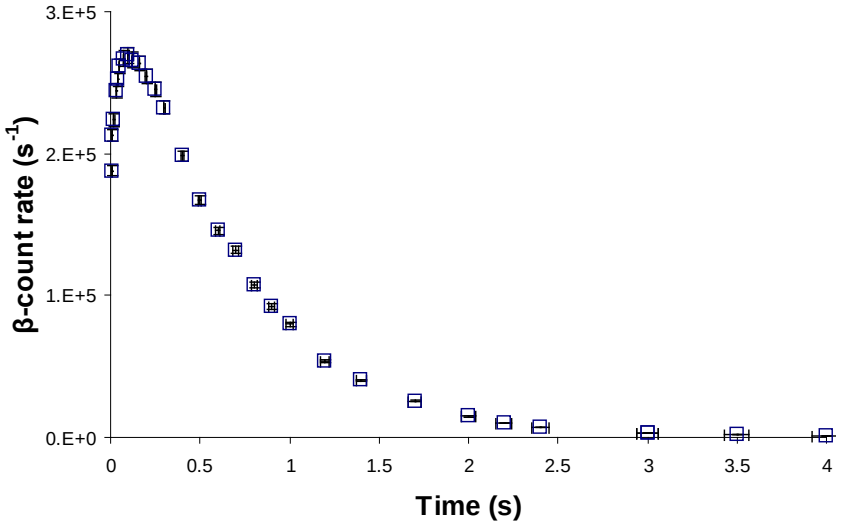

Figure 2.5-1: ***Typical measurement of the release of ^{20}Na from a uranium carbide target (collection time of 50ms).***

The rise time is assimilated to the speed of effusion from the target to the ion source via the transfer line whereas effusion and diffusion within the target material influences the fall of the function. The fast fraction α (0< α <1) determines the relative weight of the last and slow fall components.

Element	Target		Ionisation	Release			
	δ (g/cm^2)	T (°C)	efficiency (%)	α	t_r (ms)	t_f (ms)	t_s (ms)
He	*52*	*2100*	*0.14*	*0.38*	*10*	*20*	*81*
Ne	*52*	*2100*	*0.36*	*0.99*	*18*	*150*	*2100*
Ar	*52*	*2100*	*2.0*	*0.96*	*38*	*300*	*2030*
Kr	*52*	*2100*	*4.3*	*0.91*	*73*	*530*	*3190*
Xe	*52*	*2200*	*11*	*0.96*	*107*	*950*	*5290*

Table 2.5-1*: Typical online values [Ber-03]*

Table 2:5-1 represents typical on-line parameters for the release of He, Ne, Ar, Kr and Xe elements from an ISOLDE uranium carbide/ graphite target. The diffusion and effusion processes slow down as the mass and size of the atom increases [Ber-03]

A Monte-Carlo approach of the diffusion-effusion processes

In order to simulate the diffusion and effusion processes, Monte-Carlo codes such as Geant4 and RIBO [San-05] are used. The Monte Carlo simulation code, RIBO (Radioactive Ion Beam Optimization), simulates and tracks nuclei as function of the geometry and materials being used. It uses database containing the diffusion parameter and adsorption enthalpy to be used for the choice of material and temperature in the target-ion source unit for the production of a radioactive ion beam. Due to the nature of Monte Carlo simulations, in which particles are thrown one by one, particle interactions (this affects recombination probability, and consequently, ionisation probability) are accounted for via the extraction efficiency constant; considering that all the atoms that have been ionised reach the end surface without recombining.

Chapter 3

Purification of a RIB by Alkali Suppression in a Quartz Line Target

At ISOLDE, the principle of isothermal chromatography is applied to design a selective transfer line in an ISOL target and ion source. For the production of pure noble gases Radioactive Ion Beams (RIBs) the less volatile elements are condensed in the transfer line that links the target and the ion source [Sun-92]. The selective ionisation schemes such as that provided by Resonant Ionization Laser Ion Source [Fed-06] (RILIS) suffers from isobaric contamination which occurs by surface ionisation of low ionisation potential elements in the RILIS high temperature cavity. The development of prototypes with a quartz insert in the transfer line and precise temperature control is presented in this chapter.

For Zn ionisation with the RILIS, the most serious background will be Rb (figure 3.0-1) and to less degree also Ga and Sr (easily surface ionised due to their low ionisation potential). Same as for Cd ionisation, the most serious background will be Cs and In.

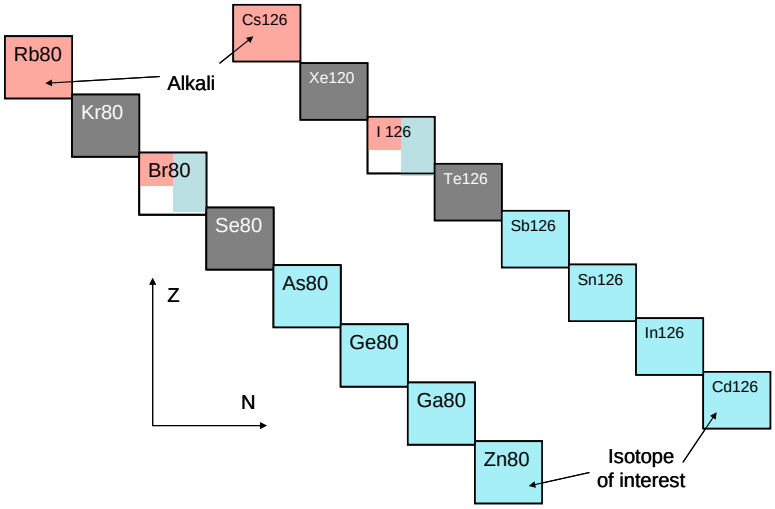

Figure 3.0-1*: Example of two isotopes of interest ^{80}Zn, ^{126}Cd, and their isobaric contaminations.*

3.1 Development of a quartz (SiO_2) transfer line

3.1.1 Choice of the trapping material and geometry of the line

As shown by Kratz et al. [Kra-86], quartz has the properties of delaying alkalis (^{130}Cs) and thus reducing by decay the alkali contamination coming out the transfer line. Also, recent series of gas thermochromatography experiments showed that quartz glass is a promising surface that has many open cavities into which alkali atoms can easily diffuse and get trapped such as Rb and Cs. [Kos-07]. Therefore it has been decided to take Si_2O element for the purification of RIBs of Zn and Cd RIBs.
RIBO [San-05] code allowed the estimation of the quartz dimensions to be used according to the number of collisions. Two cases have been investigated and are shown in figure 3.1-1. Calculations of the number of collisions were done in surface 'q' (l_q and r_q) for the geometry (a) for different radii and lengths. Simulations have been realized using ^{131}Cd isotope. UC_2-C has been taken as target material inside a matrix of graphite. The second case (b) represents the geometry of a standard ISOLDE target with a horizontal chimney of 120mm long.

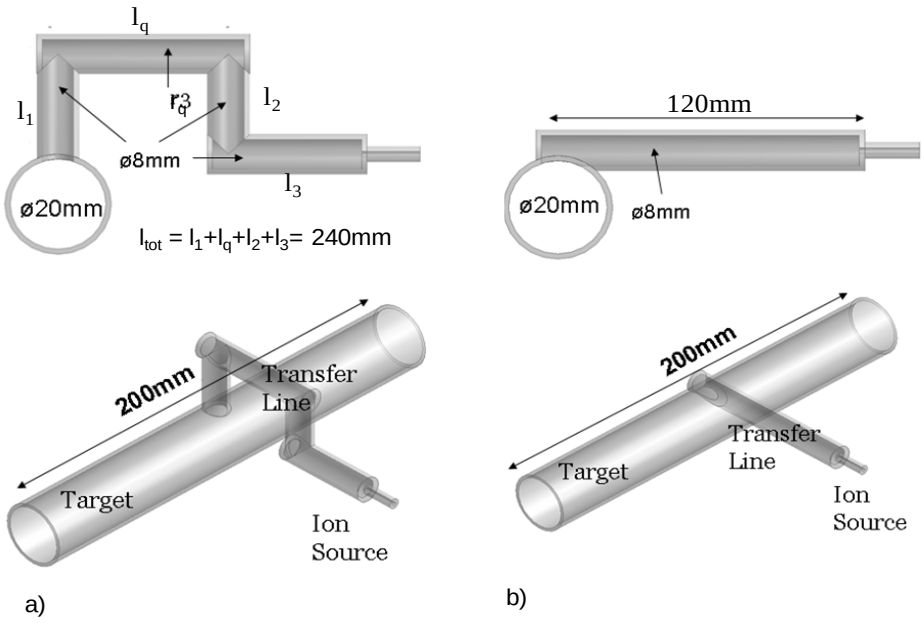

Figure 3.1-1*: Geometry of the quartz line (a) and of a standard transfer line (b), investigated with RIBO*

An element produced in the target hits 660 times the wall of a standard transfer line (total length: *120mm*) before it reaches the ion source (RIBO simulations) while for the quartz line configuration (figure 3.1-1, case a) collisions are increased up to 1260 (total length: *240mm*, l_q *=50mm*, r_q *=3mm*). The number of collisions of the elements inside the tube of quartz of length l_q increases when the radius of this tube is decreased; for a fixed length (l_q*= 60mm*), the number of collisions is decreased by factor 3 when the radius of the tube is doubled from *1.5mm* to *3mm* (figure 3.1-2).

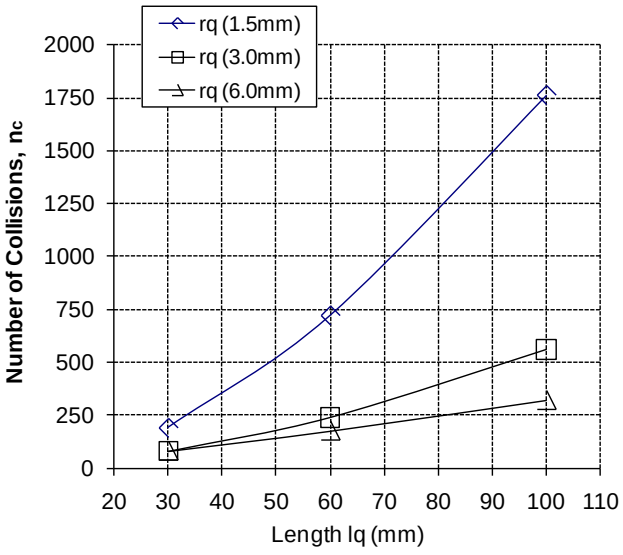

Figure 3.1-2*: Plot of the number of collisions for an isotope ^{131}Cd travelling into a tube of length l_q and of radius r_q of the case (a).*

The number of collisions of the isotopes with the wall of the quartz must be optimised both to efficiently delay the alkalis within the transfer line and to allow the isotopes of interests having a short half life to be released and measured.
Figure 3.1-3 shows the comparison of the ^{131}Cd releases from the two different geometries.

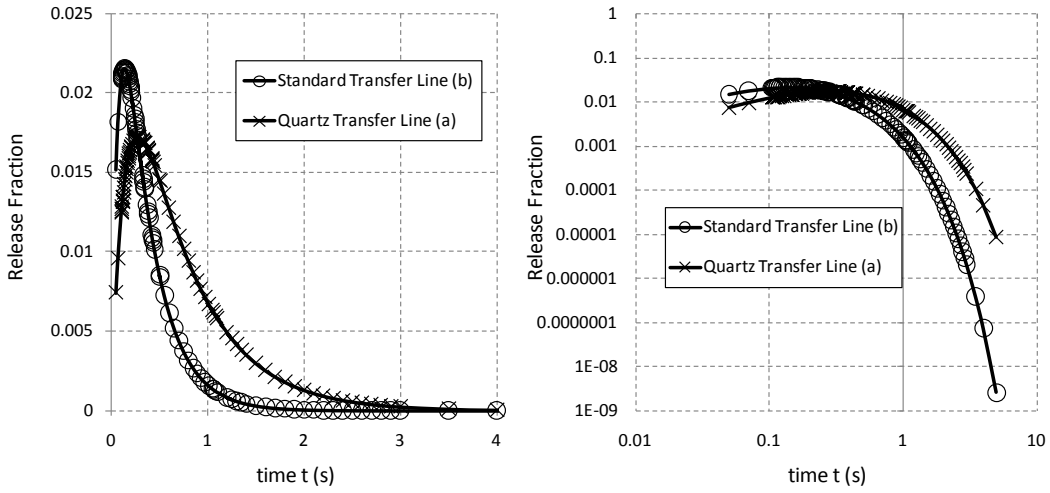

Figure 3.1-3*: Comparison of release of ^{131} Cd through the transfer line of case a) with a total length l_{tot}=240mm (l_q=50mm) and case b) with a total length of 120mm (Temperature taken for the simulations: 1800K)*

The isotopes effuse faster within the standard transfer line (case b) than within the quartz line (case a) (figure 3.1-3). The path the isotopes have to travel between the target and the ion source is doubled for the quartz configuration; nevertheless this later case is preferred due to heat transfer issues (see Section 3.1.2).
Following the analyses of the RIBO simulations, it was decided to use a piece of quartz having a cylindrical shape of *50 mm* length and *6 mm* diameter. The average number of collisions of an atom travelling through a tube for such dimensions *is* $n_c = 220 \pm 20$.

3.1.2 Thermal characteristics of a tube of SiO_2 into a Ta transfer line

An ISOLDE UC_2-C target operated above *2000˚C* is used to produce a wide range of reaction products. To avoid the melting of the quartz by a direct view with UC_2-C, the transfer line has been designed with an estimation of the heat flow (figure 3.1-4). To efficiently trap alkalis, the transfer line must operate within a certain range of temperatures; therefore 2 prototypes were designed with a controlled transfer line temperature: from *700ºC* to *1100ºC* (<*warm line*>); from *300ºC* to *800ºC* (<*cold line*>).

<*Warm line*>, operating from 700ºC to 1100ºC

To control the temperature at the quartz location, an external oven was positioned around the transfer line (figure 3.1-4) and a radiator, for heat dissipation, was installed at the exit of the container.

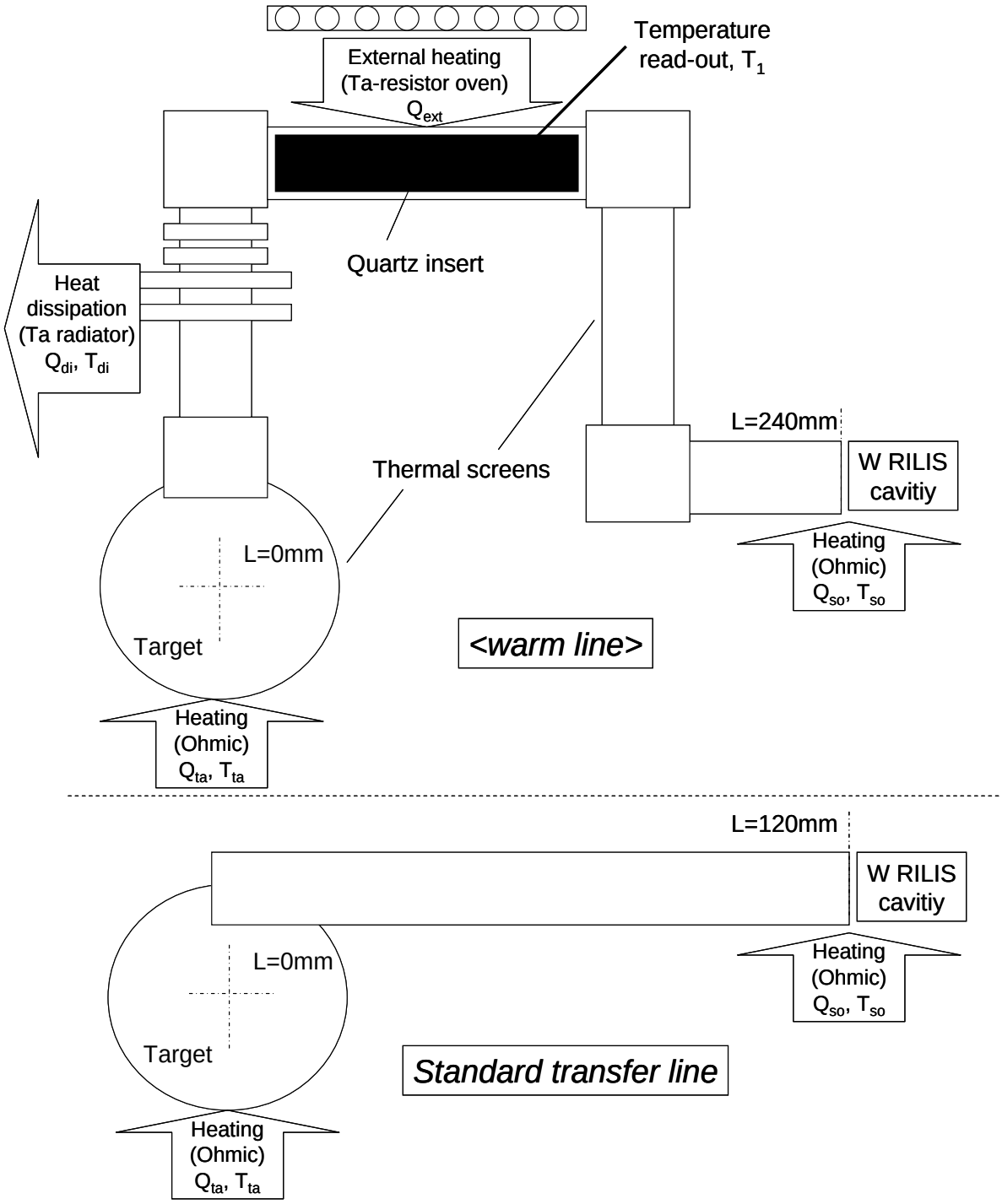

Figure 3.1-4: ***Schematic layouts of a standard transfer line and the <warm line> displaying heat sources and sinks used for the simulation of the quartz operating temperature (T_1). L is the coordinate along the line.***

Calculations of the heat transfer have been carried out using thermal conductivity and radiation equations (3.1.0) and (3.1.1).
Equation (3.1.0) was used to calculate the heat transfer by conductivity over the target/transfer line system [Inc-02]:

$$q_x(L) = k.A_1(L).\frac{dT}{dL} \qquad (3.1.0)$$

where q_x is the heat flow rate (W), A_1 represents the section through which the heat is conducted (m^2), dT/dL is the temperature gradient along the line (K/m) and k, the thermal conductivity ($W/m.K$).
Thermal radiation is taken into account through the following equation [Inc-02]:

$$q_{rad}(L) = A_2(L).\varepsilon.\sigma.(T_S^4(L) - T_0^4) \quad (3.1.1)$$

q_{rad} is the radiated heat flow (W). A_2 is the area (m^2). ε is the emissivity. σ is the Stefan-Boltzmann constant ($\sigma = 5.67 \text{ X } 10^{-8}\ W/m^2.K^4$). T_s is the temperature of the surface. T_0 is the temperature of the surrounding surface. The target and ion source temperature are at $T_1=2000^\circ C$ and $T_4=2100^\circ C$ respectively. The geometry of the transfer line was drafted varying the oven and radiator parameters.

3D Simulations have also been done using ANSYS [Ans-00] to determine the quartz insert temperature. Thermal radiation and conductivity were taken into account in these simulations.

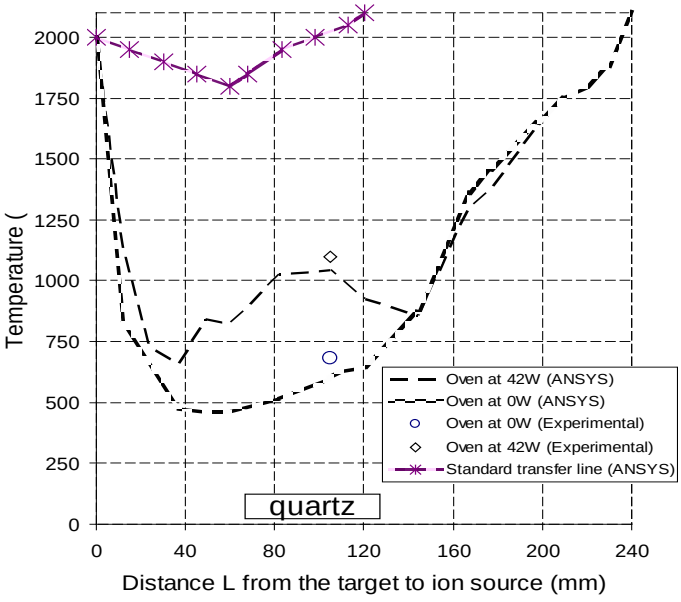

Figure 3.1-5*: Comparison of ANSYS Workbench simulations and experimental temperatures of the quartz transfer line <warm line> with oven switched off (Q_{ext}= 0 W) and oven at Q_{ext}= 42 W.*

The minimum temperature reached in this configuration at the quartz location where a thermocouple readout has been positioned was predicted to be *600˚C* (figure 3.1-5).

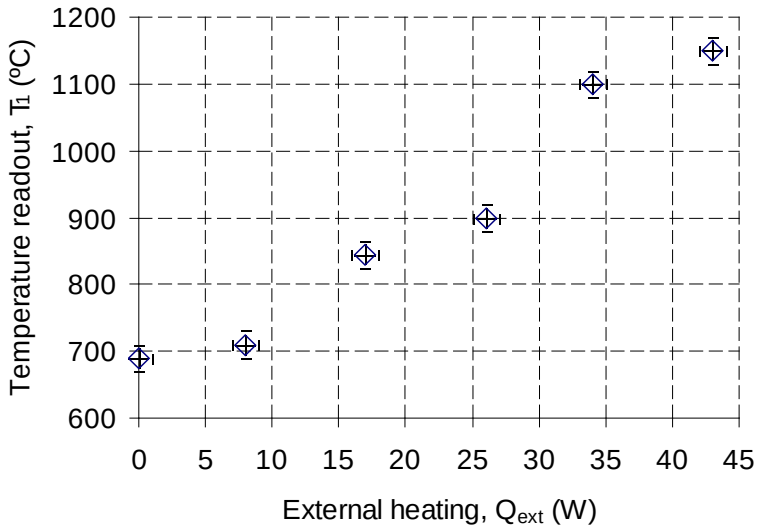

Figure 3.1-6*: Temperature of the <warm line> at different heating powers.*

The produced unit was then calibrated as a function of the oven power (figure 3.1-6). The thermocouple measured a temperature of *680˚C* when no current was applied on the oven in good agreement with the simulations. The external oven allows the setting of the temperature T_1 of the transfer line from *680˚C* to *1150˚C* corresponding to *42 W* dissipated in the oven. Figure 3.1-7 shows a picture of the <warm line> when being assembled.

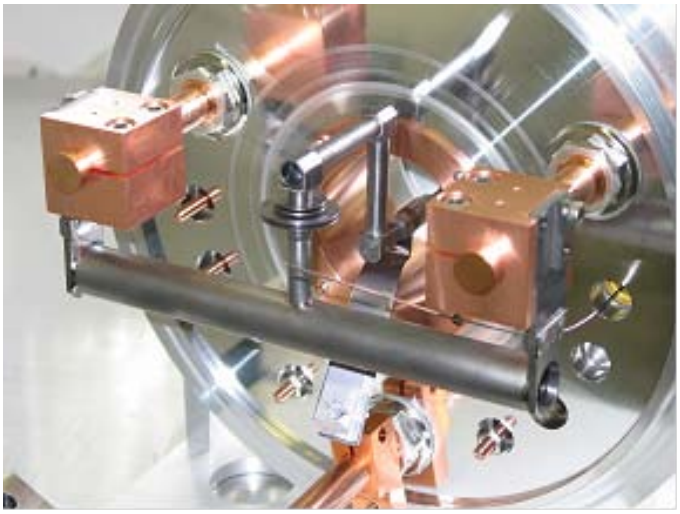

Figure 3.1-7*: Quartz transfer line, <warm line> linking to the Ta oven, the ISOLDE target and the ion source.*

<u><*Cold line*>, operating from 300ºC to 800ºC</u>

This second version of the transfer line named <*cold line*>, was designed with the aim of being colder than the <*warm line*>, with a temperature range from *300˚C* to *800˚C.* As for the <*warm line*>, an external oven was positioned around the transfer line (figure 3.1-8) and a radiator, for heat dissipation, was installed at the exit of the container. A water cooling block allowed the transfer line to reach a minimal temperature of T_1= *308ºC* (figure 3.1-9).

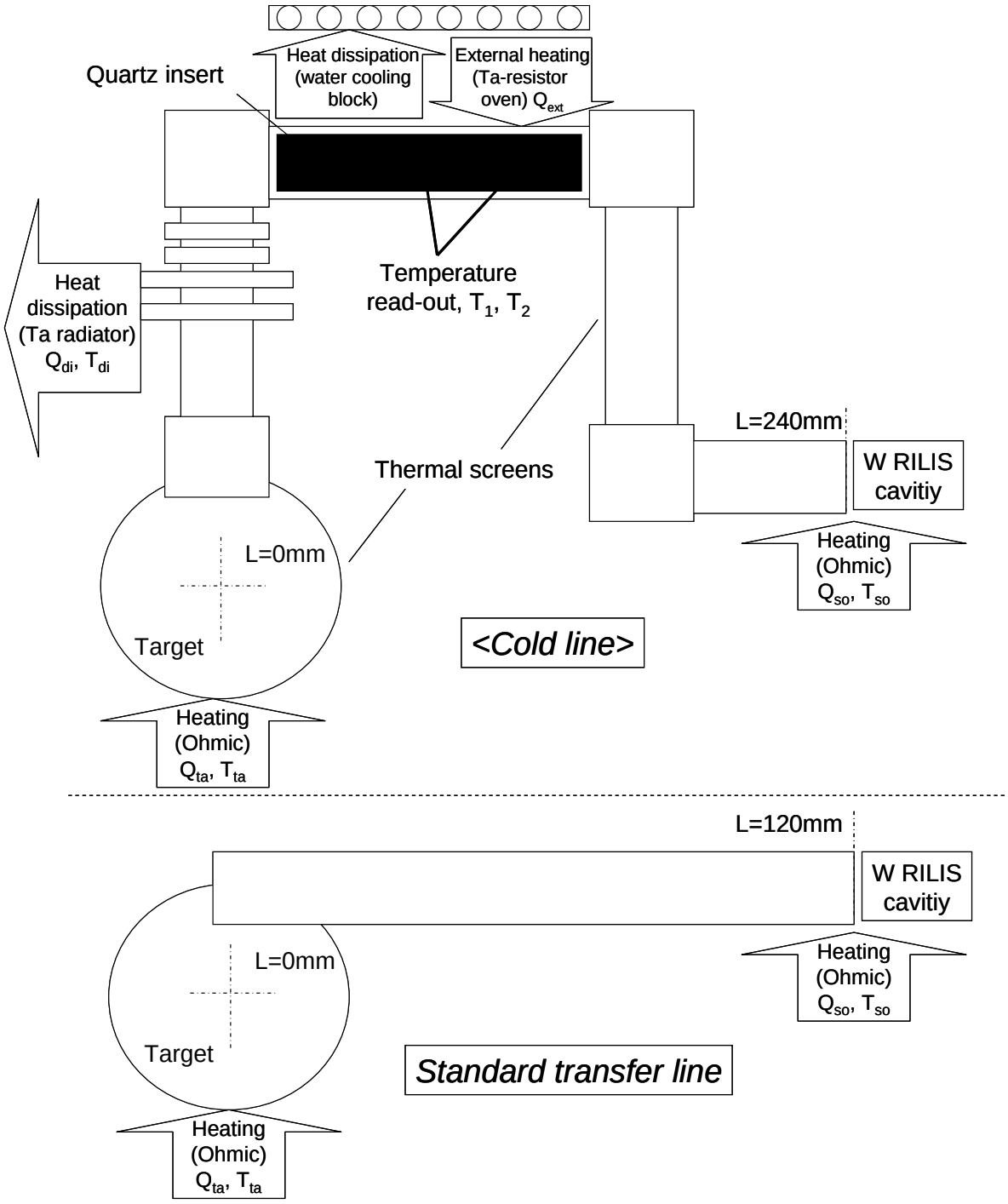

Figure 3.1-8: ***Schematic layouts of a standard transfer line and the <cold line> displaying heat sources and sinks used for the simulation of the quartz operating temperature. L is the coordinate along the line.***

A water cooling block allowed the transfer line to reach a minimal temperature of T_1= *308ºC* (figure 3.1-9). Calculations of the heat transfer have been carried out solving the local heat transfer equations; thermal conductivity and radiation equations along the distance L (equation 3.1.0 and 3.1.1).
The target and ion source temperature are at *2000˚C* and *2100˚C* respectively. The transfer line was designed varying the oven and radiator geometry. Temperature profiles of the <*cold line*> of the quartz line was shown to be different from the <*warm line*>: due to the contact of cooling system on the line, the difference of temperature between the middle of the quartz tube and the extremities increases with an increasing power of the oven giving a triangular temperature profile (not seen for the <*warm line*>). The minimum temperatures predicted at the end and at the middle of the quartz where thermocouples have been positioned are T_1= *380˚C ± 5˚C* and T_2= *420˚C ± 5˚C* (figure 3.1-9, 3.1-10).

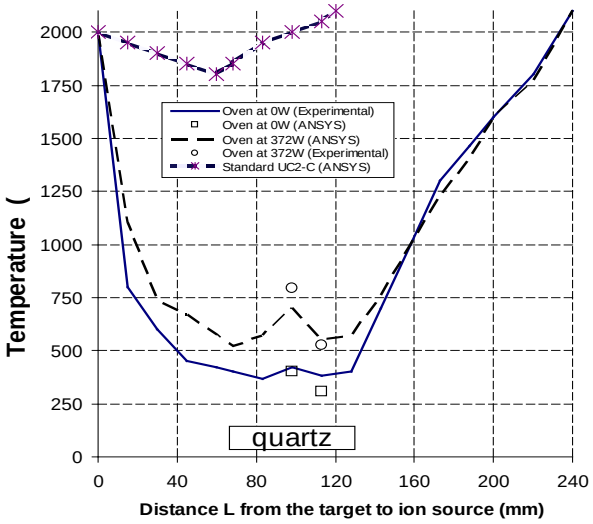

Fig.3.1-9

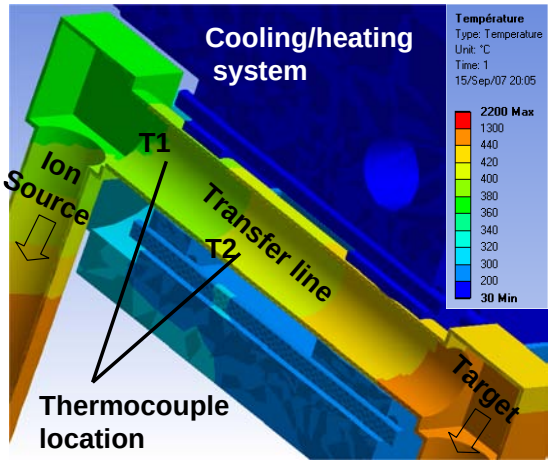

Fig.3.1-10

Figure 3.1-9*: Comparison of ANSYS simulations and experimental temperatures of the <cold line> with oven switched off (Q= 0 W) and oven at Q= 372 W.*
Figure 3.1-10*: Temperature profile through the <cold line> simulated with ANSYS. T_1 and T_2 are the thermocouple locations at the end (<source>) and at the middle of the quartz respectively.*

T_1 and T_2 were recorded at *308˚C ± 5˚C* and *394˚C ± 5˚C* respectively when no current was applied on the oven. For *372W* dissipated in the oven, the highest temperatures reached T_1= *524˚C ± 5˚C* and T_2= *792˚C ± 5˚C* (figure 3.1-11). The differences between the temperatures measured online and the ones measured offline came from the fact that the water cooling was not flowing at the same velocity into the system. A version similar to the <*cold line*> was designed with the aim of being able to regulate further the cooling effect at the quartz location and therefore operate within a broader range of temperatures. This version is named <*cold line 2*> and is shown in figures 3.1-12 and 3.1-13.

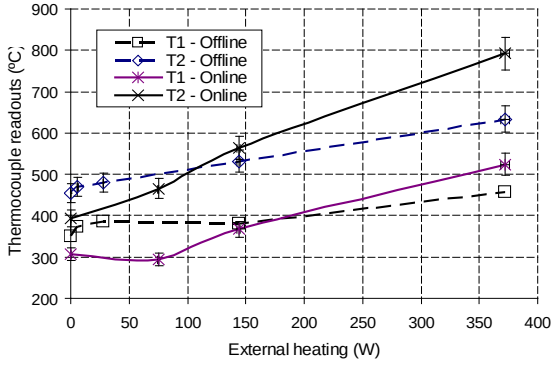

Figure 3.1-11*: Temperature of the cold line at different heating powers, Q_{ext}.*

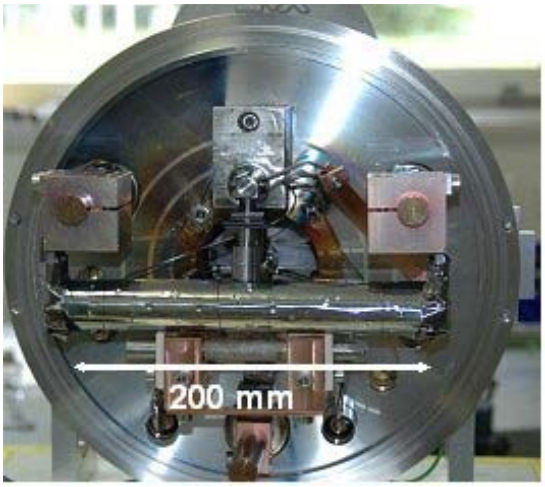

Fig. 3.1-12

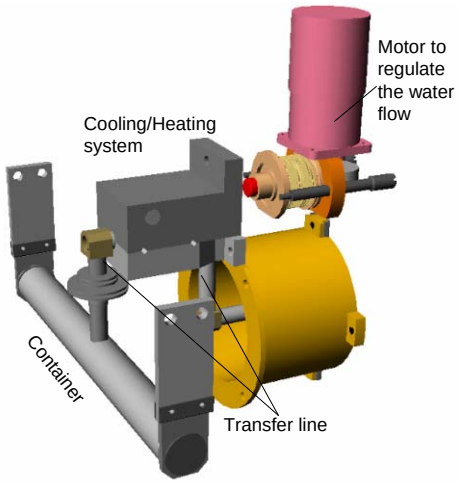

Fig.3.1-13

Figure 3.1-12*: Quartz transfer line, <cold line> linking to the temperature controlled system, the ISOLDE target and the ion source.*
Figure 3.1-13*: Schematic layout of the <cold line 2> linked to a motor to regulate the water flow.*

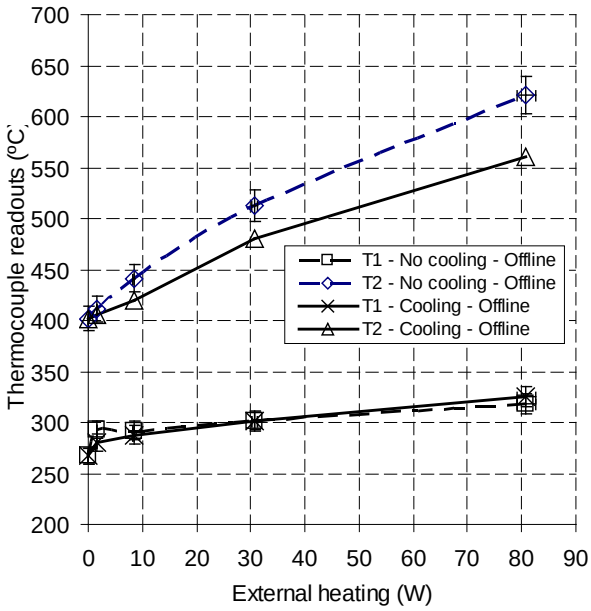

Figure 3.1-14*: Temperature of the <cold line 2> for different heating powers, Q_{ext} (Off-line).*

The motor was able to regulate the temperature by *50˚C* at the middle of the quartz line (T_2) when a maximum power of *82 W* was applied to the oven (figure 3.1-14). No similar effect was noticed on the source part of the quartz (T_1); this is due to the part of the cooling system which is in contact with the cooled face of the main part of the confinement box.

3.2 Suppression of the alkali contamination by a temperature controlled quartz line

3.2.1 Trapping of the $^{79, 80, 82m}$Rb and $^{126, 142}$Cs contaminants

Rubidium contamination

Rubidium has been the first yield of alkali contaminant studied. The measured ^{80}Rb *($t_{1/2}$= 33.4s)* element for a temperature of *680˚C* (<*warm line*>) is *2.2x10^{4} ions/μC* whereas for a standard UC_2-C ISOLDE target the yield is *1.79x10^{8} ions/μC* thus the ^{80}Rb has been suppressed by 4 orders of magnitude. ^{80}Rb yields as a function of the quartz temperature is shown in figure 3.2-1.

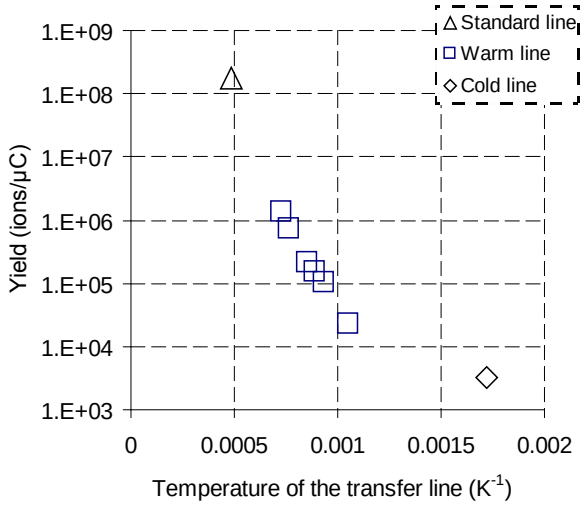

Figure 3.2-1*: Yields of ^{80}Rb ($t_{1/2}$= 33.4 s) according to the temperatures at the quartz location, t_1, for the <warm line>, <cold line> and a standard line.*

According to the temperatures applied by the oven of the transfer line, the yields measured with the <*warm line*>, follow a specific trend. A decrease of the temperature of the quartz clearly induces a decrease in the yield (figure 3.2-1).

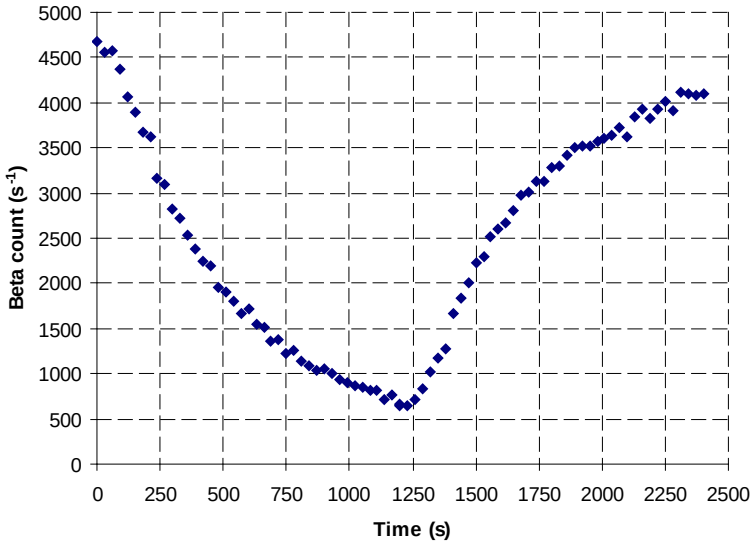

Figure 3.2-2*: Depletion and repopulation of ^{79}Rb ($t_{1/2}$=22.9 min) onto the quartz.*

Figure 3.2-2 shows intensity of the ^{79}Rb *($t_{1/2}$= 22.9 min)*. The proton beam has been stopped at time *0 second* up to *1250 seconds* to measure the depletion of the piece of quartz by the isotope. At the time *1250 seconds*, the proton beam has been sent again onto the target (repopulation) which induces an increase of the beta counts.

Cesium contamination

The quartz lines suppressed ^{142}Cs *($t_{1/2}$= 1.70 s)* alkali contaminants by 3 orders of magnitude when compared to a standard transfer line (figure 3.2-3).

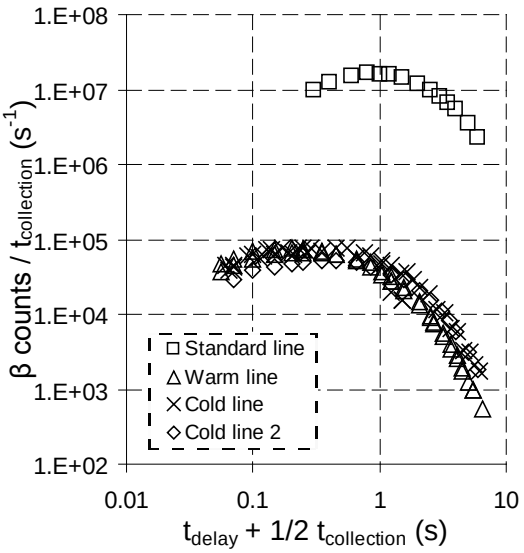

Figure 3.2-3*: ^{142}Cs ($t_{1/2}$= 1.70 s) release from ISOLDE UCx target compared with the different quartz lines. Release measured when no heat was applied from the external oven of the transfer lines (Q= 0 W).*

The suppression factor for ^{142}Cs *($t_{1/2}$= 1.70 s)* was insensitive to the temperatures of the <*warm line*> and the <*cold line*>. The <*cold line 2*> seemed to show a different release curves when compared to the two previous prototypes (figure 3.2-4).

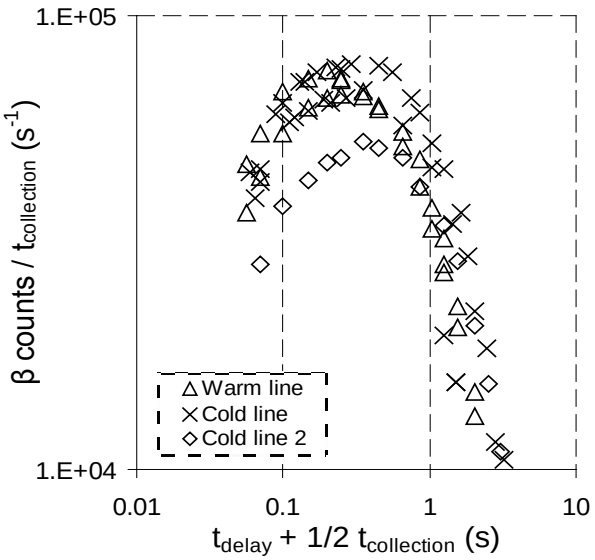

Figure 3.2-4*: ^{142}Cs ($t_{1/2}$= 1.70 s) release from the 3 different quartz lines.*

A much stronger effect was observed on the suppression of ^{126}Cs ($t_{1/2}$= *98.4 s*) as illustrated at different temperatures on figure 3.2-5. The measured ^{126}Cs contaminant for a temperature of T_1= *308˚C* is *2.3x10^3 ions/µC* whereas for the highest temperature the yield is *4.6x10^5 ions/µC*. Thus between these two temperatures ^{126}Cs has been suppressed by *200*.

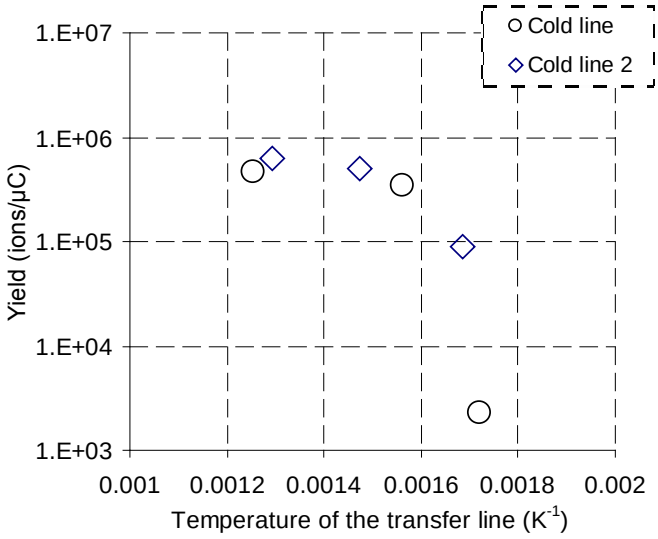

Figure 3.2-5*: Yields of ^{126}Cs ($t_{1/2}$= 98.4 s) according to the temperatures T_1, at the quartz location for the <cold line> and <cold line 2>.*

3.2.2 Trapping of other alkalis: ^{8}Li, ^{46}K and ^{25}Na

^{8}Li *($t_{1/2}$= 0.84 s)*, ^{46}K *($t_{1/2}$= 1.92 min)* and ^{25}Na *($t_{1/2}$= 59.1 s*) was suppressed from 2 to 3 orders of magnitude when compared to a standard line (figure 3.2-6). All three prototypes did not show any difference in the release of the elements according to the operating temperatures of the quartz.

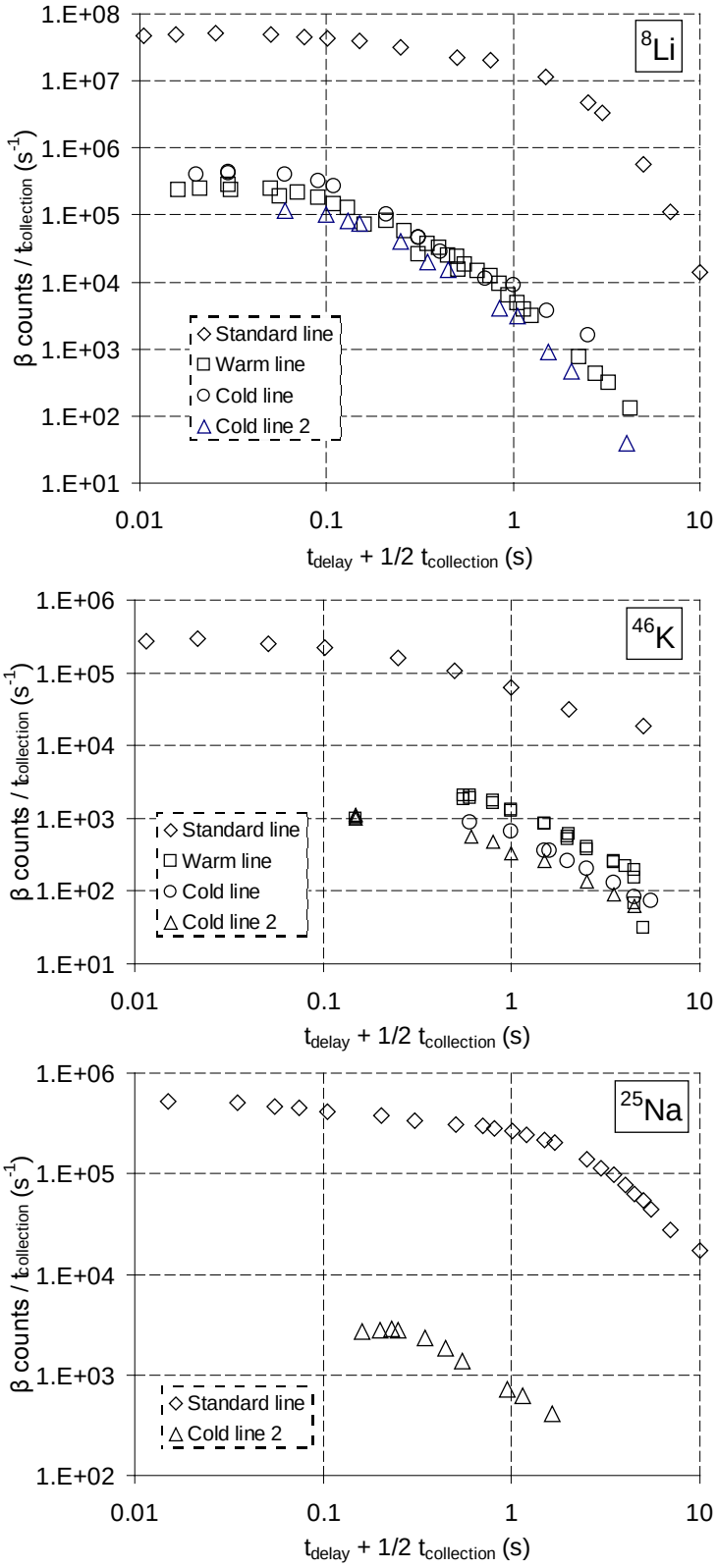

Figure 3.2-6*: Release curves of ^{8}Li ($t_{1/2}$= 0.84 s), ^{46}K ($t_{1/2}$= 1.92 min) and ^{25}Na ($t_{1/2}$= 59.1 s) from ISOLDE UCx target compared with the different quartz lines. Releases measured when no heat was applied from the external oven of the transfer lines (Q_{ext}= 0 W)*

Isotope	$t_{1/2}$ (s)	Transfer line version	Ext. heating, Q_{ext} (W)	Temperature of the quartz at T_1 (°C)	Yield (ion/µC)	Yield of a standard transfer line (ion/µC)**	Suppression factor
^{8}Li	0.84	Warm line	0	680	$\mathbf{3.3x10^{4}}$	$3.9x10^{7}$	$\mathbf{1x10^{2}}$
^{25}Na	59.1	Cold line 2	44	348	$\mathbf{5.4x10^{4}}$	$2.7x10^{8}$	$\mathbf{5x10^{3}}$
^{46}K	115.2	Cold line	144	360	$\mathbf{5.1x10^{5}}$	$5.4x10^{7}$	$\mathbf{1x10^{2}}$
^{80}Rb	34	Cold line	0	308	$\mathbf{3.0x10^{3}}$	$1.8x10^{8}$	$\mathbf{6x10^{4}}$
^{82m}Rb	76.2	Cold line	0	308	$\mathbf{3.2x10^{4}}$	$7.2x10^{7}$	$\mathbf{2x10^{3}}$
^{126}Cs	98.4	Cold line	0	308	$\mathbf{2.3x10^{3}}$	$3.4x10^{7}$	$\mathbf{1x10^{4}}$
^{126}Cs	98.4	Cold line	144	360	$\mathbf{4.6x10^{5}}$	$3.4x10^{7}$	$\mathbf{7x10}$
^{142}Cs	1.70	Cold line	0	308	$\mathbf{2.6x10^{5}}$	$1.6x10^{8}$	$\mathbf{6x10^{2}}$

Table 3.2-1*: Yields of ^{8}Li, ^{25}Na, ^{46}K, $^{80,82m}Rb$ and $^{126,142}Cs$ isotopes measured with the quartz line and their suppression factors. **the yield of a same isotope fluctuates from a standard unit to another one. Some 'uncontrolled' parameters influence the yields of an isotope at a different level: low (statistic, proton beam parameters), medium (target material preparation, ion source efficiency) or high (half life of the isotope: a short half life will tend to dramatically increase the error bar of the fitting parameters – rise time and fast and slow fall time). To be able to deduce physical parameters from the suppression factors, additional beam time is required; it was more specially done for ^{80}Rb and ^{142}Cs, to deduce the enthalpy of absorption from $f_{th}(\lambda,T)$ (Section 3.5).*

Within both of the prototypes, the highest suppression factor reached was for the ^{80}Rb *($t_{1/2}$= 33.4 s)* which was suppressed by a factor 60 000 (table 3.2-1).

3.3 Production of ^{122,126}Cd and ^{75}Zn

Elements of interest were ionised by RILIS method (Resonance Ionisation Laser Ion Source) which is based on the selective excitation of atomic transitions by tunable laser radiation (see **Section 1.3.3**). Cadmium and Zinc were the two main elements of interest studied with the quartz line. Cadmium is an element which is ionised by laser, however, it suffers from isobaric contamination such as Cesium (alkali) and Indium which are also produced in high quantities and released from the target.
The release of the ^{122}Cd ($t_{1/2}$= *5.2 s*) has been measured with the <*warm line*> (figure 3.3-1) when no heating was applied to the external oven (Q_{ext}= *0 W*).

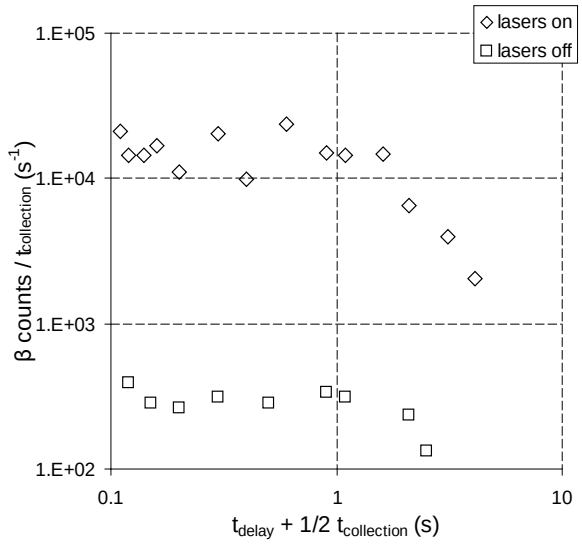

Figure 3.3-1*: Release curves of ^{122}Cd ($t_{1/2}$= 5.2 s) (lasers on) and of ^{122}In ($t_{1/2}$= 1.5 s) (lasers off), measured with the <warm line> (no heat was applied from the external oven of the transfer line, Q_{ext}= 0 W)*

When no laser was applied to ionise the ^{122}Cd *($t_{1/2}$= 5.2 s)*, ^{122}In ($t_{1/2}$= 1.5 s) was the only isotope measured on the tapestation (factor 50 times less). This means that no ^{122}Cs *($t_{1/2}$= 21.2s)* is release from the ion source. Yield of the ^{122}Cd was calculated to be $6.34x10^{4}$

ions/μC which is close to typical ISOLDE yields. On the other hand, ^{126}Cd *($t_{1/2}$= 0.52 s)* showed a yield of *1.38x10^5 ions/μC* (typical yields being around *9x10^5 ions/μC*) and was only contaminated by ^{126}Cs (*$t_{1/2}$= 1.64 min*) with a yield of *2.59x10^4 ions/μC* which gave a ratio *^{126}Cd/^{126}Cs= 5*.

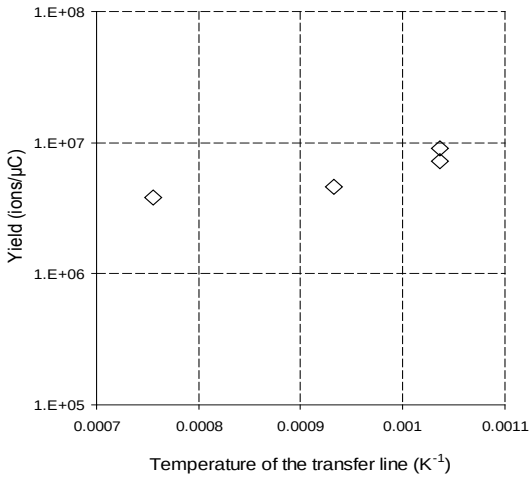

Figure 3.3-2: ***^{75}Zn ($t_{1/2}$= 10.2 s) yield measurements for the <warm line> according to the temperatures, T_1, of the quartz.***

Similar investigations were done on the Zinc element which is also ionised by laser (RILIS) and suffers from contaminations such as Rubidium. As seen previously (**Section 3.2.1**), Rubidium is trapped in the transfer line and the trapping effect depends on the temperature of the quartz. Figure 3.3-2 shows the yields of the ^{75}Zn according to the temperature of the quartz.

3.4 Retention of ^{95,96}Sr, ^{77}Ga and ^{114}In by the quartz

The yields of ^{95,96}Sr, ^{77}Ga and ^{114}In showed to be lower than the typical yields measured with a standard transfer line (table 3.4-1). The <cold line> suppressed the ^{95}Sr and ^{96}Sr by a factor 922 and 248 respectively.

Isotope	*$t_{1/2}$ (s)*	*Transfer line version*	*Ext. heating, Q_{ext} (W)*	*Temperature of the quartz at T_1 (°C)*	*Yield (ion/μC)*	*Yield of a standard transfer line (ion/μC)*	*Suppression factor*
^{77}Ga	*13.2*	*Cold line*	*0*	*308*	***4.8x10^4***	*7.7x10^6*	***2x10^2***
^{95}Sr	*24.3*	*Cold line*	*0*	*308*	***3.6x10^5***	*3.3x10^8*	***1x10^3***
^{96}Sr	*1.07*	*Cold line*	*0*	*308*	***1.5x10^4***	*3.6x10^6*	***2x10^2***
^{114}In	*72*	*Warm line*	*0*	*680*	***2.7x10^5***	*1.8x10^7*	***7x10***
^{114}In	*72*	*Warm line*	*34*	*1100*	***1.2x10^6***	*1.8x10^7*	***2x10***

Table 3.4-1*: Yields of ^{77}Ga, ^{95,96}Sr and ^{114}In isotopes measured with the quartz line and their suppression factors.*

A temperature dependant increase was noticed for the production of ^{114}In *($t_{1/2}$= 72 s)*. At a temperature of *700˚C* (*Q_{ext}= 0 W*) and *1100˚C* (*Q_{ext}= 34 W*) the yield was measured to be *2.7x10^5 ions/μC* and *1.2x10^6 ions/μC* respectively, thus an increase of the yield by a factor 5 at these two temperatures.

3.5 Enthalpies of adsorption for the Rb and Cs onto SiO_2

The suppression factor is not a fixed value for all alkali elements, but it depends on the element with a given adsorption enthalpy and depends on the half life of the isotope (a very long–lived isotope comes through the transfer line while a short-lived one decays before).
As discussed earlier in Chapter 2, effusion is driven by three important parameters which are n_c, the mean number of collisions with the surface of the materials; t_s, the mean sticking time per collision, which depends on the temperature T and the adsorption enthalpy ΔH_{ad}; and t_{fly}, the mean flight time between collision which depends on the geometry of the target and ion source unit, the mass and the temperature.

$$t_{eff} = t_{fly} + n_c \cdot t_s \qquad (3.5.1)$$

With $t_s = t_0 \cdot e^{(\Delta H_{ad} / k_B T)}$ (3.5.2) known as the Frenkel equation; t_0 is the Debye frequency of the material (equal to $2.3x10^{-13}s$ for quartz [Sim-07]); k_B is the Boltzmann constant and is equal to $1.38x10^{-23}$ J/K. The well known general exponential decay expression is

$$N(t) = N_0 \cdot e^{-\lambda \cdot t} \qquad (3.5.3)$$

Where N_0 is the number of radioactive nuclei at time $t = 0$. λ represents the decay constant. The half life of the nuclei $t_{1/2}$ is equal to $\ln(2)/\lambda$.
If one considers that the quartz induces an additional delay on isotope release, by interactions of the atoms with its interface, the fraction of remaining isotopes after a characteristic temperature dependent effusion time is:

$$N(\lambda,T) = N_0 \cdot e^{(-n_c \cdot t_0 \cdot e^{(-\Delta H_{ad}/kT)}) \cdot \lambda} \qquad (3.5.4)$$

Therefore the theoretical suppression factor f_{th} of the nuclei decaying can be generalized for a non uniform quartz temperature T(L) :

$$f_{th}(\lambda,T) = \frac{N_0}{N(\lambda,T)} \qquad (3.5.5)$$

$$f_{th}(\lambda,T) = e^{\lambda \cdot t_0 \cdot \int \frac{dn_{coll}}{dL} e^{(-\Delta H_{ad}/kT(L))} dL} \qquad (3.5.6)$$

For convenience, equation (3.5.6) has been rearranged for a tube of quartz separated into n=5 isothermal regions:

$$f_{th}(\lambda,T) = e^{\lambda \cdot t_0 \cdot \sum_{i=1}^{n} \left\langle (L_i - L_{i-1}) \cdot \frac{n_c}{L} e^{(\Delta H_{ad}/kT_i)} \right\rangle} \qquad (3.5.7)$$

with i being the number of sections of the quartz tube. Equation (3.5.7) is used in the following parts to estimate the enthalpy of adsorption from experimentally measured suppression factors.

Modelling of the dependence of the Rubidium yields with the temperature of the transfer line

According to the data obtained by the ANSYS simulations (figure 3.1-5) and the experimental values from the readouts of the thermocouples (figure 3.1-7), the temperature profile along the line was estimated (figure 3.5-1). The length of the quartz tube was split into 5 equal sections of 1cm each. Therefore, a temperature in each section was set up and calculations allowed finding an enthalpy of adsorption of the Rb onto the SiO_2 material.
For the <*warm line*>, a thermocouple gave the temperature, T_1, measured at the end of the quartz (side of ion source) at different external powers (oven).

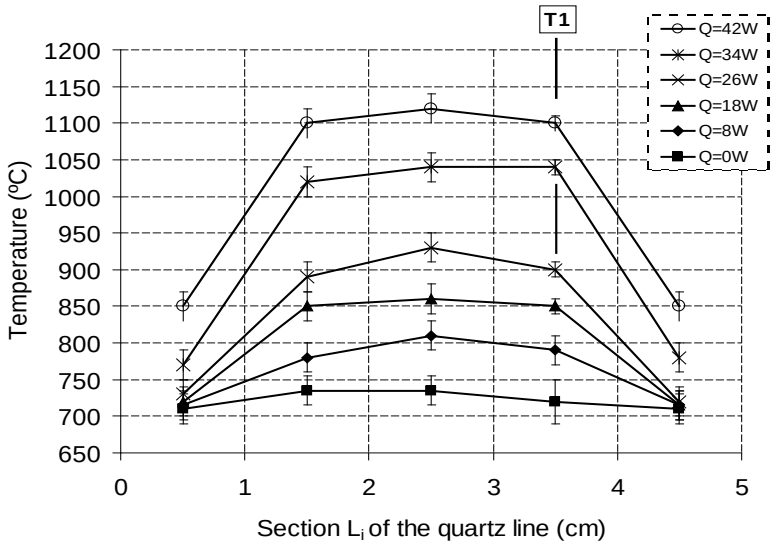

Figure 3.5-1*: Estimation of the average temperatures at each section of the transfer line <warm line> for the quartz location according to the power applied to the external heating. T_1 values are experimental.*

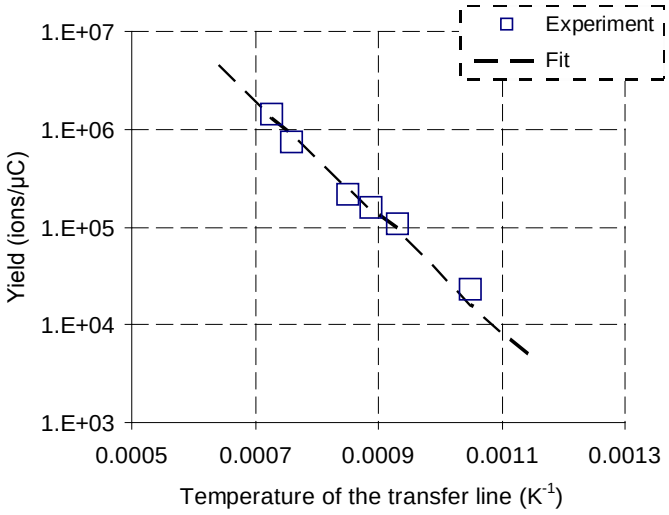

Figure 3.5-2*: Experimental and fitted yield of ^{80}Rb ($t_{1/2}$= 33.4 s) versus the temperature T_1 at the quartz location. Experimental data obtained on the ^{80}Rb with the <warm line> have been fitted. Yield of ^{80}Rb for the <cold line> does not correspond to the fit because of the different temperature profile, see text for the details.*

The observed temperature variation of the suppression factor was fitted with equation (3.5.7) with ΔH_{ad} the only free parameter, n_c= *220 ± 20* collisions deduced from RIBO and the temperature profile from the thermal simulations (ANSYS).

The fit gave ΔH_{ad} = **-242 ± 20 kJ/mol** and good agreement of the model with the experimental data is shown on figure 3.5-2. This shows that the suppression factor originates directly from the specific interaction of Rb with the quartz. Different contributions may affect this estimation and the obtained values, such as impurities from target outgassing. The value of the enthalpy of adsorption is about *85%* of value deduced from isothermal chromatography [Kos-07]

Fitting of the Cesium yields according to the temperature of the transfer line

Similar investigations were performed to analyse the yields obtained with the Cs element in the quartz line, <*cold line*>. Figure 3.1-9 and 3.1-11 shows the ANSYS simulations and the online temperatures obtained. Unlike the <*warm line*>, the <*cold line*> had two thermocouples when online, therefore the temperature profile along the quartz line can be estimated more precisely.
As for the case of the Rb, the length of the quartz tube was also split into 5 equal sections of 1cm each. This allows the set up of a mean temperature in each section finding an enthalpy of adsorption of the Cs onto the SiO_2 material.
For the <*cold line*>, thermocouples gave the temperatures, T_1 and T_2, measured at the end and at the middle of the quartz (figure 3.5-3).

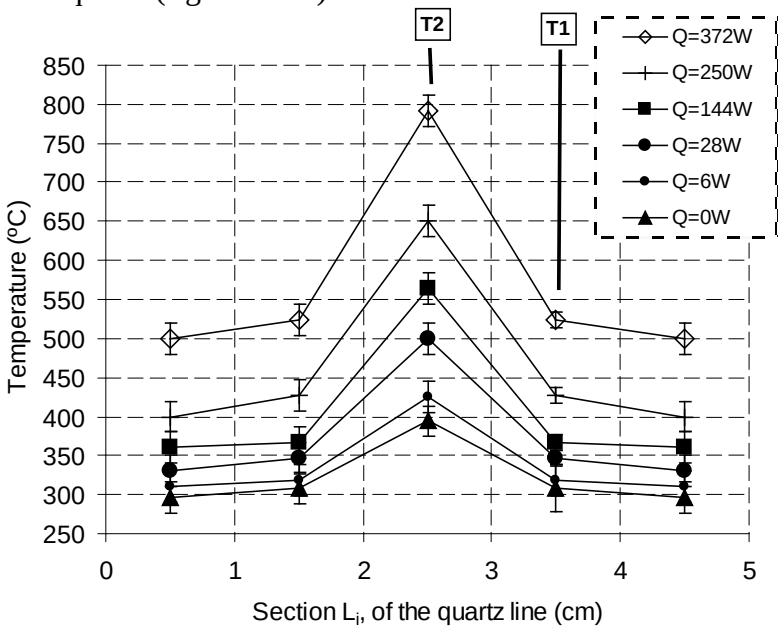

Figure 3.5-3*: Average temperatures at each section of the transfer line <cold line> of the quartz location according to the power applied to the external heating. T_1 and T_2 are experimental points.*

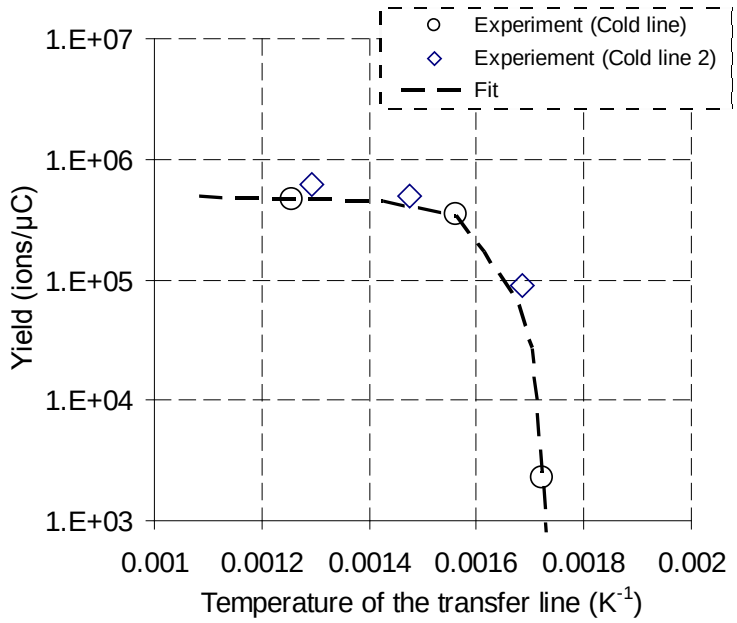

Figure 3.5-4*: Experimental and fitted yield of ^{126}Cs ($t_{1/2}$= 98.4 s) versus the temperature T_1 at the quartz location.*

As the external heating system was different from the <*warm line*> to the <*cold line*>, it was shown that the profile of the temperature inside the tube of quartz was also different from one to another. For the <*warm line*>, the profile of the temperatures tends to take a Gaussian shape when the power of the oven is increased while for the <*cold line*> unit, this profile takes a triangular shape. This is due to the cooling block which is in direct contact at the two extremities of the transfer line and therefore, when increasing the power of the external heating, the middle of the quartz sees its temperature increasing much faster than at the extremities: when no heating is applied (Q_{ext}=*0W*), T_1 and T_2 equal to *308ºC* and *351ºC* respectively; on the other hand, when a power of 372W is applied to the external heating, T_1 and T_2 equal to *524ºC* and *792ºC* respectively. This means that an increase of *372 W* induced a gap of about *270ºC* between the centre and one of the extremities of the quartz tube.
The temperature variation of the suppression factor (figure 3.5-4) was fitted with equation (3.5.7) with ΔH_{ad} the only free parameter, n_c= *220 ± 20* collisions deduced from RIBO and the temperature profile from the thermal simulations (ANSYS). The fit gave ***ΔH_{ad} = -145 ± 20 kJ/mol*** for the Cesium. It was shown that the experimental yields measured with the <*cold line 2*> coincide with the fit established using the yields obtained with the <*cold line*>: this is due to a similar design. The value of the enthalpy of adsorption for the Cesium is about *80%* of value deduced from isothermal chromatography [Kos-07]
The alkali retention onto the quartz depends on the temperature, the profile of the temperature along the quartz and the enthalpies of adsorption. For temperatures below 300*ºC* of the quartz, Cd and Zn are trapped and do not reach the ion source. The purification effect is obtained when the temperature is tuned such that the contaminant is retained and the element of interest goes through the transfer line. The temperature is not distributed homogeneously along the quartz tube (fig. 3.1-9, 3.1-11 and 3.1.14) and each quartz transfer line has its own profile of temperature. A better temperature profile leads to a better trapping efficiency of the alkalis.

Chapter 4

Effusion and Decay Losses of a Multi Body Target Coupled to one Ion Source

In ISOL (Isotope Separator On-Line) facilities, radioactive nuclides are produced by spallation, fission or fragmentation reactions in a thick target with a high energy proton or light ion beam of either *1 GeV/nucleus* (EURISOL), *1.4 GeV/nucleus* (ISOLDE) *or 500 MeV* (TRIUMF). They diffuse within the target material and effuse out of the target vessel through a transfer line to the ion source where they are ionised and extracted.
The EURISOL Design Study describes *100 kW* direct target stations to produce the proton rich radioactive ion beams. The power deposited by the beam exceeds the heat that can be dissipated by one target unit. A system composed of 1 to 4 target containers coupled to one single ion source dissipates *100 kW*. At 100 kW incoming beam power, efficient heat dissipation schemes and efficient effusion process are mandatory. The effusion of radioisotopes induces decay losses that have to be calculated and the geometry optimized [Eur-08]. This chapter presents the effusion process studies in a double container configuration. The design and the online tests of a double transfer line prototype linked to a FEBIAD plasma ion source are presented. The experimental results obtained at ISOLDE are used to benchmark the software tools mandatory to develop future multiple target units.

Bivalves, Bi-Valve, Bivalvia…
As the main characteristic of this prototype consisted of two transfer lines having a valve each, the name of **Bi-Valve** was given to ease the reading of the following sections of this thesis. The reader has to pay attention that the **Bi-Valve** has nothing to do with **Bivalves** which correspond to a molluscs belonging to the class **Bivalvia**.

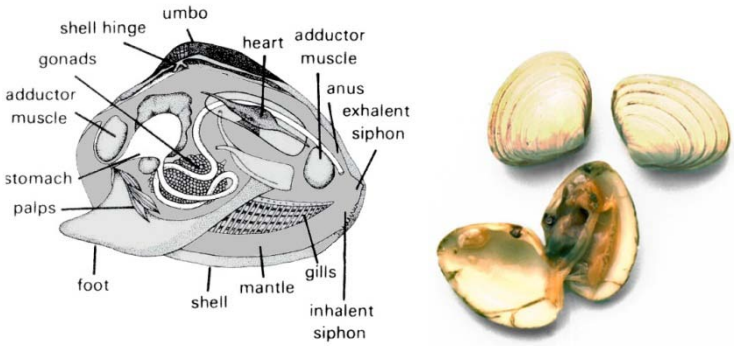

Figure 4-1.0: ***General anatomy of the Bivalve [Mol-00]***

''Bivalves are characterized by two oval or elongate valves, which enclose the organism's body. If the valves are a mirror image of each other then they are said to be equivalved. If not, they are inequivalved. The valves are joined dorsally by a toothed hinge, which prevents the shell from being misplaced when opening and closing. An internal elastic ligament automatically opens the valves, but by contracting one of two of its adductor muscles it is able to hold the shell shut. The first part of a bivalve shell to develop is the umbo which is seen as a large bump towards the anterior end of the dorsal side of the shell.
Bivalves are entirely aquatic and rather stationary organisms. To feed they use siphons. One siphon will carry water to the internal cavity and is known as the inhalant siphon, the other takes water away from the internal cavity and is known as the exhalant siphon. In certain cases these siphons can become fused, but the water in the two tubes still remains separate. Once inside the bivalve the water runs past ciliated gills, which sift out any food particles.
Bivalves also possess a muscular foot which they use to attach themselves to the substrate and/or burrow down into sediments.'' [Bri-00]

- No animals were harmed nor submitted to radiation during the making of this prototype -

4.1 Design of a dual target-transfer line unit (Bi-Valve)

To perform tests of such prototype at ISOLDE, full compatibility with the facility must be ensured. The configuration of the ISOLDE front-end did not allow distributing the proton beam onto different targets. The target sub-units to be irradiated were thus aligned with respect to the axis of the incoming beam. Each of two transfer lines merged into the FEBIAD ion source and the system was equipped with remotely driven valves to have a full control on the opening/closing state on each of the transfer lines. A dual independent valve system was developed and integrated. Simulations of the Energy Deposition and the Heat Transfer were performed with FLUKA [Fas-03; Fas-05] and ANSYS [Ans-08] respectively to design the prototype (figure 4.1-1).

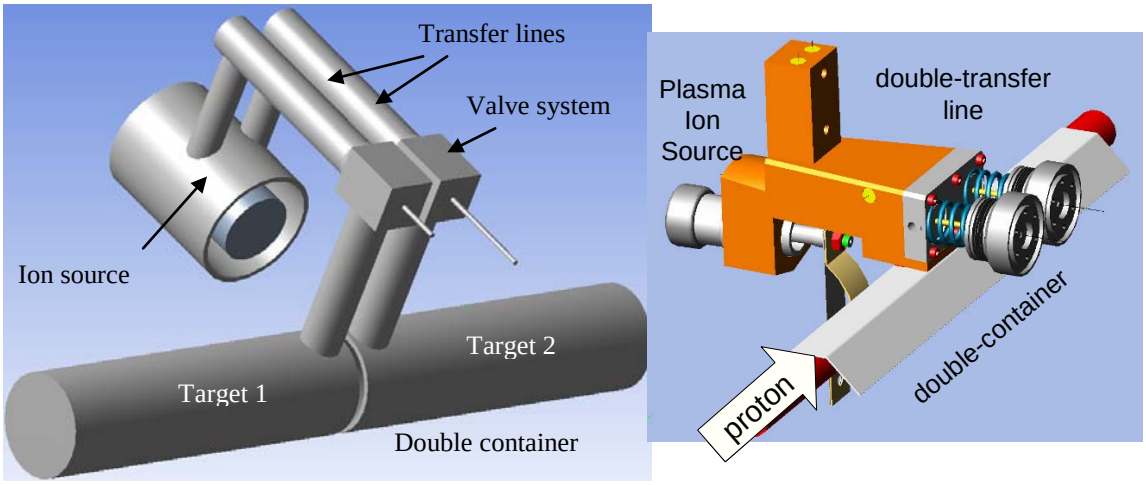

Figure 4.1-1*: Drawings of the Bi-Valve prototype concept showing the double container, the target 1 and 2, the ion source, the double-transfer line and the direction of the incoming proton beam.*

4.1.1 Isotope production and energy deposition in a double CaO target

Oxides are one of the most target materials used at ISOLDE; they have the properties of being less risky with respect to the radio-protection point of view (light materials used).

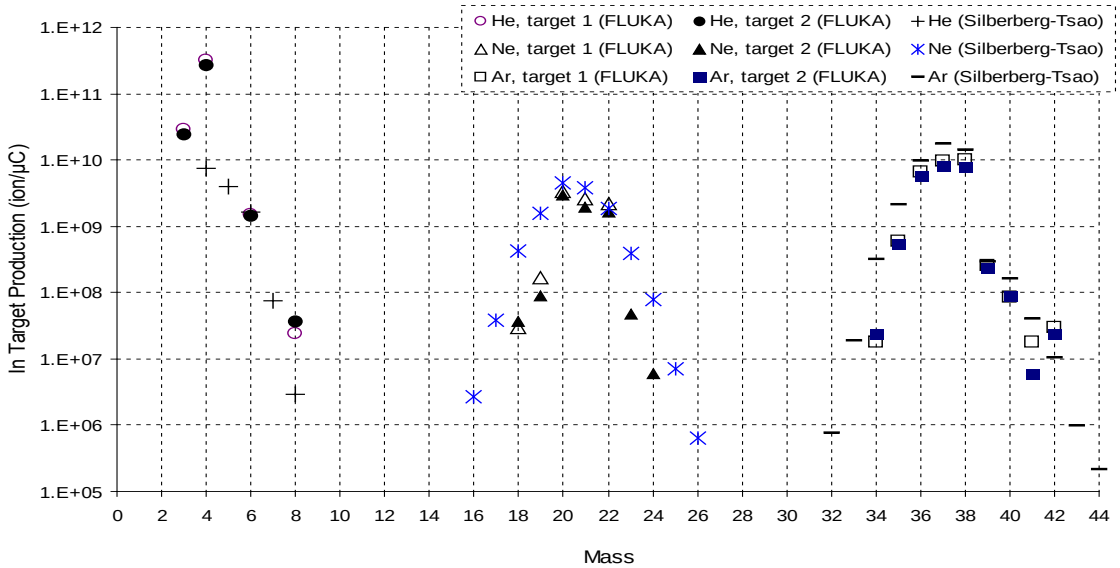

Figure 4.1-2*: Isotope productions of Ar, Ne and He in each side of the container (in target 1 and target 2), simulated with FLUKA and SigmasWIN2000 for CaO as target material. (Statistics on 2,000,000 primary particles)*

Among these materials, CaO has been chosen to be the target material for the prototype: the releases of isotopes coming from such a target are very well known and therefore it constitutes the best candidate for this present study. Produced Ar permits to use this element as a reference for the ISOLDE FEBIAD ion source. Studying He, Ne and Ar isotopes is particularly useful to make a comparison with ISOLDE yields of standard target unit.

Isotope productions simulated with FLUKA and SigmasWIN2000 [Sil-73] are shown on figure 4.1-2. Despite the differences of the two codes (SigmasWIN2000 will tend to overestimate productions), in-target isotope productions from a CaO target, especially for ^{35}Ar and ^{18}Ne elements have been estimated. The production of He, Ne and Ar isotopes is very similar in each part of the double container; the local energy deposition, simulated with FLUKA [Fas-05; Fas-03] is slightly asymmetric (figure 4.1-3). Integrating over the length of target 1 provides a deposition of *2.1%* (±0.1%) of the incoming power while *1.8%* (±0.1%) is deposited in target 2: these represent a dE/dx loss of 29 MeV (±2 MeV) and 26 MeV (±2 MeV) respectively of the incoming beam power.

This slight inequality between both containers leads to a temperature difference of a few degrees centigrade and therefore of small impact on the process of the isotope release. For a primary beam of *2 kW*, the total power represents *78 W* which is much lower than the external joule heating of *1.1 kW* used to reach the temperature of operation (*1400°C*). This difference would be rather important when using a higher power for the incoming beam; indeed the power deposited would become then so significant that no ohmic heating would be necessary to heat the target up.

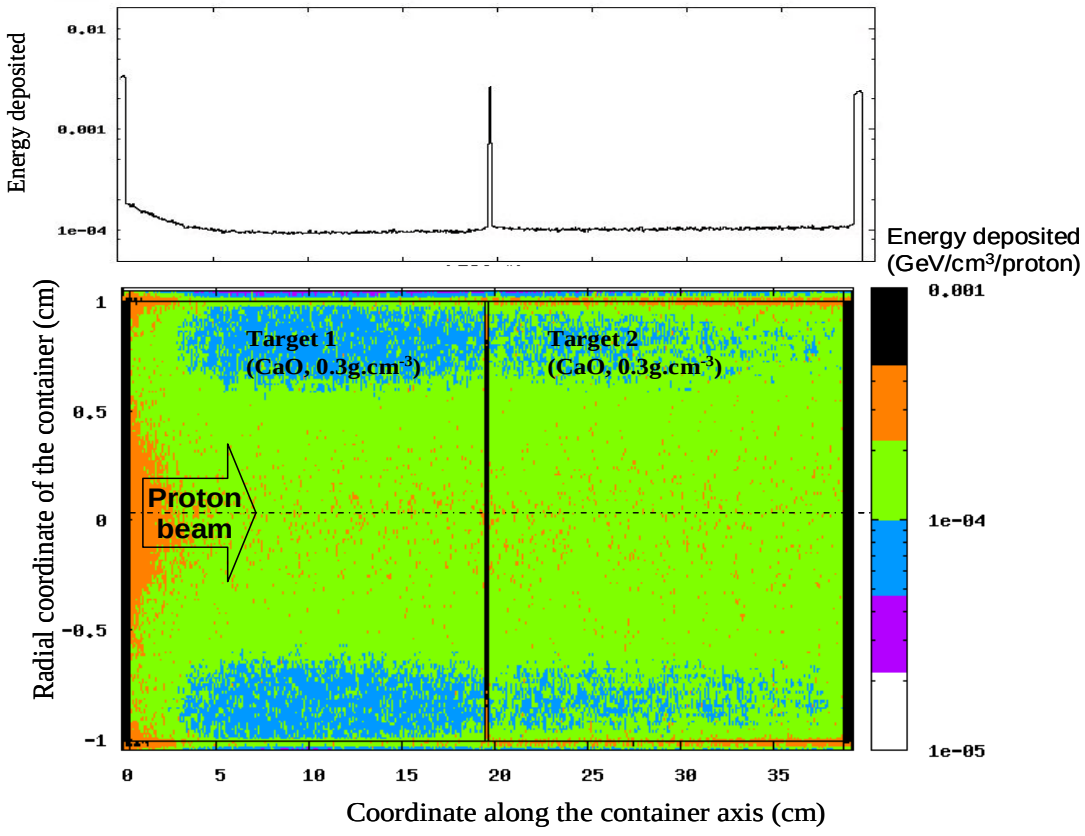

Figure 4.1-3*: Energy deposition within the Bi-Valve double-container simulated by FLUKA. The peaks of energy at the two extremities correspond to the Ta caps (δ = 16.6 g.cm^{-3}, d = 0.4 cm thick) closing the container, while the peak in the middle represents the Ta wall (d = 0.1 cm thick) separating target 1 from target 2.*

4.1.2 Engineering of the Bi-Valve

Several iterations were required to develop the adequate engineering solution of the concept shown on Figure 4.1-1. The main constraints for the unit were:

- Material chosen to resist to radiations and high temperatures.
- Remote controlled valves and reliability of the system: be sure that the valves close/open as needed.
- Coupling the prototype valve system onto the ISOLDE Front End configuration and associated services (ie: cables, robot handling).

Therefore the main choices for the unit were:

- Two *200 mm* long cylinder containers and *10 mm* in radius.
- Two Tantalum vertical transfer lines of *4 mm* radius connected to the two containers.
- Water-cooled Cu block surrounding the Ta transfer line connected to a plasma ion source (FEBIAD).
- Modified Al vacuum vessel to host the pneumatic actuation of the valves system.

The principle consists in having two symmetrical targets linked to two parallel transfer lines as shown on figure 4.1-4. Each transfer line has a pneumatic valve which is remotely controlled by a computer's program. To preserve similar effusion characteristics as those present in an ISOLDE standard unit, similar length was kept for the transfer lines of the prototype. The chimneys (vertical transfer lines) were each symmetrically connected at *1.5 cm* from the middle of the double container (figure 4.1-5) (in a standard ISOLDE target the chimney is in the middle of the *200 mm* long container).

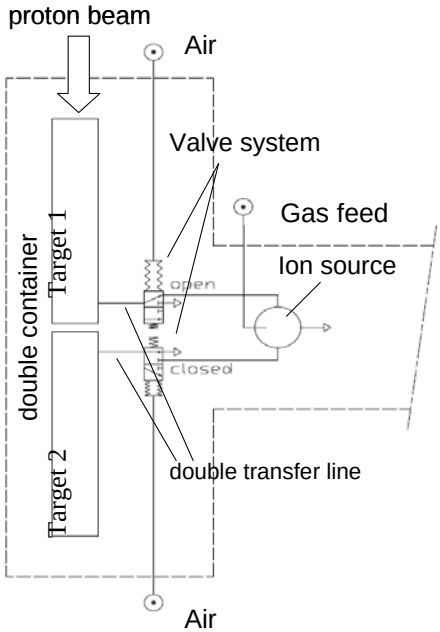

Figure 4.1-4*: Schematic layout of the double-container prototype displaying the double transfer line, the valve system, the double-container, the target 1 and 2, the ion source, the gas feed and the pneumatic air connections.*

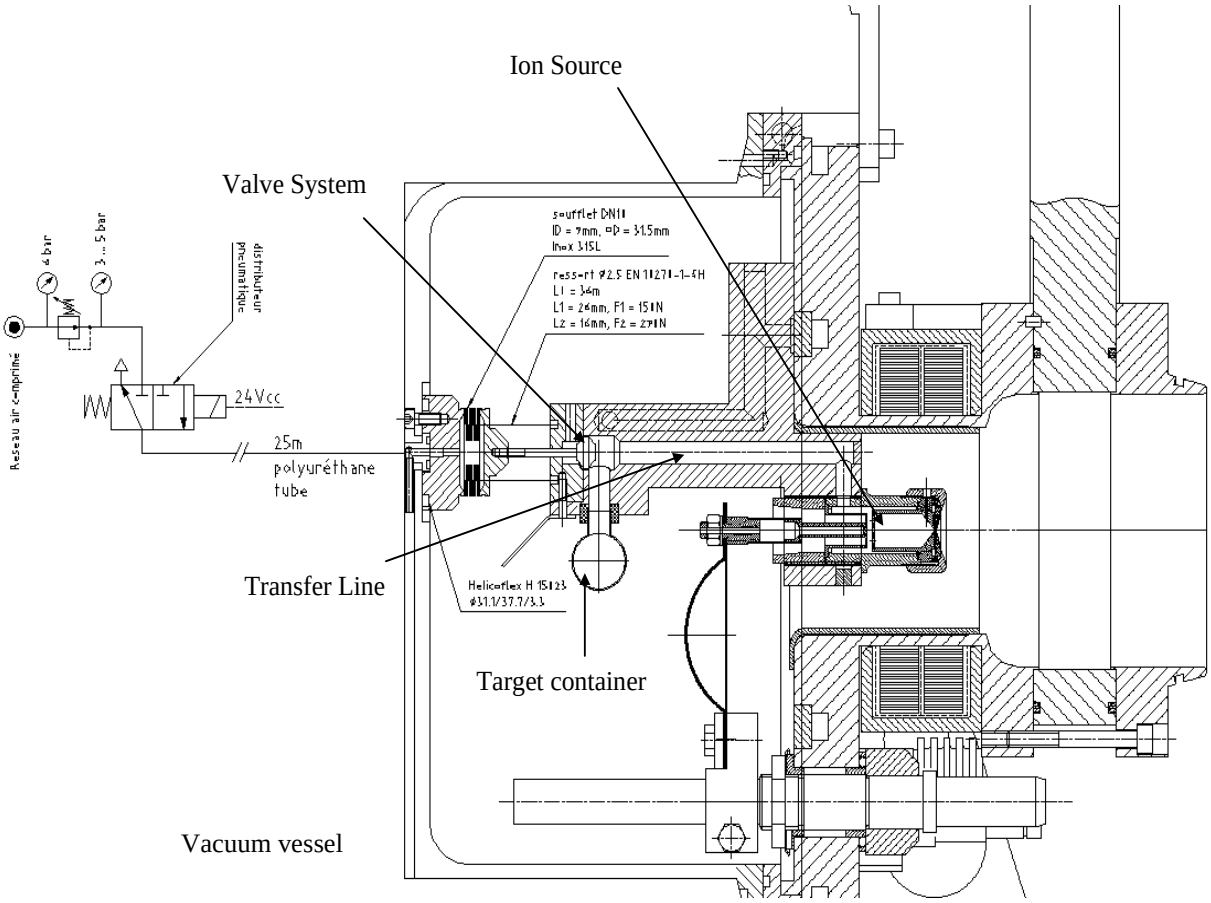

Figure 4.1-5*: General layout of the whole Bi-Valve prototype with the valve control system, the ion source, the target container and the vacuum vessel.*

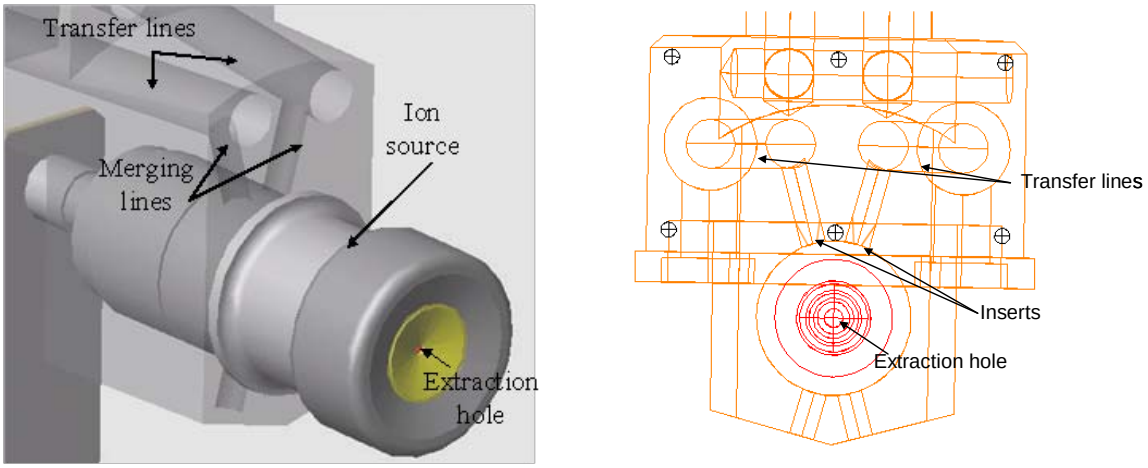

Figure 4.1-6: ***Drawing of the transfer lines of the Bi-Valve merging into the ion source. The conic inserts (0.8 mm diameter) to restrict the entrance into the ion source are shown (extraction hole diameter: 1.5 mm)***

To minimize the probability that an isotope produced effuses from one transfer line to the second one instead of being directly extracted, the lines merging into the ion source chamber consisted of a conic insert to restrict the diameter of the entrance at *0.8 mm* (*4 mm* diameter for a standard target-ion source unit operating at ISOLDE) and were designed as showed in figure 4.1-6. Surface ratio calculations estimated that reducing the entrance of the transfer lines into the ion source from *4* to *0.8 mm* (which is almost half size of the extraction hole)

set up to *63%* the probability that an isotope will go to the extracted hole instead of either going to the other transfer line or coming back to the line it is coming from). Using two standard diameters for the exit of the transfer lines set up this probability to *7%*.
Several configurations were investigated before achieving an appropriate tightness of the valve system. One consisted in establishing a contact of the piston against an O-ring in EPDM (ethylene propylene diene monomer) when closing. After off-line investigations, it appeared that the O-rings started to melt for temperatures above *150°C* and lost leak tightness very rapidly. Figure 4.1-7 shows the degradation of the O-rings after a couple of hours.
Another approach consisted in making a metal to metal valve contact with a stainless steel piston and a ring in copper (figure 4.1-7). The contact force was limited (*<150 N*) from the maximum pressure applied by the bellows (*5 bar*); the surface of contact was thus increased and the metal surface polished to get a better tightness. After off-line tests, it appeared that it was not yet sufficient and there was a progressive transfer of matter between the stainless steel and the copper materials. Therefore this solution was dropped.

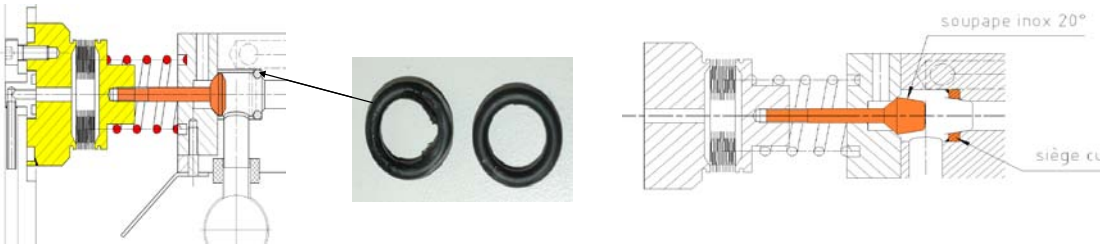

a) b)

Figure 4.1-7*: Configuration involving a) O-rings for the valve system – Picture of the O-rings after off-line tests; b) metal to metal valve contact.*

A third approach was to replace the copper ring by a flat ring made of different material such as Papyex on the front and the back of the piston (figure 4.1-8). A stainless steel tube was also inserted around the piston to avoid unwanted chemical reactions.
Off-line test results showed a leak rate of $1x10^{-5}$ *mbar L/s*, too high to perform online tests with an acceptable quality which is expected to be lower than $1x10^{-8}$ *mbar L/s (*to avoid important additional leaks to the systematic ones already existing for usual targets). Moreover this graphite grade had an intrinsic porosity thus preventing to reach the appropriate leak rate.

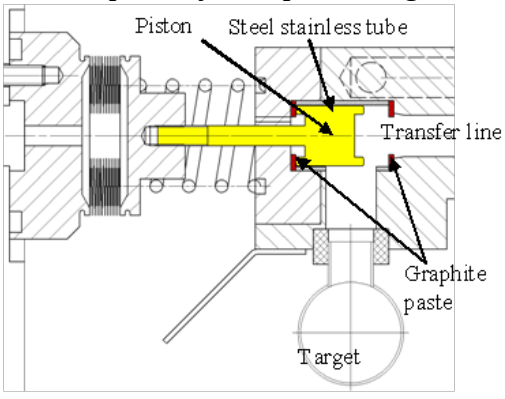

Figure 4.1-8*: Valve system involving graphite and steel stainless tube*

Therefore the choice was made to use O-rings with specific characteristics with respect to radiation levels and to decrease the temperature at this location to below their melting point.
O-rings made of PUR, Copolymer of vinylidene fluoride and hexafluoropropylene were tested. Off-line results showed a leak rate of $1x10^{-9}$ *mbar L/s* acceptable for the tests to be performed. However the maximum operating temperatures for PUR and EPDM are *80°C* and *100*°C respectively. Therefore Viton (FKM) material was chosen instead due to its higher

resistance to heat: *200°C* over a long time and *250°C* over a short time. A tightness value of $1x10^{-10}$ *mbar L/s* was obtained with this last material when the target container was kept at room temperature.
To determine the temperature at the valve position with a container at *1400°C*, ANSYS simulations [Ans-08] were done and predicted a temperature of *577°C* (figure 4.1-9). It is *300°C* above the standard operating value for the selected the O-ring made of Viton.

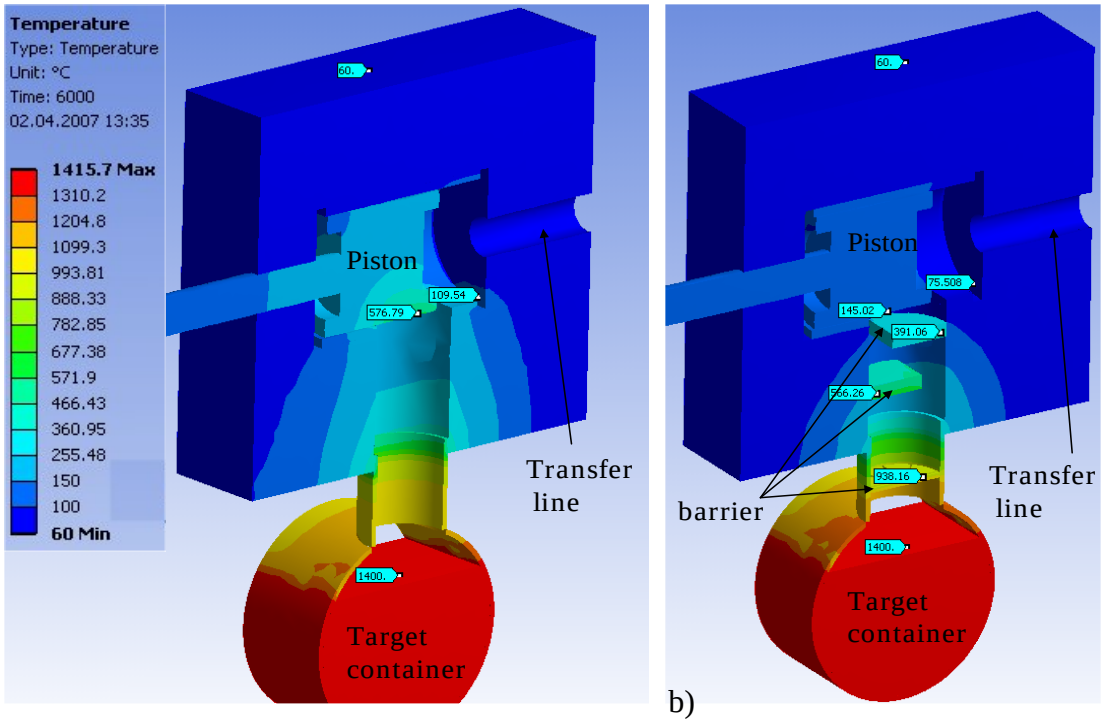

Figure 4.1-9*: Drawing of the heat transfer simulation done with ANSYS without (a) and with (b) internal thermal screens (barriers).*

The piston was heated by thermal radiation from the target container. To block the direct view between the target and the valve system, a thermal barrier consisting of three Tantalum heat screens was placed on the vertical transfer line. The surface of the piston was also polished in order to reflect as much as possible the heat (reducing its emissivity to a minimum value). With these modifications the temperature at the valve location was estimated to be at *145°C* by new numerical simulations. To test this result, the container of the prototype was left under a stabilized temperature of *1400°C* during *1h*. No damage was observed on the structure of the O-ring.

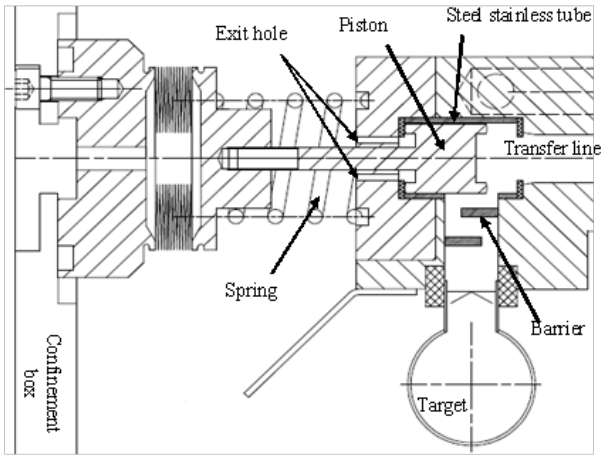

Figure 4.1-10*: Valve and its actuator showing the stainless tube, the piston, the barriers and the rear hole. The valve is in position O (Open): the isotopes produced can lead to the transfer line.*

The final valve system tested (figure 4.1-10) consisted of barriers, a stainless tube and six horizontal exit holes of *1 mm* radius each placed in the back of the block in order to allow the isotopes to be released in the vacuum vessel when the piston is closed.

Control of the valve system

The valve system was controlled from the Ethernet network. A LabVIEW programme [Lab-08] allowed the remote control of the piston with two distinct positions. Figure 4.1-11 shows the schematic layout of the whole network and the two valves used. Four combinations with the valves 1 and 2 were possible as explained in the figure next page. The state 'O' stands for 'Open': the valve allows the isotopes produced in the target to pass through the transfer line and to lead to the FEBIAD ion source. The state 'C' stands for 'Closed': the piston blocks the transfer line and opens the rear exit holes to the vacuum, the valve does not allow the isotopes produced to pass through the transfer line therefore they are released into the vacuum vessel.

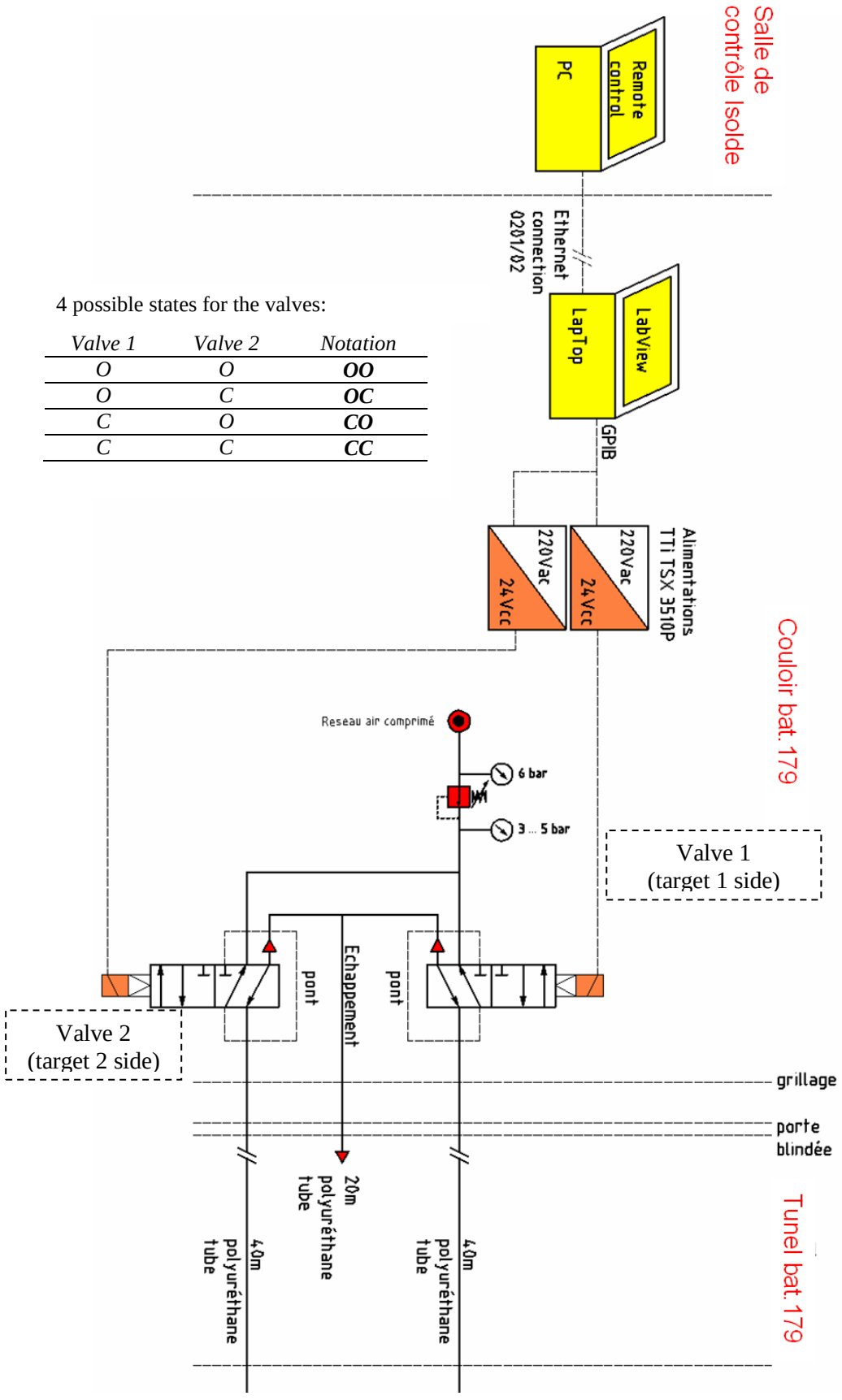

4 possible states for the valves:

Valve 1	*Valve 2*	*Notation*
O	*O*	***OO***
O	*C*	***OC***
C	*O*	***CO***
C	*C*	***CC***

Figure 4.1-11*: Functional drawing of the controlling system. The valves 1, 2 and their states are showed. The state 'O' stands for 'Open' (the valve allows the isotopes produced in the target to pass through the transfer line). The state 'C' stands for 'Closed' (the valve does not allow the isotopes produced to pass through the transfer line and are then released in the vacuum vessel through the rear exit holes).*

4.1.3 Settings of the FEBIAD Ion Source with Ar/Xe and Kr gases

The prototype properties have been investigated on the ISOLDE off-line separator; the goals were to monitor:

- Ionisation efficiency for Ar (Argon) and Kr (Krypton) using Ar/Xe and Kr injection with a calibrated leak. Ar/Xe was injected after the valve system close to the ion source while the Kr was injected from one side of the double-container (before the valves).
- Gas-tightness of the valves changing the valve states.
- Possible impact of the Bi-Valve system on the ion source behaviour.

To investigate the dependence of the ion source operation on the valve system state, ionisation efficiencies of Ar and Kr were measured. Figure 4.1-12 represents an off-line mass scan. Ar/Xe gas was injected in the ion source through a calibrated leak to check its efficiency and its good operation. An increase of the Ar ion efficiency was observed upon variation of the temperature of the cathode.

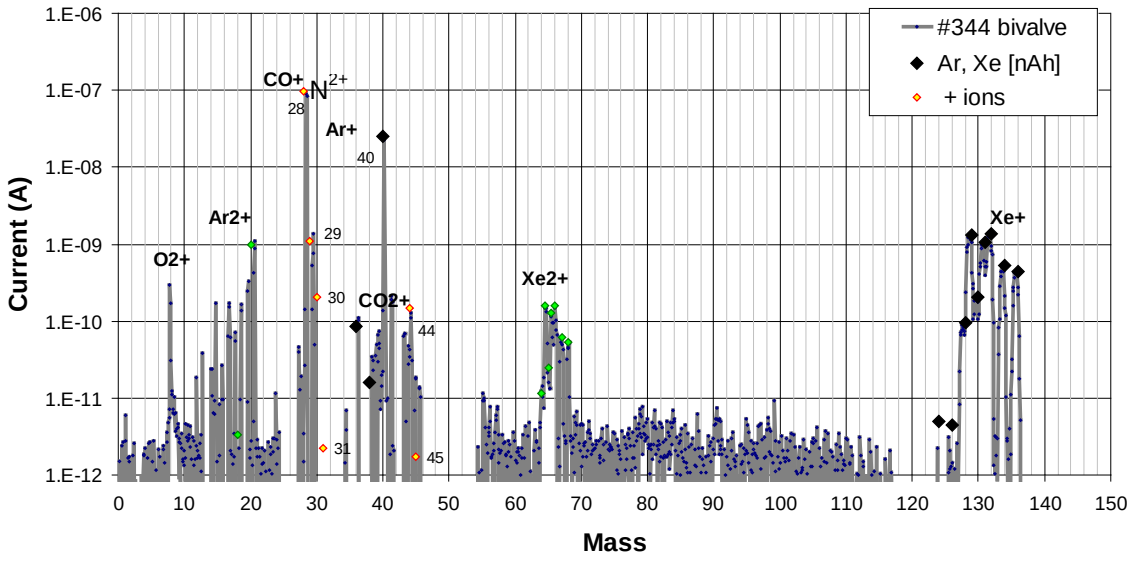

Figure 4.1-12*: Offline mass scan results. Valve 1 and 2 were open (state OO). Temperature of the container was 1380ºC.*

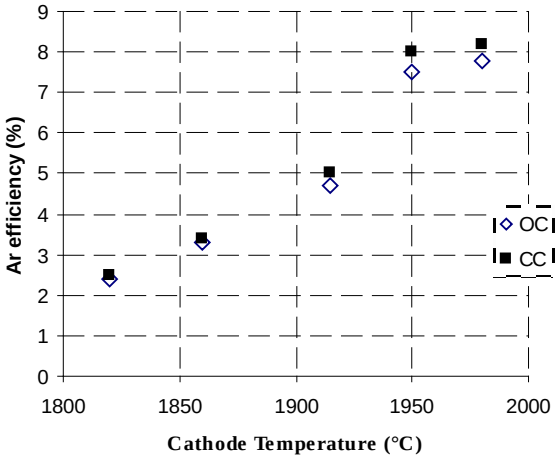

Figure 4.1-13*: Plot of the Ar ionisation efficiency versus the temperature of the ion source and to the valve position: CC and OC. The temperature of the container was 1380°C.*

The Ar efficiency as a function of the cathode temperature is shown in figure 4.1-13. A variation of the Ar current was noticed according to the position of the valves. A fall of *7%* in the extraction current (target and line current at *400 A* each) was observed immediately after one of the two valves was open (state OC or CO), as compared to when both were closed (state CC). A fraction of the injected gas went through the transfer line from where the valve was open instead of being extracted directly by the ion source. Confirmation of this behaviour was shown when sending Kr from one of the two containers (target 1) (figure 4.1-14).

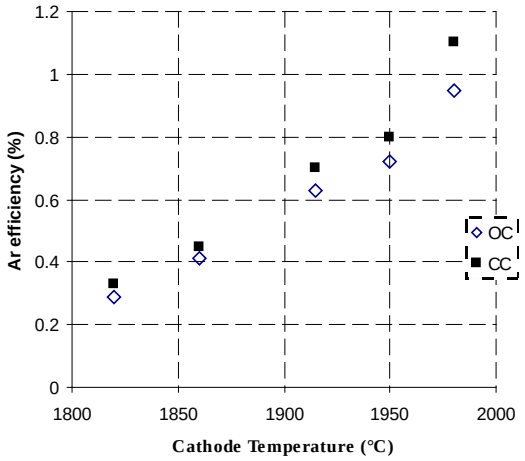

Figure 4.1-14: Plot of the Ar ionization according to the temperature of the ion source and to the valve status (CC and OC) with Kr injection. The temperature of the container was 1380°C.

4.2 Release of $^{34, 35}$Ar and $^{18, 19}$Ne noble gases from the Bi-Valve

4.2.1 Tightness and symmetry of the double target-line measured with $^{34, 35}$Ar.

Some 30% unusual fluctuations were observed at the tape station during online tests due to unexpected instability which were not linked to instabilities related to the operation of the double target-line itself. These fluctuations implied the measurement of five values for a same delay time when doing the release curves (figure 4.2-1).

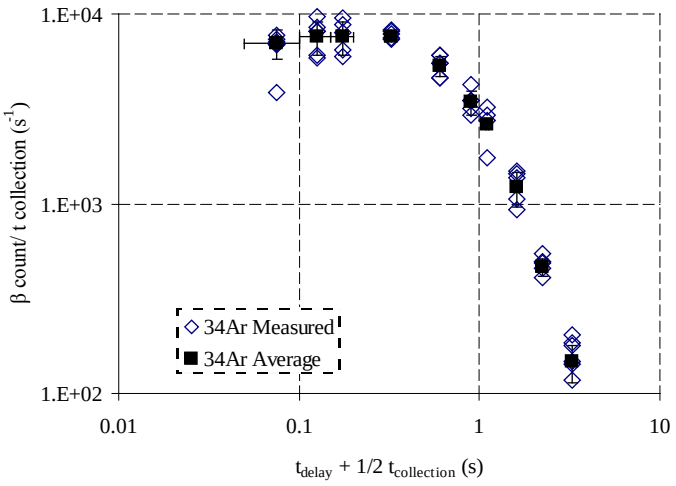

Figure 4.2-1*: Example of fluctuations in the measurement of the release of ^{34}Ar ($t_{1/2}$= 844 ms). For each point, five values were measured and averaged. Collection times are represented by the horizontal bars.*

To ease the calculation of the yields for each of the isotopes measured for each state of the valves, an average of the values at each point of the curves has been calculated.
The release curves of ^{34,35}Ar for all possible valves' positions are shown on figure 4.2-2 and 4.2-3 respectively. The states OC and CO of the valves lead to slight differences in the shape of the release curves. As discussed previously in figure 4.1-3, the energy deposited by the incoming proton beam within the double container was slightly greater in the target 1 than in the target 2 but did not explain any sufficient change in the temperature coming from this difference to influence the release process. A possible reason of such differences in the release curves might be due to a non perfect alignment of the double-container to the proton beam which leaded to a better diffusion in the target 1. Also both parts of the double-container might not be filled in a 100% similar way with CaO materials.

At an ion source temperature of *2100°C*, when both valves were closed (CC), the measured ^{35}Ar yield was $7.6x10^3$ *ions/μC*, compared to $2.6x10^6$ *ions/μC* when both valves were open (OO). For the same temperature, the measured ^{34}Ar yield was $4.8x10^2$ *ions/μC* (CC) compared to $1.9x10^5$ *ions/μC* (OO) (figure 4.2-1). This indicated a total relative leak rate of *0.29% (± 0.02%)* which was of good quality to perform the tests.

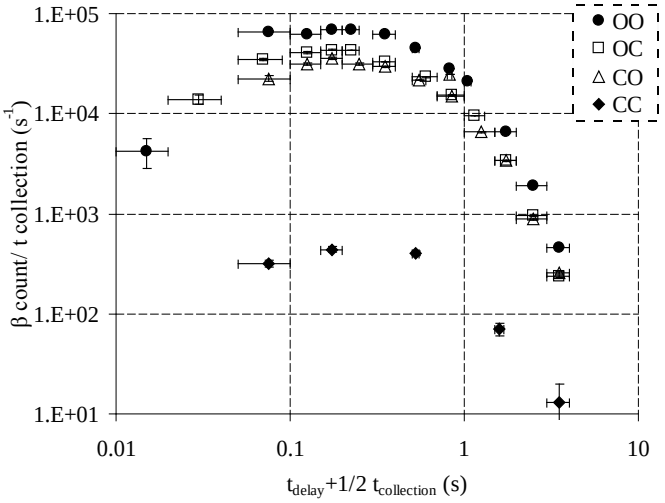

Figure 4.2-2*: Release of ^{34}Ar ($t_{1/2}$= 844 ms) according to the position of the valves*

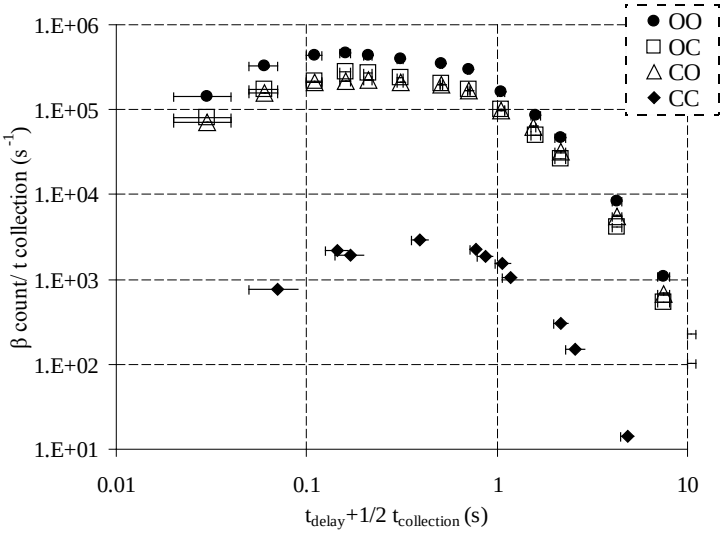

Figure 4.2-3*: Release of ^{35}Ar ($t_{1/2}$= 1780 ms) according to the position of the valves (O stands for Open; C stands for Closed).*

4.2.2 Impact of the operating modes on ion source efficiencies and yields of $^{18, 19}$Ne and $^{34, 35}$Ar

The online tests, two temperatures of operation of the FEBIAD ion source were chosen *(1920°C* and *2100°C)*. This resulted in an increase of the yields of up to a factor 7 for *180°C* difference (table 4.2-1). The efficiency of the FEBIAD ion source increased from *2.3* to *4.9%* when all valves were open and from *2.5* to *5.1%* for the other configurations.

Ratio of the ion source efficiencies for the different operating temperatures gave εff(OO)/εff(CO) = *0.92* when the ion source was at *1920°C* and εff(OO)/εff (CO) = *0.96* when the ion source was at *2100 °C*. This may due to a re-visit phenomenon of the isotopes through the lines instead of being ionised. At *2100°C*, the probability that an isotope is ionised by the source is higher, therefore the nuclide does not re-visit or visit the other transfer line when all valves are open. This hypothesis will be investigated further in the following section using the RIBO code in order to estimate the impact of the geometry of this double target-line on the effusion process. Such increase in the yields when changing the temperature of the ion source might also be directly linked to possible thermal radiations coming from the source and therefore eating up the double-container.

Isotope	$t_{1/2}$ (s)	Ion Source Temperature (ºC)	Yields** (ions/μC) for different valve positions						
			OO	Eff_i (%)	OC	Eff_i (%)	CO	Eff_i (%)	CC
^{34}Ar	0.844	1920	$4.9x10^4$	2.3	$2.7x10^4$	2.5	$2.3x10^4$	2.5	-
^{35}Ar	1.780		$3.9x10^5$		$2.5x10^5$		$2.6x10^5$		-
^{19}Ne	17.22		$5.7x10^4$	-	$2.2x10^4$	-	$3.4x10^4$	-	-
^{34}Ar	0.844	2100	$1.8x10^5$	4.9	$1.0x10^5$	5.1	$9.8x10^4$	5.1	$4.9x10^2$
^{35}Ar	1.780		$2.6x10^6$		$1.6x10^6$		$1.5x10^6$		$7.6x10^3$
^{18}Ne	1.670		$5.3x10^4$	-	$3.8x10^4$	-	$4.6x10^4$	-	-

Table 4.2-1: ***Yields and ion source efficiencies of ^{34,35}Ar and ^{18,19}Ne for different position of the valves (O: Open Valve, C: Closed Valve) and for different ion source temperatures.***
Due to the fluctuations in the measurements, errors in the yields were estimated to be between 7 and 18% according to the number of values measured for each point when doing the release curves.

The measured yields were in the range of those produced by a standard ISOLDE CaO target *0.4 g.cm^{-2}* thick as presented in table 4.2-2. The double target-line unit as designed produced nominal $^{34, 35}$Ar yields.

Isotope	$T_{1/2}$ (s)	Typical Yield (ions/μC)	Typical Ion Source Efficiency, Eff_i (%))	Source Temperature (°C)
^{18}Ne	1.670	$1.2x10^5$	0.9	2100
^{19}Ne	17.22	$5.9x10^5$	0.9	2100
^{35}Ar	1.780	$4.2x10^6$	5	2100

Table 4.2-2*: Typical yields of ^{35}Ar and ^{18,19}Ne of a standard CaO ISOLDE target (0.4 g.cm^{-2} thick), PS Booster [Iso-00].*

Although errors in the yields were estimated to be between *7* and *18%*, the comparison of the yields for one of the possible states of the valves (OC, CO) to the case where all valves were open (OO), showed that the yields of ^{34}Ar (ion source temperature *1920°C* and *2100°C*) and the yields of ^{35}Ar *($t_{1/2}$= 1.780 s)* (ion source temperature *2100°C*) would tend to be greater when the valves were in OC state (figure 4.2-4).

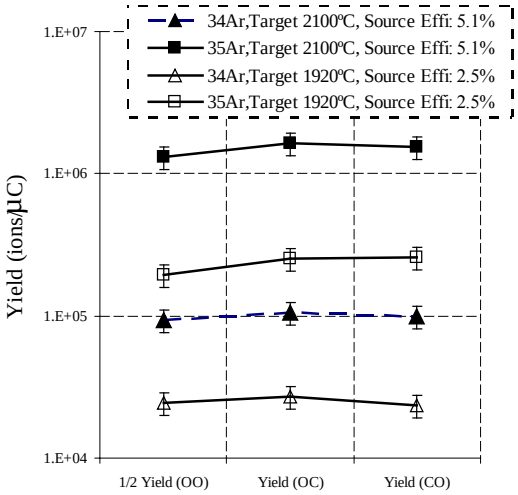

Figure 4.2-4: Yield of ^{34,35}Ar for all possible states of the valves for the two modes of operation of the FEBIAD ion source. Errors in the yields were estimated to be between 7 and 18% according to the number of values measured for each point when doing the release curves.

The yield of ^{34}Ar *($t_{1/2}$= 0.844 s)* (ion source temperature *1920°C*) did not seem to follow this trend of having the highest value for a valve's state OC; this might be due to statistical reasons. Indeed the yields of ^{34}Ar (ion source temperature *1920°C*) for states CO and OC were shown to be very close giving a ratio of 1.06. This made difficult any clear deduction on the effect of the valves state in the ^{34}Ar at this precise temperature.

4.2.3 Time structures, impact of the dual transfer line on the effusion process and decay losses

The sum of the yields from each independent transfer line did not equal to the measured yields when the valves were simultaneously open (table 4.2-1). This non additive phenomenon originated from two possible causes. The first might be due to the fraction of the isotopes which revisited the second transfer line and container before getting ionised in the source. The second would be due to the decrease of the ion source efficiency when the two valves were open (OO).
Table 4.2-3 shows the rising times ^{34,35}Ar and ^{18,19}Ne for each position of the valves accounting to a part of the delay time needed for the isotopes to effuse from the target container to the extraction hole of the ion source (Chapter 2.5). No clear significant differences in the rising times were noticed according to the states OO-OC-CO of the valves for most of the isotopes studied due to large error bars. ^{35}Ar was the only element to show a better effusion time for valve states' OC and CO at the two different ion source temperatures.

		Ion Source	*Rising times (ms) for different valves positions*			
Isotope	*$t_{1/2}$ (s)*	*Temperature (ºC)*	*OO*	*OC*	*CO*	*CC*
^{34}Ar	*0.844*		*135 ± 7*	*133 ± 7*	*158 ± 85*	-
^{35}Ar	*1.780*	*1920*	*102 ± 7*	*97 ± 12*	*89 ±18*	-
^{19}Ne	*17.22*		*109 ± 5*	*102 ± 10*	*123 ± 9*	-
^{34}Ar	*0.844*		*131 ± 3*	*131 ± 6*	*120 ± 20*	*284 ± 33*
^{35}Ar	*1.780*	*2100*	*86 ± 3*	*80 ± 2*	*70 ± 2*	*296 ± 55*
^{18}Ne	*1.670*		*181 ± 11*	*180 ± 7*	*175 ± 4*	-

Table 4.2-3*: Rising times of ^{34,35}Ar and ^{18,19}Ne for different positions of the valves (O: Open Valve, C: Closed Valve) and ion source modes.*
The rising times have been determined from experimental data points using a FORTRAN program developed at CERN which uses fitting routines from the CERNLIB [Cer-00] and integrates the release function [Ber-03]. The parameter minimization and error analysis were performed with MINUIT [Jam-00] based on the Poison maximum likelihood χ^2.

THEORETICAL APPROACH

RIBO Code was used to simulate the paths and investigate the effusion times of particles generated from the double container to the ion source according to different status of the valves (figure 4.2-5).

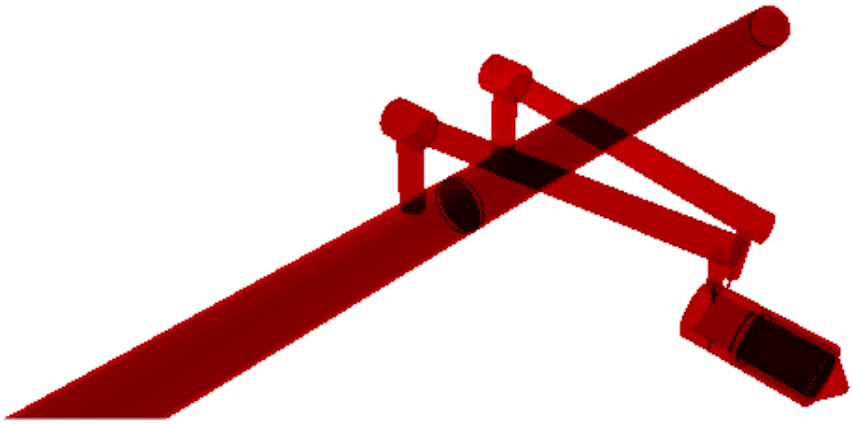

Figure 4.2-5*: Geometrical view of the Bi-Valve for RIBO simulations.*

As discussed in Chapter 2, the probability that an isotope effuses through a thin target is given by the equation (2.4.19) which uses one single exponential function [Kir-92]. In the case of a thick target having a transfer line system, one should take into account that the profile of the effusion times might be slightly different and then involves the use of two exponential functions to fit the data (figure 4.2-6). The probability an isotope effuses becomes then:

$$p_v(t) = (1 - \exp(\frac{-t}{t_1})) \cdot \exp(\frac{-t}{t_2}) \qquad (4.2.1)$$

where t_1 and t_2 are the parameter of the effusion times.

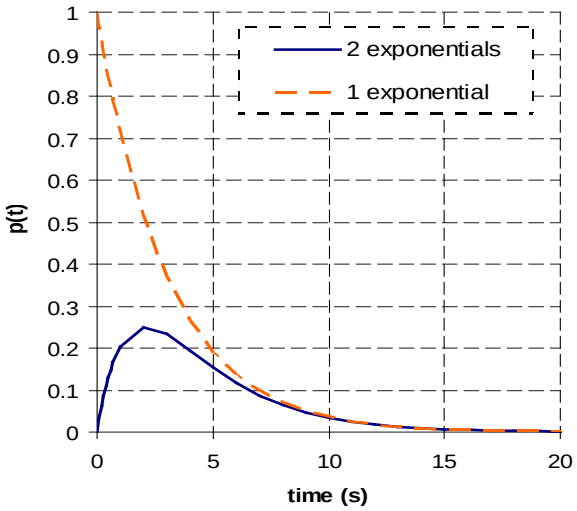

Figure 4.2-6: *differences between using either one or two exponential functions for p(t). The use of two exponential functions suits the shapes of the release curves measured.*

Figure 4.2.7 presents the results of the simulations for an isotope of mass 35, according to the possible states of the valves: OO and OC (or CO). Differences in the effusion times are shown for each position of the valves.

When fitting the events from the simulations with equation (4.2.1), t_1 is found to be equal to *0.010 s* whereas the differences mainly come from the second time variable, t_2 = *0.095 s* when the position of the valves are OO and t_2 = *0.060 s* when the valves are in the OC (or CO) statue. The isotope seemed to effuse slightly quicker through the system when one of the valves was closed. The rising time of ^{35}Ar *($t_{1/2}$= 1.780 s)* accounting for effusion process (table 4.2-3) confirmed this phenomenon.
Figure 4.2.8 represents the RIBO simulation of the fraction of isotopes of mass 35 visiting the other transfer line instead of leading directly to the ion source. Simulations showed that *2.5%* of the isotopes produced by the proton beam onto the CaO target material were actually revisiting the other line.

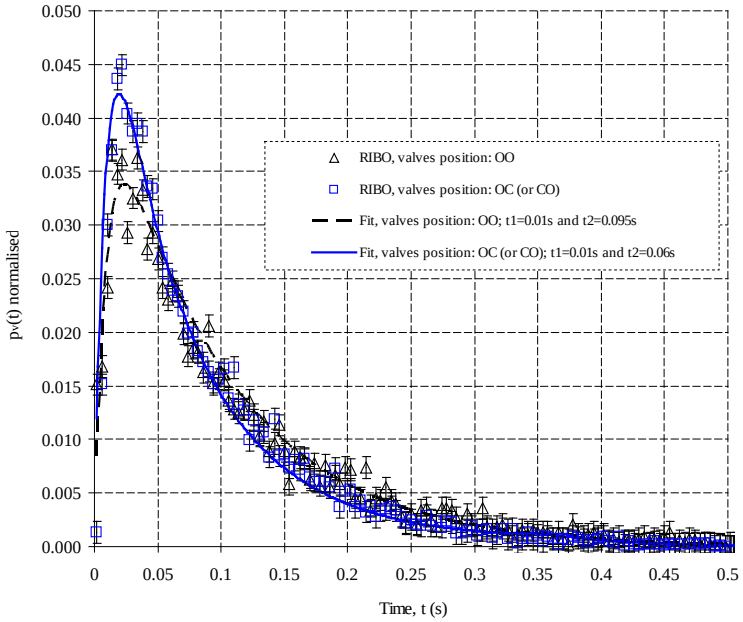

Figure 4.2-7*: Normalised $p_v(t)$ simulated with RIBO for isotopes of mass 35 according to the two different positions of the valves.*

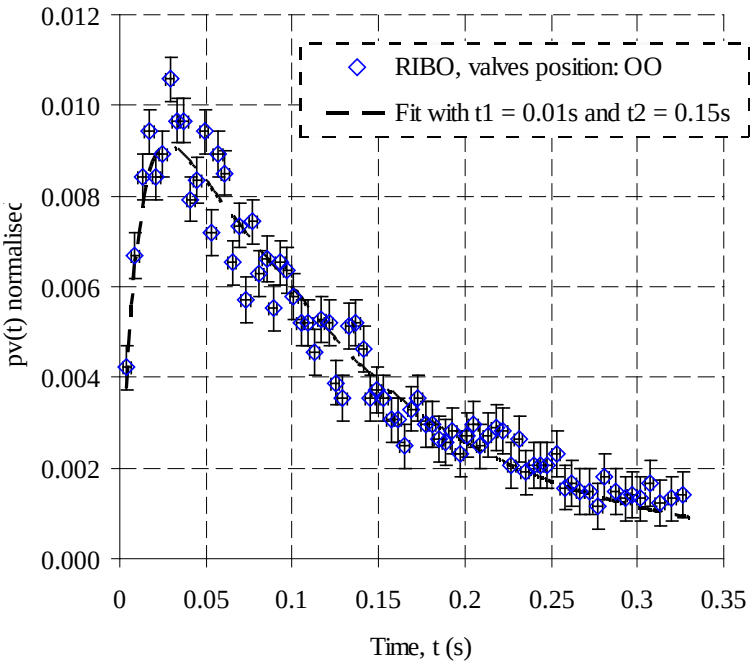

Figure 4.2-8*: Normalised $p_v(t)$, representing the fraction of isotopes (mass 35) visiting the other transfer line before being ionised, simulated with RIBO when both the valves are open (position OO).*

Fitting the events from the simulations (figure 4.2.7) with equation (4.2.1), gave value for t_1 and t_2 of *0.010 s* and *0.150 s* respectively. As seen earlier, t_1 got the same value; therefore a comparison was made possible according to the different t_2 used to fit. This latter concerning the isotopes revisiting the transfer line confirms the higher delay for those to reach the ion source. Convoluting equation (4.2.1) with equation (2.3.7) from the diffusion process gives an expression of the probability, *p(t)* that an isotope diffuses and effuses through the actual system according to the delay time:

$$p(t) = p_\mu \otimes p_\nu(t) = \int_0^t p_\mu(\tau)\cdot p_\nu(t-\tau)\cdot d\tau$$

$$= \frac{8\mu_0}{\pi^2}\sum_{n=0}^{\infty}\left[\frac{\exp(-\mu_n t)}{\nu_2-\mu_n} - \frac{\exp(-\nu_2 t)}{\nu_2-\mu_n} - \frac{\exp(-\mu_n t)}{\nu_1+\nu_2-\mu_n} + \frac{\exp(-\nu_2 t-\nu_1 t)}{\nu_1+\nu_2-\mu_n}\right] \qquad (4.2.2)$$

where $\mu_n = \mu_0(2n+1)^2$, $\mu_0 = \frac{\pi^2 D}{d^2}$, $\nu_1 = \frac{1}{t_1}$ and $\nu_2 = \frac{1}{t_2}$. Thus,

$$p(t) = \frac{8\mu_0}{\pi^2}\sum_{n=0}^{\infty}\left[\frac{\exp(-\mu_n t)-\exp(-\nu_2 t)}{\nu_2-\mu_n} - \frac{\exp(-\mu_n t)-\exp(-\nu_2 t-\nu_1 t)}{\nu_1+\nu_2-\mu_n}\right] \qquad (4.2.3)$$

COMPARISON WITH THE ONLINE MEASUREMENTS

The experimental data obtained for ^{35}Ar were fitted using the values of t_1 and t_2 from the previous RIBO simulations (effusion process) making the assumption that the delay parameter for diffusion, μ_0 is chosen arbitrarily and is kept as a fixed parameter all along the experiment. This means the influences of the temperature onto it was neglected (and is constant) so that $D(p,t) = D_0(p,t)\cdot e^{\frac{-E_a(p,t)}{k_b\cdot T(p,t)}}$ (see Section 2.3) was set as constant. Figure 4.2-9 shows the fitting of both experimental release curves when the valves were on position OO and OC respectively.

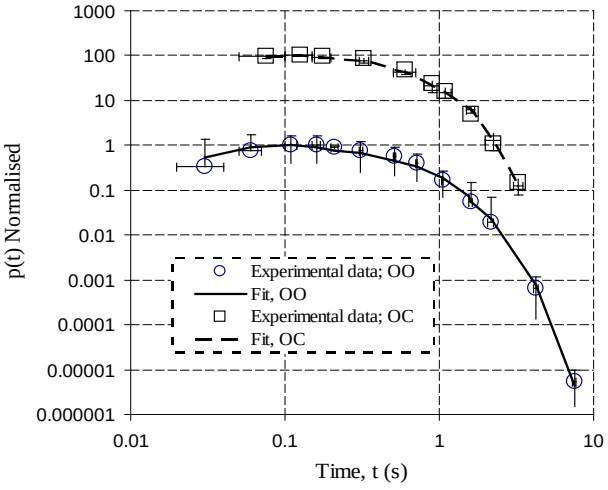

Figure 4.2-9*: Experimental data and theoretical fit (equation 4.2.3) of normalised p(t) versus the delay time for isotopes of mass 35. When only one valve is open (OC state): t_1 = 0.010 s, t_2 = 0.060 s and μ_0 = 1.79 s^{-1}. When all valves are open (OO state): t_1 = 0.010 s, t_2 = 0.095 s and μ_0 = 1.79 s^{-1}.*

In both cases above, a same value for the diffusion time constant made possible the fitting of the experimental data: $\mu_0 = 1.79\ s^{-1}$. Taking into account that the diffusion coefficient, *D*, is of order of magnitude of $5x10^{-13}$ *m* at a temperature of *2000 K* [Kir-92] for the CaO, from equation (2.3.8) one can estimate the distance, *d*, between two nuclei from which isotopes diffused out. In that specific case, d was found to be equal to:

$$d = \sqrt{\pi^2 \cdot \frac{D}{\mu_0}} = \sqrt{\pi^2 \cdot \frac{5 \cdot 10^{-13}}{1.79}} = 1.65 \cdot 10^{-6} \pm 0.50 \cdot 10^{-6}\,\mathrm{m} \quad (4.2.4)$$

Under vacuum conditions and at *923 K*, the decomposition of $CaCO_3$ particles of *10 μm* diameter leads to the formation of CaO having a specific surface area of *100 m^2/g* and particle size smaller than *10 μm*. Under ambient atmosphere, high surface area powders are not produced [Rah-03]. Therefore, the number used for the delay parameter for diffusion, μ_0, is actually very close to a parameter defining the real structure of the CaO medium used for the experiment. To compare the values of effusion simulated with RIBO to a standard target unit, equation (4.2.3) was used to fit ^{35}Ar isotopes released from a CaO target having a single transfer line (CaO#236) [Iso-08]. The diffusion parameter was kept the same as previously, $\mu_0 = 1.79\ s^{-1}$, and values of t_1 and t_2 were found to be equal to *0.010 s* and *0.09 s* respectively to manage the fitting of the released isotopes (figure 4.2-10).

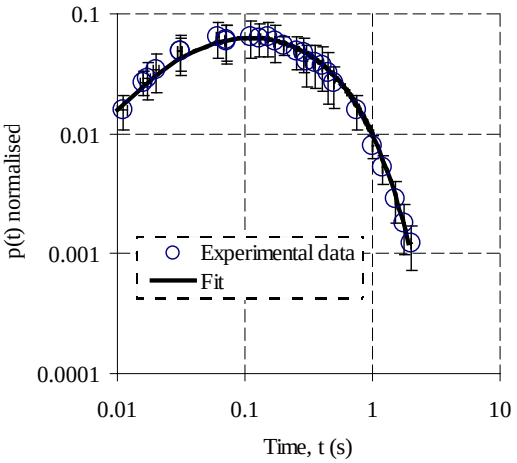

Figure 4.2-10*: Experimental data and theoretical fit (equation 4.2.3) of normalised p(t) versus the delay time for mass 35 for an ISOLDE standard target unit (CaO#236).* $t_1 = 0.01$ *s,* $t_2 = 0.09$ *s and* $\mu_0 = 1.79\ s^{-1}$.

Table 4.2-4 summarizes the different effusion times obtained with the RIBO code for a double target-transfer line having a similar geometry of the Bi-Valve and for a standard target-line unit.

CaO target type	*Valves positions*	t_1 *(s)*	t_2 *(s)*	μ_0 (s^{-1})
Bi-Valve	*OO*	*0.010*	*0.095*	*1.79*
Bi-Valve	*CO (or OC)*	*0.010*	*0.060*	*1.79*
Standard (CaO#236)	-	*0.010*	*0.090*	*1.79*

Table 4.2-4*: Effusion times* t_1 *and* t_2 *simulated with RIBO for* ^{35}*Ar* ($t_{1/2} = 1.775$ *s) through the Bi-Valve and comparison to a standard CaO target unit. The diffusion delay time,* μ_0*, has been taken as an arbitrary number to fit the simulations.*

Such differences in the time structures for the effusion are explained by the fact that the geometry of the Bi-Valve is different from the standard target unit (chimney positions, chicanes, transfer line slightly longer and holes leading to the ion source factor 5 smaller).

EFFICIENCY INVESTIGATIONS

To really understand the impact of the Bi-Valve in the release of the isotopes produced from the CaO material, one has to investigate the release efficiencies of the system studied. As discussed in Chapter 2, the release efficiency of a target-transfer line system is given by the expression:

$$Eff_r(\lambda) = \int_{t=0}^{\infty} p(t) \cdot e^{-\lambda \cdot t} \cdot dt \qquad (4.2.5)$$

Therefore, using equation 4.2.3:

$$Eff_r(\lambda) = \frac{8\mu_0}{\pi^2} \sum_{n=0}^{\infty} \left[\frac{\exp(-\mu_n t - \lambda t)}{-\mu_n - \lambda} - \frac{\exp(-\nu_2 t - \lambda t)}{\nu_2 - \mu_n} - \frac{\exp(-\mu_n t - \lambda t)}{-\mu_n - \lambda} + \frac{\exp(-\nu_2 t - \nu_1 t - \lambda t)}{-\nu_2 - \nu_1 - \lambda} \right]_{t=0}^{t=\infty} \qquad (4.2.6)$$

$$Eff_r(\lambda) = \frac{8\mu_0}{\pi^2} \cdot \frac{\nu_1}{\alpha} \sum_{n=0}^{\infty} \left[\frac{1}{\lambda + \mu_n} \right] \qquad (4.2.7)$$

where $\alpha = \frac{\nu_1}{\nu_2 \cdot (\nu_2 + \nu_1)}$ is the normalisation parameter. Thus,

$$Eff_r(\lambda) = \frac{8\mu_0}{\pi^2} \cdot \frac{(-\nu_2 - \lambda) \cdot (-\nu_2 - \nu_1 - \lambda)}{\nu_2 \cdot (\nu_2 + \nu_1)} \sum_{n=0}^{\infty} \left[\frac{1}{\lambda + \mu_n} \right] \qquad (4.2.8)$$

$$Eff_r(t_{1/2}) = \frac{8\mu_0}{\pi^2} \cdot \frac{(\nu_2 + \frac{\ln 2}{t_{1/2}}) \cdot (\nu_2 + \nu_1 + \frac{\ln 2}{t_{1/2}})}{\nu_2 \cdot (\nu_2 + \nu_1)} \sum_{n=0}^{\infty} \left[\frac{1}{\frac{\ln 2}{t_{1/2}} + \mu_n} \right] \qquad (4.2.9)$$

with $Eff_r(t_{1/2} \to \infty) = 1$.

It is clear from figure 4.2-11 that having one of the valves closed increases the efficiency of the release of the isotopes produced in the target. On the other hand, when both of the valves are open, the efficiency is similar to the one from the standard unit.

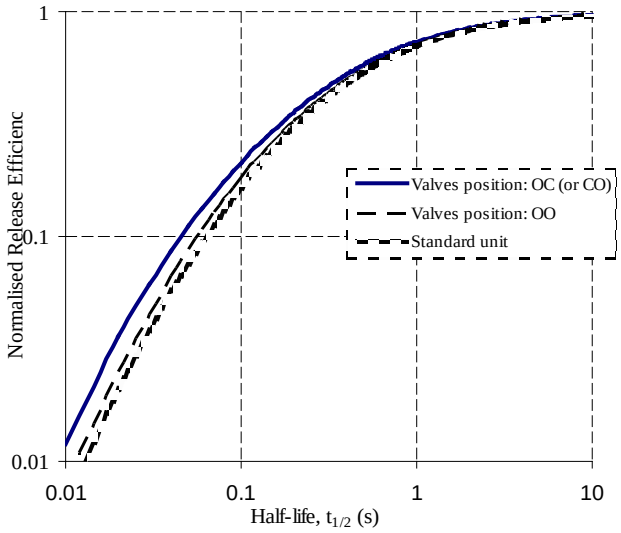

Figure 4.2-11*: Theoretical normalised efficiencies, $Eff_r(t_{1/2})$, for the release of Ar from the Bi-Valve (two different positions) and from an ISOLDE standard unit.*

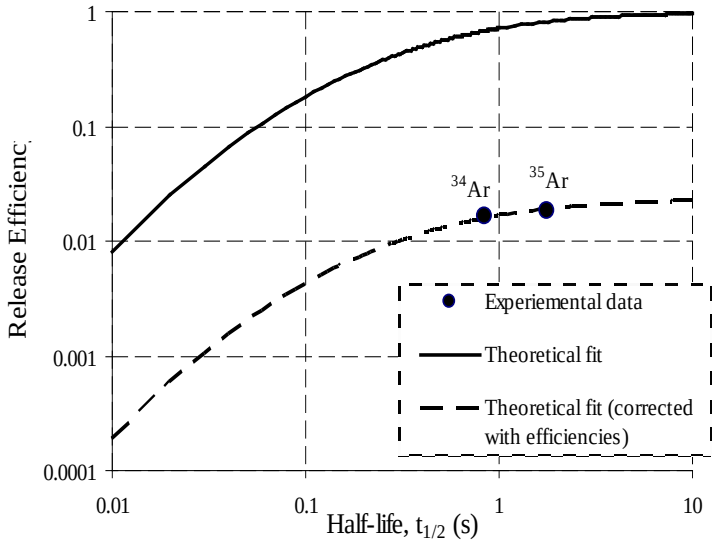

Figure 4.2-12*: Experimental and theoretical release efficiencies for Ar isotopes from the Bi-Valve.*

Comparisons of all the different efficiencies involved into the system were made between the experimental data and the theoretical point of view discussed earlier (figure 4.2-12). The release efficiency, ε_r, for $^{34, 35}$Ar was measured to be *1.67*% and *1.83%* respectively (table 4.2-5).

			Experiment				*Theory*
Isotope	*Half-life, $t_{1/2}$ (s)*	*In target Production from FLUKA (ion/μC)*	*Yield (ion/μC)*	*ε_{ion} (%)*	*$\varepsilon_{transport}$ (%)*	*$\varepsilon_{release}$ (%)*	*$\varepsilon_{release}$ (%) (eq. 4.2.9)*
^{34}Ar	*0.844*	*$6x10^7$*	*$2.36x10^4$*	*2.5*	*94*	*1.67*	*1.60*
^{35}Ar	*1.775*	*$6x10^8$*	*$2.58x10^5$*	*2.5*	*94*	*1.83*	*1.92*

Table 4.2-5*: Experimental yields and efficiencies obtained online for $^{34, 35}$Ar with the Bi-Valve (T = 1920ºC; Valves position: CO) compared to the theory. FLUKA was preferred to SigmasWIN2000 (Silberberg and Tsao), this latter known to over-estimate values.*

The release efficiencies calculated with the equation (4.2.9) showed to be very close, within 95%, to the experimental measurements ^{34,35}Ar.

In the EURISOL Design Study the total incoming beam power on direct targets is 100 kW. The layout of the targets depends on the nature of the materials to be irradiated [Eur-09]: one target unit at 100 μA will be used for metal foils (i.e Ta) and liquid metal (i.e Pb), 2 sub-units at 50 μA for SiC and then 4 sub-units at 25 μA for oxides (i.e Al_2O_3). The Bi-valve experiment benchmarked the tools (RIBO) to design proper target units with 4 sub-units (EURISOL). Although RIBO is a tool to describe the effusion process of isotopes within a specific configuration, it does not describe the probability for an isotope to be ionized while being in the ionization chamber [Liv-09].

Conclusions and Outlook

Two key issues of developments mandatory for the forthcoming generation of ISOL target-ion source units were treated in this thesis by the conception and the online measurements of two prototypes at ISOLDE-CERN. The first domain dealt with the purity of the ion beams that are delivered by the target-ion source. Ion beams at ISOLDE suffer from isobaric contaminants such as alkalis; therefore, a transfer line was designed with the aim of trapping such elements before they reach the ion source. The second field of study investigated in this thesis lead to the demonstration of how a target-ion source unit can handle an incoming beam of hundreds of kW such as the EURISOL facility plans to use. To operate with such beam parameters it is necessary to design a multibody target and dedicated transfer line able to dissipate all the incoming power and at the same time be reliable in the release of isotopes to the different users.

In the context of beam purification, the combination of the RILIS with a quartz transfer line showed the trapping effect on the contaminants. It did not only allow an excellent Zn versus Rb (and Ga) separation, but works also well for the heavier isobars Cd versus Cs (and In). The RIBO code allowed dimensioning the piece of quartz to be used with respect to the number of collisions of a radioactive element. A tube of quartz of *50 mm* long and *6 mm* diameter was chosen as being the optimum dimension. Two quartz units were designed operating from*700ºC* to *1100ºC*; and from *300ºC* to *800ºC*. Energy flow of the heat transfer along the system was investigated and thus allowed the design of the prototypes.
Suppression factors were calculated for $^{80,\ 82m}$Rb, $^{126,\ 142}$Cs, ^{8}Li, ^{46}K, ^{25}Na, ^{114}In, ^{77}Ga, $^{95,\ 96}$Sr, and yields were compared to those obtained with an ISOLDE standard transfer line.
^{80}Rb and ^{142}Cs were suppressed by 4 and 3 orders of magnitude respectively. A clear suppression behaviour of the ^{80}Rb and ^{126}Cs as a function of the quartz temperature was showed.
The enthalpy of adsorption was estimated for Rb and Cs from a fit to the experimental data: ΔH_{ad} (Rb) = *-242 ± 20* kJ/mol and ΔH_{ad} (Cs) = *-145 ± 20* kJ/mol. These enthalpies showed to be about *80%* and *85%* respectively of values obtained by isothermal chromatography.
Recently, ISOLTRAP physics have successfully used a target-ion source unit equipped with a quartz transfer line and achieved the measurement of ^{207}Tl by retaining the francium (francium was not visible); the Fr-to-Tl yield ratio was around 100 without quartz. Sapphire has been investigated as trapping material at ORNL and integrated to this concept to obtain new chemical purification factors [Jos-09].

The Bi-Valve, a double-transfer line merging into a single FEBIAD ion source with remotely controlled valves was designed and tested at ISOLDE. They also showed equal isotope production and heat deposition in both target containers. This was verified online with symmetric release profiles and isotope yields obtained for ^{34,35}Ar and ^{19}Ne, at two ion source operation temperatures, to better than *10-20%*. Engineering design of the prototype has been performed and ANSYS simulations allowed to estimate the heat flow along the prototype and helped in finding the right materials to develop an efficient, gas-tight and reliable valve system. The valve position was controlled by a program through the Ethernet network. The leak rate of the closed valves measured on $^{34,\ 35}$Ar was equal to *0.3%*. The FEBIAD ion source was operated at two temperatures: *1920°C* and *2100°C*, which increased the yields of up to a factor 4. Four isotopes were more particularly investigated online: ^{34,35}Ar and ^{18,19}Ne. The efficiency of the double line merging was found to be in the range of *75* to *95%*, depending on the investigated isotope and ion source operation mode. This originates from the revisit of the isotopes in the second open transfer line, as observed in the increased effusion times and in the decrease of the ion source efficiency when both transfer lines were open. The best efficiencies for the two merging lines configuration were found for the highest temperature ion source operation mode. The overall measured yields agreed well with figures obtained with standard CaO ISOLDE target units.

The RIBO code helped in fitting the experimental data by providing the profile of the effusion distribution of the isotopes within the Bi-Valve unit for the different situations. A clear dependence of the valve position on the effusion process was confirmed. A mathematical expression for the probability, *p(t)* that an isotope diffuses and effuses through the system is proposed. The simulated release efficiencies were in agreement to the experimental ones for $^{34, 35}$Ar at *95%* thus opening the way to the engineering of multi body target units for future facilities.

The Bi-Valve experiment benchmarked the tools calculating the effusion of isotopes through a complex configuration of target where 2 sub-units (2 transfer lines) merge into one single ion source. The design of 4 sub-units (oxides) or 2 sub-units (SiC) such as in the EURISOL concept will require these tools (i.e. RIBO) to engineer the unit and describe the effusion process. The ionization process must be implemented in the code [Liv-09]. Recently high power Al_2O_3 target prototypes have been tested at TRIUMF by EURISOL DS Task #3 at 25 μA [Sto-09] under the s1149 approved experiment, the composition of materials to be used under high power beams have been engineered.

Bibliography

[All-90] B.W. Allardyce, R. Billinge, C.E. Hill, C. Metzger, K. Schindl, H. Schoenauer and D.J. Simon, in: Proc. of the 2nd European Particle Accelerator Conf. EPAC-90, Nice (June 1990), eds. P. Marin and P. Mandrillon (Edition Frontieres, 1990) p. 583.

[Ans-00] ANSYS Workbench website, http://www.ansys.com/products/workbench.asp

[Bec-96] H. Becquerel, Comptes Rendus 122, 420 ff. (1896).

[Ben-98] J. Benlliure, A. Grewe, M. de Jong, K.H. Schmidt, S. Zhdanov, Nucl. Phys. A 628, 458 (1998)

[Ber-03] U.C. Bergmann et al. 'Production yields of noble-gas isotopes from ISOLDE UCx/graphite targets', Nucl. Instr. And Meth. B 204 (2003) 220-224

[Bey-00] G.J. Beyer, Hyperfine Interactions 129 (2000) 529–553

[Bil-03] J. C. Bilheux, G. D. Alton, Y. Liu, J. M. Cole, and C. L. Williams, AIP Conf. Proc. 680, 241 2003.

[Bio-86] T. Biørnstad, E. Hagebo, P. Hoff, O.C. Jonsson, E. Kugler, H.L. Ravn, S. Sundell and B. Vosicki, 'Methods for Production of Intense Beams of Unstable Nuclei: New Developments at ISOLDE', Phys. Scripta 34 (1986) 578

[Boe-69] J. H. de Boer, The dynamical character of adsorption, Clarendon Press Oxford (1969).

[Bol-96] NIM A, Volume 368, Issue 3, 11 January 1996, p675-697. doi:10.1016/0168-9002(95)00561-7

[Bri-03] P. Bricault,' high Power targets for ISOL Radioactive Ion Beam Facility', Proceedings of the 2003 Particle Aceelerator conference.

[Bri-03b] P. Bricault, M. Dombsky, NIM B204 (2003) 319.

[Car-78] Carraz, L. C., Haldorsen, I., Ravn, H. L., Skarestad, M., and Westgaard, L., Nucl. Instr. Meth. 148, 217 (1978)

[Car-08] H. K. Carter et al., Radioactive target and ion source test facilities at HRIBF, NIMB 266(2008) 4702-4705

[Cer-00] CERN Program Library,' http://cernlib.web.cern.ch/cernlib/'

[Cra-75] J. Crank,' The Mathematics of Diffusion', 2nd Edition, Clarendon Press, Oxford, 1975

[Cur-98] P. Curie and M. Curie: Comptes Rendus Acad. Sciences127 (1898) 175.

[Eur-00] Feasibility report, EURISOL website, http://www.eurisol.org

[Eur-01] www.nupecc.org/presentations/eurisol_ds_nov11.ppt

[Eur-09] T. Stora et al,' Final Report – 100 kW direct target stations – Task #3', EDMS document nº975615, 20/07/09.

[Ess-02] S. Essabaa, ' The study of a new PARRNe experimental area using an electron linac close to the Orsay tandem', Proceddings of EPAC 2002, Paris, France

[Fai-00] FAIR – Facility for antiproton and Ion Research – www.gsi.de/fair

[Fas-03] A. Fasso, A. Ferrari, S. Roesler, P.R. Sala, G. Battistoni, F. Cerutti, E. Gadioli, M.V. Garzelli, F. Ballarini, A. Ottolenghi, A. Empl and J. Ranft, "The physics models of FLUKA: status and recent developments", Computing in High Energy and Nuclear Physics 2003 Conference (CHEP2003), La Jolla, CA, USA, March 24-28, 2003, (paper MOMT005), eConf C0303241 (2003), arXiv:hep-ph/0306267

[Fas-05] A. Fasso, A. Ferrari, J. Ranft, and P.R. Sala, "FLUKA: a multi-particle transport code", CERN-2005-10 (2005), INFN/TC_05/11, SLAC-R-773

[Fed-00] V. N. Fedosseev, G. Huber, U. Koester, J. Lettry, 'The ISOLDE laser ion source for exotic nuclei', Hyperfine Interactions 127 (2000) 409-416

[Fed-06] V. N. Fedosseev, B. A. Marsh, D. V. Fedorov, U. Koster, 'Ionization Scheme Development at the ISOLDE RILIS', Hyperfine Interactions (2005), Springer 2006. DOI 10.1007/s10751-005-9204-2

[Fed-06b] V.N.Fedosseev et al,"Development of the RILIS Research laboratory at ISOLDE", CERN-INTX-2006-015, INTC-I-065, 20.01.2006

[Flu-00] A. Fasso, A. Ferrari, <Fluka Code>, Website www.fluka.org

[Gar-06] R. Garoby, Nuclear Physics B (Proc. Suppl.) 155 (2006) 67–73

[Gli-00] M. E. Glicksman, 'Diffusion in Solids; Field theory, Solid-State Principles and Applications', J. Wiley & Sons, Inc; 2000.

[Gue-02] D. Guerreau,' Radioactive beam facilities: european perspectives', Eur. Phys. J. A 13, 263-266 (2002).

[Gut-49] A. Guthrie and R. K. Wakerling, eds., Vacuum Equipment and Techniques, McGraw Hill, London, 1949.

[Gre-05] J. Greene, NIM B241 (2005) 986-990

[Hal-57] D. Halliday, 'Introduction à la Physique Nucléaire', Dunod Paris, 1957

[Hey-99] K. Heyde, 'Basic Ideas and Concepts in Nuclear Physics, Second Edition', IOP Publishing Ltd 1999

[Hie-00] http://hie-isolde.web.cern.ch/HIE-ISOLDE/

[Hof-84] Hoff, P. Jonsson, O. C., Kugler, E., and Ravn, H. L,. Nucl. Instr. Meth. 221, 313 (1984)

[Inc-02] Frank P Incropera, David P DeWitt , 'Fundamentals of Heat and Mass Transfer Fifth Edition', John Wiley & Sons 2002.

[Iso-00] ISOLDE website, www.cern.ch/ISOLDE; visited in October 2008.

[Jam-00] F. James, M. Roos, MINUIT, Function Minimization and Error Analysis, CERN D506, Long Writeup.

[Jol-34] I. Curie and F. Joliot, J. phys. radium 5, 153 (1934).

[Jos-09] C. Jost, H.K. Carter,' Radioactive Ion Beam Purification By Sepective Adsorption', www.eurisol.org/site02

[Kir-75] R. Kirchner et al., Nucl. Instr. Meth. B 126 (1997) 135.

[Kir-76] R. Kirchner and E. Roeckl, 'Investigation of gaseous discharge ion sources for isotope separation on-line', Nucl. Instr. Meth. 133 (1976) 187-204

[Kir-81a] R. Kirchner, 'Progress in ion source development for on-line separators', Nucl. Instr. Meth. 186 (1981) 275-293

[Kir-87] R. Kirkaldy and D. J. Young, Diffusion in the Condensed State, The Institute of Metals, London 1987.

[Kir-87b] R. Kirchner, An ion source with bunched beam release, Nuclear Instruments and Methods in Physics Research, B26 (1987) 204-212.

[Kir-90] R. Kirchner, Nucl. Instr. Meth. A 292 (1990) 203.

[Kir-92] R. Kirchner, On the release and ionization efficiency of catcher-ion-source systems in isotope isotope separation on-line, Nuclear Instruments and Methods in Physics Research, B70 (1992) 186-199.

[Kir-96] R. Kirchner, 'Ion sources for radioactive beams and related problems (Review)', Rev. Sci. Instr. 67 (1996) 928-933

[Kir-97] R. Kirchner Nucl. Instr. Meth. B 126 (1997), p. 135.

[Kof-51] Kofoed-Hansen and Nielsen, Phys. Rev. 82, 96 (1951).

[Kos-01] U. Koster, ' ISOLDE target and ion source chemistry', Radiochim, Acta 89, 749-756 (2001)

[Kos-07] U. Koster et al.' Progress in ISOL target-ion-source systems', Nuclear Instruments and Methods in Physics Research Section B, v. 266, iss. 19-20, p. 4229-4239.
[Kow-07] M. Kowalska,' High-precision mass studies on short-lived nuclides using ISOLTRAP', CERN-INTC-2007-022 (2007).
[Kra-86] K.L. Kratz et al., "The Beta-decay half-life of 13048Cd82 and its importance for astrophysical r-process scenarios", CERN-EP/86-189, 18 November 1986.
[Lab-00] LabVIEW Website, http://www.ni.com/labview
[Lan-18] Langmuir, I. , J. Amer. Chem. Soc., 38, 2267 (1916) ; 40, 1361 (1918).
[Lan-25] I. Langmuir and K. H. Kingdon, Proc. R. Soc. London, A107, 61, 1925
[Lax-03] R.E. Laxal, NIM B 204 (2003) 400-409
[Lec-08] N. Lecesne, Rev. Sci. Instrum. 79, 02A907 (2008); doi:10.1063/1.2823895
[Let-97] J. Lettry, 'Pulse shape of the ISOLDE radioactive ion beams', Nucl. Instrum. And Methods Research B 126 (1997) 130-134
[Lil-01] J. Lilley, 'Nuclear Physics, Principles and Applications', Wiley, 2001
[Liv-09] L. Penescu. ISOL Ion Source Development for 100kW Beam Power. PhD thesis, University Politehnica of Bucharest, (to be published in 2009).
[Loe-34] L. B. Loeb,' The Kinetic Theory of Gases', McGraw-Hill Book Company, Inc, 1934.
[Loi-96] M. Loiselet et al., "Production and Acceleration of Radioactive Beams at Louvain-la-Neuve," 14th Int. Conf. on Cyclotrons and their Application, Cape Town, 1995 (World Scientific, 1996) p. 629.
[Luk-06] S. Lukic,' systematic comparison of ISOLDE-SC yields with calculated in-target production rates', NIM A, V 565, Issue 2, 15 Sept. 2006, p784-800
[Mis-92] V. I. Mishin, V. N. Fedosseev, H. L Ravn,' Chemically selective laser ion-source for the CERN-ISOLDE on-line mass separator facility', Nuclear Instruments and Methods in Physics Research B73 (1993) 550-560
[Moo-05] I. Moore et al., Development of a laser ion source at IGISOL, J. Phys. G: Nucl. Part. Phy. 31 (2005) S1499-S1502
[Mor-92] K. Morita et al., RIKEN isotope separator on-line GARIS/IGISOL, NIMB 70(1992) 220-225
[Nup-00] Nuclear Physics European Collaboration Committee website, http://www.nupecc.org/
[Nol-02] RIA, http://www.phy.anl.gov/ria/index.html, see J.A. Nolen, European Physical Journal A 13 (2002) 255
[Omn-00] Omnexus 4 adhesives website, http://www.omnexus4adhesives.com/documentsom4as/indexables/editorial/articles/769/Relative-radiation-resistan.jpg
[Pan-02] V.N. Panteleev, ' Developpment of high temperature targets at IRIS facility', Nuclear Physics A 701 (2002) 470c-475c
[Pre-58] R. D. Present, Kinetic Theory of Gases _McGraw-Hill, New York, 1958.
[Rah-03] M. N. Rahaman, 'Ceramic Processing And sintering', Second Edition. 2003.
[Rav-75] H. L. Ravn, S. Sundell, L. Westgaard, Nucl. Instr. and Meth. 123, Issue 1, 1 Jan 1975, 131-144
[Rav-79] H. Ravn, Phys. Rep. 54 (1979) 203.
[Rav-86] H. Ravn, B. Allardyce, 'On-Line Mass Separators', CERN-EP/87-105; CERN-PS-87-50-SC, 1988, p53.
[Rav-98] H. Ravn Phil. Trans. R. Soc. Lond. A 356 (1998), p. 1955.
[Rex-00] http://rextrap.home.cern.ch/rextrap/
[Rik-00] RIKEN Website, SLOWRI Team, http://www.riken.go.jp/engn/r-world/research/lab/nishina/slowri/index.html
[Rot-82] A. Roth, 'Vacuum technology', Second, Revised Edition, North Holland, 1982.
[Sak-88] G. L. Saksaganskii, 'Molecular Flow In Complex Vacuum Systems', 1988.

[San-05] M. Santana Leitner, A Monte Carlo Code to Optimize the Production of Radioactive Ion Beams by the ISOL Technique, PhD. Thesis, UPC-ETSEIB / CERN.

[Sch-96] P. Schmor et al., ISAC: the High Intensity Radioactive Beam Facility at TRIUMF, American Physical Society, APS/AAPT Joint Meeting, May 2-5, 1996.

[Sch-08] F. Schwellnus, NIMB, Volume 266, issues 19-20, October 2008, p4383-4386

[Sho-02] A. Shotter, 'Advances at ISOL facilities', NIMB V204, May 2003, p17-19.

[Sil-73] R. Silberberg, C. H. Tsao, 'Partial Cross-section in High-Energy Nuclear Reactions, and Astrophysical Applications', The Astrophysical Journal Supplement Series No 220(II), 25, 335-368

[Sim-07] E. Simmat. R. Andrae , F14 - Debye Temperature. Website www.rzuser.uni-heidelberg.de/~randrae/F14.pdf.

[Sti-92] T. H. Stix, Waves in Plasmas, Springer-Verlag, New York, Berlin, Heidelberg, (1992), ISBN 0883188597.

[Sto-09] T. Stora et al.,'Oxide target Designs for High Primary Beam Intensities for Future Radioactive Ion Beam Facilities', AIP Conf. Proceedings, 1099, 764 (2009).

[Sto-09b] T. Stora,'Online tests of a high power Al2O3 EURISOL target prototype', EURISOL Project Document ESL-TAU-R-002 REV 0.1, EDMS Document 1011259, 07/2009.

[Str-03] D.W. Stracener, Nucl. Instr. And Meth. B 204 (2003) 42.

[Sun-92] S. Sundell, H. Ravn and the ISOLDE Collaboration, NIM B70 (1992) 160.

[Spe-00] Official SPES website, www.lnl.infn.it/~spes/

[Tur-08] M. Turrión , M. Eller, 'Management of ISOLDE yields', Nuclear Instruments and Methods in Physics Research Section B: Beam Interactions with Materials and Atoms, Volume 266, Issues 19-20, October 2008, Pages 4674-4677

[Vil-01] C.C. Villari, Nuclear Physics A, Volume 693, Issues 1-2, 8 October 2001, Pages 465-476.

[Vos-81] B. Vosicki et al., Nucl. Instr. Meth. 186 (1981) 307.

[Wol-95] B. Wolf, Handbook of Ion Sources, CRC Press Inc. (1995)

[Yor-09] R. C. York,' FRIB: A New Accelerator Facility for The Production of Rare Isotope Beams', Proceedings of SRF2009, Berlin, Germany.

[Zha-99] H. Zhang, book 'Ion Sources', Springer (1999)